2.12 Appendix

2.12.1 References

(1) Metallic Materials and Elements for Aerospace Vehicle Structures, MIL-HDBK-5A, Change Notice 2, Sections 2.8 and 8.1, July 24, 1967.

(2) Wojtaszak, I. A., "Deformation of Thin Cylindrical Shells Subject to Internal Loading", Phil. Mag. 5.7, 18, (123), December, 1934, p 1099.

(3) Roark, R. J., Formulas for Stress and Strain, McGraw-Hill Book Co., 4th Ed., Equation 6, (1965), p 271.

(4) Nelms, H. A., "Structural Analysis of Shipping Casks, Vol 3, Effects of Jacket Physical Properties and Curvature on Puncture Resistance", Oak Ridge National Laboratory, ORNL-TM-1312, Vol 3, June, 1968.

(5) Lustman, B., and Kerze, F., The Metallurgy of Zirconium, p 626, McGraw-Hill Book Co., New York (1955).

(6) Tipton, C., Reactor Handbook, 2nd Ed., Vol I, Materials, p 727.

(7) Tipton, C., p 867.

(8) Roark, R. J., Equation 15, p 366.

(9) Brown, A. F. C., and Edmonds, R., "The Dynamic Yield Strength of Steel at an Intermediate Rate of Loading", Proceedings of the Institution of Mechanical Engineers, 159, 1948, p 11-23.

(10) Roark, R. J., Case 18, p 152.

(11) Private communication from Dr. Martin N. Haas, Associate Director, Nuclear Science and Technology Facility, State University of New York at Buffalo to Mr. R. Denney, Allied Chemical Company, 550 Second St., Idaho Falls, Idaho, 83401, File Ref. J-759.

(12) Roark, R. J., Case 41, p 227.

(13) Nuclear Regulatory Commission, Packaging of Radioactive Material for Transportation and Transportation of Radioactive Material Under Certain Conditions; Compatibility with IAEA Regulations, Proposed Rules 10CFR 71, August, 1979.

(14) Roark, R. J., Case 25, p 352.

(15) Roark, R. J., p 243.

(16) Roark, R. J., Case 6, p 217.

(17) Baumeister, T., Mark's Standard Handbook for Mechanical Engineers, 7th Ed., McGraw-Hill Book Co., New York, p 13-25 (1966).

(18) RDT F8-9T "Design Basis for Fuel and Irradiations Experiment Resistance to Shock and Vibration in Truck Transport; USERDA, Div. of Reactor Research and Development (February 1975.

(19) Roark, R. J., Case 33, p 112.

(20) ASME Boiler and Pressure Vessel Code (1974).

(21) Baker, Kovalevsky, and Rish, Structural Analysis of Shells, McGraw-Hill (1972).

(22) Kirk, J. A., and Overway, N., "One-Shot Shock Absorbers", Machine Design, p 152 (October 20, 1977).

(23) Roark, R. J., Case 4, p 320

(24) Roark, R. J., Case 18, p 176.

(25) Roark, R. J., Case 31, p 112.

(26) Roark, R. J., Case 30, p 307.

(27) Roark, R. J., Case 81, p 239.

(28) The Nastran User's Manual (Level 15.0), C. W. McCormick, Editor, NASA SP-222 (01), May 1973.

(29) Roark, R. J., Case 23, p 109.

(30) Roark, R. J., Case 36, p 225.

(31) Shigley, J. E., Mechanical Engineering Design, McGraw-Hill Publishing Co., 1977, p 113-119.

THIS PAGE INTENTIONALLY LEFT BLANK

THIS PAGE INTENTIONALLY LEFT BLANK

2.12.2 Results of Cover Lifting Tests

Approved by: W. J. Madia

Battelle
Columbus Laboratories

Project Number 117-5865

Internal Distribution

W. J. Madia
T. R. Emswiler
D. E. Stellbrecht
W. J. Gallagher
A. Parsons
D. E. Lozier

Date April 18, 1980

To R. J. Burian

From D. E. Lozier

Subject Testing of Lifting Handle on Cask BMI-1 Lid, February 27, 1980

The lid-lifting handle welded on the lid of cask BMI-1 was tested by attaching cask BCL-3, with its lid in place, to the BMI-1 lid with a chain. The assembly was then lifted off the floor and suspended for 3 minutes by a crane hooked to the BMI-1 lid-lifting handle. The certified weight of cask BCL-3 with lid is 2595 lb., placing a total weight on the lifting handle of >3695 lb. which is in excess of three times the weight of the 1100 lb. lid.

The weld was then checked by liquid dye penetrant in accordance with BCL QA Procedure HL-PP-60 with no defects detected.

DEL/cm

QUALITY ASSURANCE DOCUMENT

LIQUID PENETRANT INSPECTION WORK COMPLETION RECORD

BATTELLE
Columbus Laboratories
505 King Avenue
Columbus, Ohio 43201

Prepared by

D. E. Lozier

April 2, 1980
Date

APPROVED BY

Date

APPROVED BY

4/4/80
Date

EV. A,
-28-80

APPROVED BY

APPROVED BY

4/4/80

LIQUID PENETRANT INSPECTION
WORK COMPLETION RECORD

1. Scope

This record documents the implementation and results of a liquid penetrant inspection.

2. Reference

2.1 BCL Hot Lab QA Manual (Sections HL-X-1 and HL-I-1).

2.2 HL-PP-60 Liquid Penetrant Inspection.

3. Work Completion Records

3.1 Work completion records shall be documented by the certified inspector performing the inspection and reviewed by a Q. A. respresentative.

3.2 Document the inspection on Record Form WC-60.

RECORD FORM WC-60
LIQUID PENETRANT INSPECTION

1. Item inspected [illegible] BM1-1 [illegible]

2. Inspection method (check method used).

   2.1 Visual Dye, i.e. spotcheck ✓

   2.2 Fluorescent Penetrant _____

	Initial	Date
3. Inspection performed as per HL-PP-60.	DES	2-27-80
4. Item approved as per acceptance criteria in HL-PP-60.	DES	2-27-80

5. Defects observed: None

6. Corrective action taken on defects:

   6.1 Reinspect after corrective action and document on another Record Form WC-60.

7. Inspection conducted by: [illegible] Date 2-27-80

8. Reviewed by: [illegible] Date 2-27-80

REV. A, 3-28-80

2.12.3 Description of MONSA Computer Program

MONSA (multilayer Orthotropic Nonsymmetric Shell Analysis) is a digital computer program written in FORTRAN IV. It is based on the multisegment numerical integration method for the analysis of boundary value problems.

MONSAS determines the displacements, forces, and stresses for a composite shell of revolution. A composite shell is defined as a shell composed of a number of distinct parts which may have the following shapes: cylindrical, spheroidal, ellipsoidal, paraboloidal, conical and toroidal. The shell wall may be composed of four different layers of orthotropic materials. The shell layers are specified by giving their location with respect to a reference surface.

Mechanical and temperature loadings can be applied to the shell. For nonsymmetric loadings, the user must determine the Fourier harmonics of the loadings and perform the appropriate number of shell calculations. Temperatures can vary along the shell meridian as well as through the thickness of the wall. The latter can be accomplished by specifying the temperature on the inner and outer surfaces and on three internal surfaces of the shell wall. A shell spinning about its longitudinal axis can be analyzed. A shell subjected to harmonically varying mechanical or temperature loadings can also be analyzed.

MONSAV will determine the natural frequencies and mode shapes of composite shells of revolution described above. The procedure is based on an iterative technique in which a trial frequency is picked and a determinant is calculated. The trial frequency becomes a natural frequency when the determinant vanishes.

Analysis of Shells of Revolution Subjected to Symmetrical and Nonsymmetrical Loads[1]

A. KALNINS
Assistant Professor
of Engineering and Applied Science,
Yale University,
New Haven, Conn.
Mem. ASME

The boundary-value problem of deformation of a rotationally symmetric shell is stated in terms of a new system of first-order ordinary differential equations which can be derived for any consistent linear bending theory of shells. The dependent variables contained in this system of equations are those quantities which appear in the natural boundary conditions on a rotationally symmetric edge of a shell of revolution. A numerical method of solution which combines the advantages of both the direct integration and the finite-difference approach is developed for the analysis of rotationally symmetric shells. This method eliminates the loss of accuracy encountered in the usual application of the direct integration approach to the analysis of shells. For the purpose of illustration, stresses and displacements of a pressurized torus are calculated and detailed numerical results are presented.

The shell of revolution is an important structural element, and the literature devoted to its analysis is extensive. With regard to axisymmetric deformation, various methods have been employed to obtain solutions of the bending theory of shells of revolution by means of the H. Reissner-Meissner equations. For example, Naghdi and DeSilva [1][2] use asymptotic integration; Lohmann [2], Münz [3], Klingbeil [4], employ a direct numerical integration approach; Galletly, et al. [5] find the solution for an ellipsoidal shell of revolution by both the finite-difference and the Runge-Kutta method; and Penny [6], Radkowski, et al. [7], and Sepetoski, et al. [8] utilize the finite-difference technique. A number of additional references which deal with the solution of the H. Reissner-Meissner equations can be found in the papers cited.

For problems of bending in the absence of axial symmetry, a reduction of the governing equations of arbitrary shells of revolution to a system of four second-order differential equations involving four unknowns has been carried out by Budiansky and Radkowski [9]. A method for obtaining the solution of the equations is given in [9] which is an extension of that employed in [7] and [8]. Furthermore, treatments of nonsymmetric deformation of shells of revolution are found in papers by Goldberg and Bogdanoff [10], where a system of first-order differential equations for conical shells is derived, and by Steele [11] and Schile [12], where solutions of certain types are considered by means of asymptotic integration.

Among the papers which employ numerical analysis, two dif-

[1] National Science Foundation Grant No. 23922, Report No. 3, July, 1963.

[2] Numbers in brackets designate References at end of paper.

Presented at the Summer Conference of the Applied Mechanics Division, Boulder, Colo., June 9–11, 1964, of The American Society of Mechanical Engineers.

Discussion of this paper should be addressed to the Editorial Department, ASME, United Engineering Center, 345 East 47th Street, New York, N. Y. 10017, and will be accepted until October 10, 1964. Discussion received after the closing date will be returned. Manuscript received by ASME Applied Mechanics Division, July 31, 1963. Paper No. 64—APM-33.

Nomenclature

ϕ, θ, ζ = coordinates of a point of shell
s = distance measured from an arbitrary origin along meridian in positive direction of ϕ
$\mathbf{t}_\phi, \mathbf{t}_\theta, \mathbf{n}$ = unit vectors tangent to coordinate curves (see Fig. 1)
R_ϕ, R_θ = principal radii of curvature of middle surface
r = distance of a point on middle surface from axis of symmetry
E = Young's modulus
ν = Poisson's ratio
h = thickness of shell
α = coefficient of thermal expansion
D = $Eh^3/[12(1-\nu^2)]$
K = $Eh/(1-\nu^2)$
u_ϕ, u_θ, w = components of displacement of middle surface
β_ϕ, β_θ = angle of rotation of normal
p_ϕ, p_θ, p = components of mechanical surface loads
m_ϕ, m_θ = components of moment of surface loads
T, T_a, T_1 = temperature increment and temperature resultants
$N_\phi, N_\theta, N_{\theta\phi}$ = membrane stress resultants
$M_\phi, M_\theta, M_{\theta\phi}$ = moment resultants
Q_ϕ, Q_θ = transverse-shear resultants
N, Q = effective-shear resultants
J = $1/R_\phi + \sin\phi/r$
U = $1/R_\phi + \nu\sin\phi/r$
H = $1/R_\phi - \sin\phi/r$
n = integer, designating nth Fourier component
β = length factor
$(\ )_{,x}$ = derivative with respect to any coordinate
m = order of system of equations
M = number of segments
x = independent variable, either ϕ or s
x_i = end point of segment
$y(x)$ = $(m, 1)$ matrix, fundamental variables
$A(x)$ = (m, m) matrix, coefficients of differential equations
$B(x)$ = $(m, 1)$ matrix, nonhomogeneous coefficients
$Y(x)$ = (m, m) matrix, homogeneous solutions
$Z(x)$ = $(m, 1)$ matrix, nonhomogeneous solutions
C = $(m, 1)$ matrix, arbitrary constants
I = unit matrix

ferent methods of solution of the boundary-value problem of deformation of shells must be recognized; i.e., the direct integration [2–5] and the finite difference approach [5–9]. While the direct integration approach has certain important advantages, it also has a serious disadvantage; i.e., when the length of the shell is increased, a loss of accuracy invariably results. This phenomenon was clearly pointed out in [8]. The loss of accuracy does not result from accumulative errors in integration, but it is caused by the subtraction of almost equal numbers in the process of determination of the unknown boundary values. It follows that for every set of geometric and material parameters of the shell there is a critical length beyond which the solution loses all accuracy. The advantage of the finite-difference approach over direct integration is that it can avoid such a loss of accuracy. It is concluded from [8] that if the solution of the system of algebraic equations, which result from the finite-difference equations, is obtained by means of Gaussian elimination, then no loss of accuracy is experienced if the length of the shell is increased.

This paper is concerned with the general problem of deformation of thin, elastic shells of revolution, symmetrically or nonsymmetrically loaded, and with the development of a numerical method of its solution, which employs the direct integration technique, but eliminates the loss of accuracy owing to the length of the shell. The method developed here is applicable to any two-point boundary-value problem which is governed within an interval by a system of m first-order linear ordinary differential equations together with $m/2$ boundary conditions prescribed at each end of the interval. It is shown that the boundary-value problem of a rotationally symmetric shell can be stated in this form for any consistent linear bending theory of shells in terms of those quantities which appear in the natural boundary conditions on a rotationally symmetric edge.

The method of this paper offers definite advantages over the finite-difference approach. The main advantages are: (*a*) It can be applied conveniently to a large system of first-order differential equations, and (*b*) it permits an automatic selection of an optimum step size of integration at each step according to the desired accuracy of the solution. The first point means that the equations of the theory of shells of revolution, characterized in terms of first-order differential equations, can be integrated directly, and further reduction of the equations to a smaller number of unknowns is not necessary. The second point seems to be of great importance if a truly general method is desired which is expected to hold for arbitrary loads, shell configurations, thickness, and so on. With the finite-difference approach, a meaningful *a priori* estimate of the step size is often difficult, if not impossible, especially when rapid changes and discontinuities in the shell parameters are encountered. If a predictor-corrector direct integration approach is employed with the method of this paper, then the step size can be selected automatically at each step which ensures a prescribed accuracy of the solution and optimum efficiency in the calculation.

The method given in this paper can be divided into two parts: (*a*) Direct integration of $m + 1$ initial value problems over preselected segments of the total interval, and (*b*) the use of Gaussian elimination for the solution of the resulting system of matrix equations. The first part of this method is a generalization of that which is employed over the whole interval in [2–5]. Here, however, the initial value problems are defined over segments of the total interval, the lengths of which are within the range of the applicability of the direct integration approach. After the initial value problems are integrated over these segments, continuity conditions on all variables are written at the endpoints of the segments, and they constitute a simultaneous system of linear matrix equations. This system of matrix equations is then solved directly by means of Gaussian elimination. The result is that the direct integration method is employed and at the same time there is no loss of accuracy because the lengths of the segments are selected in such a way that the solutions of the initial value problems are kept sufficiently small. A convenient parameter is given from which the appropriate lengths of the segments can be estimated easily.

In the application of this method to the analysis of rotationally symmetric shells, the boundary-value problem is formulated in terms of first-order ordinary differential equations. For this purpose, starting with the equations of the linear classical bending theory of shells in which the thermal effects are included, first a system of equations is derived in the form of eight partial differential equations involving eight unknowns in such a manner that the system of equations contains no derivatives of the material parameters, thickness, or principal radii of curvature. The absence of the derivatives in the coefficients of the differential equations permits the calculation of the coefficients at a point without regard to the values of the shell parameters at preceding or following points. Then, assuming separability with respect to the independent variables, the desired system of eight first-order ordinary differential equations is obtained which together with the boundary conditions on two edges of the shell constitute a two-point boundary-value problem. The derived system of equations is applicable to rotationally symmetric shells with arbitrary meridional variations (including discontinuities) in Young's modulus, Poisson's ratio, radii of curvature, thickness and coefficient of thermal expansion. While such a system of equations is derived in this paper only for one version of the classical theory of shells, it can be derived in the same way for all other consistent linear bending theories of shells, including those which account for the dynamic effects, transverse shear deformation, nonhomogeneity, and anisotropy.

Finally, with the use of the method and the equations given in this paper, stresses and displacements are calculated in a thin-walled torus subjected to internal pressure. The solution shows that the meridional membrane stress is almost identical to that predicted by membrane theory, but that the bending stresses even for a relatively thin torus may not be negligible.

Geometry and Basic Equations

The position of a point of a shell of revolution is given by the coordinates θ, ϕ, ζ measured along the triplet of unit vectors t_ϕ, t_θ, n, respectively, as shown in Fig. 1. The shape of the shell is determined by specifying the two principal radii of curvature R_ϕ, R_θ of the middle surface as functions of ϕ. Instead of R_θ, it is convenient to use the distance r from a point on the middle surface to the z-axis; from Fig. 1 it follows that

$$r = R_\theta \sin \phi \tag{1}$$

If the generating curve of the middle surface is given by $r = r(z)$ then

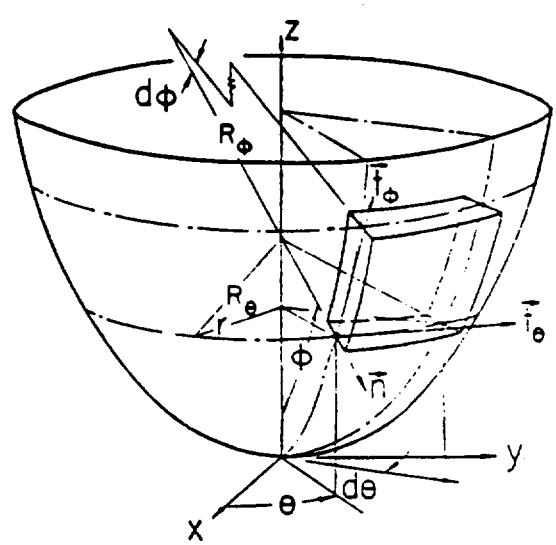

Fig. 1 Element of a shell of revolution

$$R_\phi = -\left[1 + \left(\frac{dr}{dz}\right)^2\right]^{3/2} \Big/ \frac{d^2r}{dz^2}$$

$$R_\theta = r\left[1 + \left(\frac{dr}{dz}\right)^2\right]^{1/2} \tag{2}$$

The following analysis requires frequent differentiation of r (or R_θ) with respect to ϕ, and it is convenient to express this derivative by the Codazzi relation

$$\frac{dr}{d\phi} = R_\phi \cos\phi \tag{3}$$

The displacement components of the middle surface of the shell and the rotations of the normal are defined by the expression of the displacement vector U of the form

$$\mathbf{U} = (u_\phi + \zeta\beta_\phi)\mathbf{t}_\phi + (u_\theta + \zeta\beta_\theta)\mathbf{t}_\theta + w\mathbf{n} \tag{4a}$$

The shell is subjected to the mechanical load vector p, which is measured as force per unit area of the middle surface and written as

$$\mathbf{p} = p_\phi\mathbf{t}_\phi + p_\theta\mathbf{t}_\theta + p\mathbf{n} \tag{4b}$$

and the moment vector m, which is measured as moment per unit area and given by

$$\mathbf{m} = -m_\phi\mathbf{t}_\phi + m_\theta\mathbf{t}_\theta \tag{4c}$$

With reference to Fig. 1, equations (4) serve the purpose for establishing the positive directions of the components of the displacement and mechanical load vectors.

The temperature distribution in the shell caused by some thermal loads is accounted for in the usual manner by means of the integrated temperature effect of the form

$$T_0(\phi, \theta) = \frac{1}{h}\int_{-\frac{h}{2}}^{\frac{h}{2}} T(\phi, \theta, \zeta)d\zeta \tag{5a}$$

$$T_1(\phi, \theta) = \frac{12}{h^2}\int_{-\frac{h}{2}}^{\frac{h}{2}} \zeta T(\phi, \theta, \zeta)d\zeta \tag{5b}$$

The derivation of a new set of equations carried out in the next section is based on a linear classical theory of shells given by Reissner [13]. When referred to arbitrary shells of revolution, the governing system of equations of [13] can be written in the following form. Equations of equilibrium:

$$N_{\theta,\theta} + \frac{r}{R_\phi}N_{\phi\theta,\phi} + 2\cos\phi\, N_{\theta\phi} + Q_\theta \sin\phi + rp_\theta = 0 \tag{6a}$$

$$N_{\theta\phi,\theta} + \frac{r}{R_\phi}N_{\phi,\phi} + (N_\phi - N_\theta)\cos\phi + \frac{r}{R_\phi}Q_\phi + rp_\phi = 0 \tag{6b}$$

$$Q_{\theta,\theta} + \frac{r}{R_\phi}Q_{\phi,\phi} + Q_\phi\cos\phi - N_\theta\sin\phi - \frac{r}{R_\phi}N_\phi + rp = 0 \tag{7}$$

$$M_{\theta,\theta} + \frac{r}{R_\phi}M_{\phi\theta,\phi} + 2\cos\phi\, M_{\theta\phi} - rQ_\theta + rm_\theta = 0 \tag{8a}$$

$$M_{\theta\phi,\theta} + \frac{r}{R_\phi}M_{\phi,\phi} + (M_\phi - M_\theta)\cos\phi - rQ_\phi + rm_\phi = 0 \tag{8b}$$

Stress-strain relations:

$$N_\theta = K(\epsilon_\theta + \nu\epsilon_\phi) - (1 + \nu)\alpha K T_0 \tag{9a}$$

$$N_\phi = K(\epsilon_\phi + \gamma\epsilon_\theta) - (1 + \nu)\alpha K T_0 \tag{9b}$$

$$N_{\theta\phi} = N_{\phi\theta} = (1 - \nu)\epsilon_{\theta\phi} \tag{9c}$$

$$M_\theta = D(\kappa_\theta + \nu\kappa_\phi) - (1 + \nu)\alpha D T_1 \tag{10a}$$

$$M_\phi = D(\kappa_\phi + \nu\kappa_\theta) - (1 + \nu)\alpha D T_1 \tag{10b}$$

$$M_{\theta\phi} = M_{\phi\theta} = (1 - \nu)D\kappa_{\theta\phi} \tag{10c}$$

Strain-displacement relations:

$$\epsilon_\theta = \frac{1}{r}(u_{\theta,\theta} + u_\phi\cos\phi + w\sin\phi) \tag{11a}$$

$$\epsilon_\phi = \frac{1}{R_\phi}(u_{\phi,\phi} + w) \tag{11b}$$

$$2\epsilon_{\theta\phi} = \frac{1}{r}(u_{\phi,\theta} - u_\theta\cos\phi) + \frac{1}{R_\phi}u_{\theta,\phi} \tag{11c}$$

$$\kappa_\theta = \frac{1}{r}(\beta_{\theta,\theta} + \beta_\phi\cos\phi) \tag{12a}$$

$$\kappa_\phi = \frac{1}{R_\phi}\beta_{\phi,\phi} \tag{12b}$$

$$2\kappa_{\theta\phi} = \frac{1}{r}(\beta_{\phi,\theta} - \beta_\theta\cos\phi) + \frac{1}{R_\phi}\beta_{\theta,\phi} \tag{12c}$$

$$\beta_\theta = -\frac{1}{r}w_{,\theta} + \frac{\sin\phi}{r}u_\theta \tag{13a}$$

$$\beta_\phi = -\frac{1}{R_\phi}w_{,\phi} + \frac{1}{R_\phi}u_\phi \tag{13b}$$

The positive directions of the stress resultants in the foregoing equations are the same as the corresponding stresses on the edge of the shell. The definitions of the stress resultants are found in [13].

The order of the system of equations (6)–(13) is eight with respect to ϕ, and consequently it is possible to reduce (6)–(13) to eight first-order differential equations which involve eight unknowns. If the eight unknowns are those quantities which enter into the natural boundary conditions at the edge ϕ = const, then the boundary-value problem of a rotationally symmetric shell can be completely stated in terms of these unknowns. For this reason, the eight differential equations, derived in the following sections, and the eight unknowns are called the fundamental set of equations and the fundamental variables, respectively.

Derivation of Fundamental Set of Equations

According to the classical theory of shells, the quantities which appear in the natural boundary conditions on a rotationally symmetric edge of a shell of revolution include the effective shear resultants N and Q defined by

$$N = N_{\theta\phi} + \frac{\sin\phi}{r}M_{\theta\phi} \tag{14a}$$

$$Q = Q_\phi + \frac{1}{r}M_{\theta\phi,\theta} \tag{14b}$$

Thus, the fundamental variables, which are consistent with the theory of [13], are the four generalized displacements u_θ, u_ϕ, w, and β_ϕ and the four generalized forces Q, N_ϕ, N, and M_ϕ.

In the derivation of the fundamental equations, it is more convenient to employ the distance s, measured along the meridian of the shell, rather than the angular coordinate ϕ. However, after the equations are derived, the problem can again be easily formulated in terms of ϕ by means of the relation

$$\frac{1}{R_\phi}\frac{\partial}{\partial\phi} = \frac{\partial}{\partial s}$$

As a preliminary step, it is necessary to express N_θ, M_θ, $M_{\theta\phi}$ in terms of the fundamental variables. From (9a) it follows that

$$\nu N_\phi + K\frac{1-\nu^2}{r}(w\sin\phi + u_{\theta,\theta} + u_\phi\cos\phi) - \alpha K(1-\nu^2)T_0 \quad (15)$$

and from (10a) that

$$M_\theta = \nu M_\phi + D\frac{1-\nu^2}{r}\left(-\frac{1}{r}w_{,\theta\theta} + \frac{\sin\phi}{r}u_{\theta,\theta} + \beta_\phi\cos\phi\right) - \alpha D(1-\nu^2)T_1 \quad (16)$$

Elimination of $u_{\theta,s}$ and $w_{,\theta s}$ from equation (12c) leads to an expression for $M_{\theta\phi}$ in the form

$$M_{\theta\phi} = LD\frac{1-\nu}{2r}\left[2\beta_{\phi,\theta} + \frac{2\cos\phi}{r}w_{,\theta} + Hu_\theta\cos\phi - Ju_{\phi,\theta}\right] + \frac{LD}{K}\frac{\sin\phi}{r}N \quad (17)$$

where

$$L = \frac{1}{1 + \frac{\sin^2\phi}{r^2}\frac{D}{K}}$$

In the derivation of the four equations of the fundamental set which involve the derivatives of the stress resultants with respect to s, the use of (14) is essential. Elimination of Q_θ from (6a) and (8a) by means of (14a) leads to

$$H\frac{\cos\phi}{r}M_{\theta\phi} - \frac{2\cos\phi}{r}N - \frac{1}{r}N_{\theta,\theta} - \frac{\sin\phi}{r^2}M_{\theta,\theta} - p_\theta - \frac{\sin\phi}{r}m_\theta \quad (18)$$

Similarly, elimination of Q_θ from (7) and (8a) gives

$$Q_{,s} = -\frac{2\cos\phi}{r^2}M_{\theta\phi,\theta} - \frac{\cos\phi}{r}Q + \frac{\sin\phi}{r}N_\theta + \frac{1}{R_\phi}N_\phi - \frac{1}{r^2}M_{\theta,\theta\theta} - p - \frac{1}{r}m_{\theta,\theta} \quad (19)$$

Solving (6b) from $N_{\phi,s}$ there results

$$N_{\phi,s} = -\frac{1}{r}N_{,\theta} + \frac{1}{r}JM_{\theta\phi,\theta} + \frac{\cos\phi}{r}(N_\theta - N_\phi) - \frac{1}{R_\phi}Q - p_\phi \quad (20)$$

and it follows from (8b) that

$$M_{\phi,s} = -\frac{2}{r}M_{\theta\phi,\theta} + \frac{\cos\phi}{r}(M_\theta - M_\phi) + Q - m_\phi \quad (21)$$

Wherever necessary, $N_{\theta\phi}$ and Q_ϕ were eliminated with the use of (14).

The fundamental set of equations consists of (18)–(21), where N_θ, M_θ, $M_{\theta\phi}$ can be replaced directly in terms of the fundamental variables by means of (15)–(17), and four additional equations giving the derivatives of w, u_ϕ, u_θ, β_ϕ with respect to s, which are obtained from (13b), (11c), (11b), (12b), respectively. Finally, the system of eight differential equations that governs the deformation of a shell of revolution can be expressed in terms of the eight fundamental variables and written as

$$w_{,s} = \frac{1}{R_\phi}u_\phi - \beta_\phi \quad (22a)$$

$$u_{\phi,s} = -Uw - \frac{\nu\cos\phi}{r}u_\phi - \frac{\nu}{r}u_{\theta,\theta} + \frac{1}{K}N_\phi + \alpha(1-\nu)T_1 \quad (22b)$$

$$u_{\theta,s} = -\frac{LD\sin 2\phi}{Kr^2}w_{,\theta} - \frac{1}{r}\left(1 - \frac{LDJ\sin\phi}{Kr}\right)u_{\phi,\theta} + \frac{\cos\phi}{r}\left(1 - \frac{LDH\sin\phi}{Kr}\right)u_\theta - \frac{2LD\sin\phi}{Kr^2}\beta_{\phi,\theta} + \frac{2}{(1-\nu)K}\left(1 - \frac{LD\sin^2\phi}{Kr^2}\right)N \quad (22c)$$

$$\beta_{\phi,s} = \frac{\nu}{r^2}w_{,\theta\theta} - \frac{\nu\sin\phi}{r^2}u_{\theta,\theta} - \frac{\nu\cos\phi}{r}\beta_\phi + \frac{1}{D}M_\phi + \alpha(1+\nu)T_1 \quad (22d)$$

$$\begin{aligned} Q_{,s} = {} & \frac{1-\nu}{r^4}\left[D(1+\nu)\frac{\partial^4}{\partial\theta^4} - 2LD\cos^2\phi\frac{\partial^2}{\partial\theta^2} + (1+\nu)Kr^2\sin^2\phi\right]w + (1-\nu)\frac{\cos\phi}{r^2}\left[\frac{1}{r}LDJ\frac{\partial^2}{\partial\theta^2} + (1+\nu)K\sin\phi\right]u_\phi \\ & - \frac{1-\nu}{r^2}\left[\frac{1}{r}LDH\cos^2\phi - (1+\nu)K\sin\phi + D(1+\nu)\frac{\sin\phi}{r^2}\frac{\partial^2}{\partial\theta^2}\right]u_{\theta,\theta} \\ & - D(1-\nu)\frac{\cos\phi}{r^3}(1+\nu+2L)\beta_{\phi,\theta\theta} + UN_\phi - \frac{\nu}{r^2}M_{\phi,\theta\theta} \\ & - \frac{LD\sin 2\phi}{Kr^3}N_{,\theta} - \frac{\cos\phi}{r}Q - p - \frac{1}{r}m_{\theta,\theta} \\ & - \alpha(1-\nu^2)\frac{1}{r}\left(K\sin\phi\,T_0 - \frac{1}{r}DT_{1,\theta\theta}\right) \end{aligned} \quad (22e)$$

$$\begin{aligned} N_{\phi,s} = {} & (1-\nu)\frac{\cos\phi}{r^2}\left[\frac{1}{r}LDJ\frac{\partial^2}{\partial\theta^2} + (1+\nu)K\sin\phi\right]w \\ & + \frac{1-\nu}{r^2}\left[(1+\nu)K\cos^2\phi - \tfrac{1}{2}LDJ^2\frac{\partial^2}{\partial\theta^2}\right]u_\phi \\ & + (1-\nu)\frac{\cos\phi}{r^2}\left[\tfrac{1}{2}LDJH + (1+\nu)K\right]u_{\theta,\theta} + JLD\frac{1-\nu}{r^2}\beta_{\phi,\theta\theta} \\ & - \frac{1}{R_\phi}Q - (1-\nu)\frac{\cos\phi}{r}N_\phi - \frac{1}{r}\left(1 - \frac{LDJ\sin\phi}{Kr}\right)N_{,\theta} \\ & - p_\phi - \alpha(1-\nu^2)K\frac{\cos\phi}{r}T_0 \end{aligned} \quad (22f)$$

$$\begin{aligned} N_{,s} = {} & \frac{1-\nu}{r^2}\left[HLD\frac{\cos^2\phi}{r} - (1+\nu)K\sin\phi + (1+\nu)D\frac{\sin\phi}{r^2}\frac{\partial^2}{\partial\theta^2}\right]w_{,\theta} \\ & - (1-\nu)\frac{\cos\phi}{r^2}\left[\tfrac{1}{2}LDJH + (1+\nu)K\right]u_{\phi,\theta} \\ & + \frac{1-\nu}{r^2}\left[\tfrac{1}{2}LDH^2\cos^2\phi - (1+\nu)\left(K + \frac{D\sin^2\phi}{r^2}\right)\frac{\partial^2}{\partial\theta^2}\right]u_\theta \\ & - D(1-\nu)\frac{\cos\phi}{r^2}\left[(1+\nu)\frac{\sin\phi}{r} - LH\right]\beta_{\phi,\theta} - \frac{\nu}{r}N_{\phi,\theta} \end{aligned}$$

$$- \frac{\cos\phi}{r}\left(2 - \frac{LDH\sin\phi}{Kr}\right) N - \frac{\sin\phi}{r^2} M_{\phi,\theta} - p_\theta - \frac{\sin\phi}{r} m_\theta$$

$$+ \alpha(1-\nu^2)\frac{1}{r}\left(KT_{0,\theta} + D\frac{\sin\phi}{r} T_{1,\theta}\right) \quad (22g)$$

$$M_{\phi,s} = -(1-\nu)D\frac{\cos\phi}{r^2}(1+\nu+2L)w_{,\theta\theta} + LDJ\frac{1-\nu}{r^2} u_{\phi,\theta\theta}$$

$$+ D(1-\nu)\frac{\cos\phi}{r^2}\left[(1+\nu)\frac{\sin\phi}{r} - HL\right] u_{\theta,\theta}$$

$$+ D\frac{1-\nu}{r^2}\left[(1+\nu)\cos^2\phi - 2L\frac{\partial^2}{\partial\theta^2}\right]\beta_\phi + Q - \frac{2LD\sin\phi}{Kr^2} N_{,\theta}$$

$$- (1-\nu)\frac{\cos\phi}{r} M_\phi - m_\phi - \alpha(1-\nu^2)D\frac{\cos\phi}{r} T_1 \quad (22h)$$

Equations (22), (14), and (15) to (17) determine all unknown variables except Q_θ which can be found from (8a) and written in the form

$$Q_\theta = \frac{1}{r} M_{\theta,\theta} + M_{\theta\phi,s} + \frac{2\cos\phi}{r} M_{\theta\phi} + m_\theta \quad (23)$$

By calculating $M_{\theta\phi,s}$ from (17) and making use of (16), it is possible to express Q_θ directly in terms of the fundamental variables. This expression is lengthy and contains derivatives with respect to s of the shell parameters. Since Q_θ does not enter into any boundary conditions on the edge s = const, it is preferable to calculate Q_θ as the last unknown directly from (23). The derivative of $M_{\theta\phi}$ can be easily obtained by numerical differentiation.

The procedure for the derivation of an equivalent set of equations for other linear classical theories of isotropic shells is identical to that given before. For general anisotropic and/or nonhomogeneous shells of revolution with rotationally symmetric properties, the fundamental set of equations is derived in the same way as (22) except that (9) and (10) must be replaced by the appropriate stress-strain relations given, for example, by Ambartsumyan [14]. Otherwise, the derivation is straightforward. For the improved theory of shells, such as the one given by Naghdi [15], in which the effects of transverse-shear deformation are accounted for, the following ten fundamental variables are required: w, u_ϕ, u_θ, β_ϕ, β_θ, Q_ϕ, N_ϕ, $N_{\phi\theta}$, M_ϕ, $M_{\phi\theta}$. Since now Q_ϕ and Q_θ appear in (13), the elimination of Q_θ from (6a), (7), (8a), is done by means of (13a). The required equations for the derivatives of the generalized forces are obtained directly from the five equations of equilibrium (6), (7), (8). The remaining five equations are derived by following a procedure similar to that of the foregoing.

Fundamental Equations for Separable Solutions

For shells of revolution which consist of complete latitude circles, the surface loads are periodic with respect to θ with a period of 2π, and they can be assumed to be of the form

$$\{p_\phi, p_\theta, m_\phi\} = \{p_{\phi n}, p_{\theta n}, m_{\phi n}\}\begin{Bmatrix}\cos n\theta\\ \sin n\theta\end{Bmatrix} \quad (24a)$$

$$\{T_0, T_1\} = \{T_{0n}, T_{1n}\}\begin{Bmatrix}\cos n\theta\\ \sin n\theta\end{Bmatrix} \quad (24b)$$

$$\{p_\theta, m_\theta\} = \{p_{\theta n}, m_{\theta n}\}\begin{Bmatrix}\sin n\theta\\ \cos n\theta\end{Bmatrix} \quad (24c)$$

where the variables with subscripts n depend only on s, and each integral value of n in (24) can be regarded as one Fourier component in a general Fourier series expansion of arbitrary periodic surface loads.

Separable solutions [illegible] 24) are then obtained in the form

$$\{w, u_\phi, \beta_\phi\} = \{w_n, u_{\phi n}, \beta_{\phi n}\}\begin{Bmatrix}\cos n\theta\\ \sin n\theta\end{Bmatrix} \quad (25a)$$

$$\{N_\phi, M_\phi, Q\} = \{N_{\phi n}, M_{\phi n}, Q_n\}\begin{Bmatrix}\cos n\theta\\ \sin n\theta\end{Bmatrix} \quad (25b)$$

$$\{u_\theta, N\} = \{u_{\theta n}, N_n\}\begin{Bmatrix}\sin n\theta\\ \cos n\theta\end{Bmatrix} \quad (25c)$$

The s-dependent coefficients with subscripts n on the right-hand side of (25) are governed by a system of equations which is obtained from (22) and, after using the assumption that the shell is thin,[3] can be written as

$$w_{n,s} = \frac{1}{R_\phi} u_{\phi n} - \beta_{\phi n} \quad (26a)$$

$$u_{\phi n,s} = -Uw_n - \frac{\nu\cos\phi}{r} u_{\phi n} \mp \frac{\nu n}{r} u_{\theta n} + \frac{1}{K} N_{\phi n} + \alpha(1+\nu)T_{0n} \quad (26b)$$

$$u_{\theta n,s} = \pm\frac{D\sin 2\phi}{Kr^2} w_n \pm \frac{n}{r} u_{\phi n} + \frac{\cos\phi}{r} u_{\theta n} \pm \frac{2Dn\sin\phi}{Kr^2}\beta_{\phi n} + \frac{2}{(1-\nu)K} N \quad (26c)$$

$$\beta_{\phi n,s} = -\frac{\nu n^2}{r^2} w_n \mp \frac{\nu n\sin\phi}{r^2} u_{\theta n} - \frac{\nu\cos\phi}{r}\beta_{\phi n} + \frac{1}{D} M_{\phi n} + \alpha(1+\nu)T_{1n} \quad (26d)$$

$$Q_{n,s} = \frac{1-\nu}{r^4}\{(1+\nu)n^4 D + 2n^2 D\cos^2\phi + (1+\nu)Kr^2\sin^2\phi\}w_n$$

$$+ (1-\nu)\frac{\cos\phi}{r^2}\left[(1+\nu)K\sin\phi - \frac{n^2}{r}DJ\right]u_{\phi n}$$

$$\pm\frac{(1-\nu)n}{r^2}\left[(1+\nu)D\frac{n^2}{r^2}\sin\phi + (1+\nu)K\sin\phi\right]u_{\theta n}$$

$$+ n^2(1-\nu)(3+\nu)D\frac{\cos\phi}{r^2}\beta_{\phi n} - \frac{\cos\phi}{r} Q_n + UN_{\phi n}$$

$$\mp\frac{nD\sin 2\phi}{Kr^2} N_n + \frac{\nu n^2}{r^2} M_{\phi n} - p_n \mp \frac{n}{r} m_{\theta n}$$

$$- \alpha(1-\nu^2)\frac{1}{r}\left(K\sin\phi\, T_{0n} + D\frac{n^2}{r} T_{1n}\right) \quad (26e)$$

$$N_{\phi n,s} = (1-\nu)\frac{\cos\phi}{r^2}\left[(1+\nu)K\sin\phi - \frac{n^2}{r}JD\right]w_n$$

$$+ \frac{1-\nu}{r^2}\left[(1+\nu)K\cos^2\phi + \frac{n^2}{r}DJ^2\right]u_{\phi n}$$

$$\pm\frac{(1-\nu^2)nK\cos\phi}{r^2} u_{\theta n} - \frac{n^2(1-\nu)}{r^2} DJ\beta_{\phi n}$$

$$- \frac{1}{R_\phi} Q_n - (1-\nu)\frac{\cos\phi}{r} N_{\phi n} = [illegible]$$

[3] In the derivation of the system of equations [illegible] the assumption is made that the shell is sufficiently thin, so that $1 - h^2/12R^2 \approx 1$, where R denotes the minimum principal radius of curvature. This same approximation is used to obtain the following equations from (22).

$$- p_{\phi n} - \alpha(1 - \nu^2)K \frac{\cos\phi}{r} T_{1n} \quad (26f)$$

$$N_{\theta n} = \pm \frac{n(1-\nu)}{r^2}\left[(1+\nu)D\frac{n^2}{r^2}\sin\phi + (1+\nu)K\sin\phi\right] w_n$$

$$= \frac{(1-\nu^2)nK\cos\phi}{r^2} u_{\phi n} + \frac{n^2(1-\nu^2)K}{r^2} u_{\theta n}$$

$$\pm nD\frac{1-\nu}{r^2}\cos\phi\left[(1+\nu)\frac{\sin\phi}{r} - H\right]\beta_{\phi n}$$

$$\pm n\frac{\nu}{r} N_{\phi n} - \frac{2\cos\phi}{r} N_n$$

$$\pm \frac{\nu n\sin\phi}{r^2} M_{\phi n} - p_{\theta n} - \frac{\sin\phi}{r} m_{\theta n}$$

$$\mp \alpha(1-\nu^2)\frac{1}{r}\left(KT_{0n} + D\frac{\sin\phi}{r}T_{1n}\right) \quad (26g)$$

$$M_{\phi n,s} = n^2(1-\nu)(3+\nu)D\frac{\cos\phi}{r^2} w_n - n^2\frac{1-\nu}{r^2} JDu_{\phi n}$$

$$\pm nD\frac{1-\nu}{r^2}\cos\phi\left[(1+\nu)\frac{\sin\phi}{r} - H\right] u_{\theta n}$$

$$+ D\frac{1-\nu}{r^2}[(1+\nu)\cos^2\phi + 2n^2]\beta_{\phi n} + Q \mp \frac{2nD\sin\phi}{Kr^2} N_n$$

$$- (1-\nu)\frac{\cos\phi}{r} M_{\phi n} - m_{\phi n} - \alpha(1-\nu^2)D\frac{\cos\phi}{r} T_{1n} \quad (26h)$$

The double signs in (26) correspond to the top or bottom trigonometric function employed in (24) and (25).

The quantities which are not included in the fundamental variables can be expressed by means of separation of variables by

$$\{N_\theta, M_\theta, Q_\phi\} = \{N_{\theta n}, M_{\theta n}, Q_{\phi n}\}\begin{Bmatrix}\cos n\theta\\ \sin n\theta\end{Bmatrix} \quad (27a)$$

$$\{N_{\theta\phi}, M_{\theta\phi}, Q_\theta\} = \{N_{\theta\phi n}, M_{\theta\phi n}, Q_{\theta n}\}\begin{Bmatrix}\sin n\theta\\ \cos n\theta\end{Bmatrix} \quad (27b)$$

where the s-dependent coefficients with subscripts n must satisfy a set of equations obtained from equations (14)–(17) and (23) in the form

$$N_{\theta n} = \nu N_{\phi n} + (1-\nu^2)\frac{K}{r^2}(w_n\sin\phi + u_{\phi n}\cos\phi \pm nu_{\theta n}) - \alpha(1-\nu^2)KT_{0n} \quad (28a)$$

$$M_{\theta n} = \nu M_{\phi n} + (1-\nu^2)\frac{D}{r}\left(\frac{n^2}{r}w_n + \beta_{\phi n}\cos\phi \pm n\frac{\sin\phi}{r}u_{\theta n}\right) - \alpha(1-\nu^2)DT_{1n} \quad (28b)$$

$$M_{\theta\phi n} = D\frac{1-\nu}{2r}\left(\mp\frac{2n\cos\phi}{r}w_n \pm nJu_{\phi n} + H\cos\phi u_{\theta n} \mp 2n\beta_{\phi n}\right) + \frac{D}{K}\frac{\sin\phi}{r}N_n \quad (28c)$$

$$Q_{\theta n} = \mp\frac{n}{r}M_{\theta n} + M_{\theta\phi n,s} + \frac{2\cos\phi}{r}M_{\theta\phi n} + \cdots \quad (28d)$$

$$N_{\theta\phi n} = N_n - \frac{\sin\phi}{r}M_{\theta\phi n} \quad (28e)$$

$$Q_{\phi n} = Q_n \mp \frac{n}{r}M_{\theta\phi n} \quad (28f)$$

The double signs again correspond to the top or bottom trigonometric function employed in (24), (25), and (27).

The remainder of this paper is concerned with the solution of the system of equations (26), subject to the boundary conditions on two edges s = const. It should be noted that after the expansion of the loads in Fourier series, the solution to (26) is obtained for each integral value of n separately, and then the solutions are superimposed to form a Fourier series expansion for the unknown variables.

Reduction to Initial Value Problems

This section is concerned with the reduction of a two-point boundary-value problem governed by

$$\frac{dy(x)}{dx} = A(x)y(x) + B(x) \quad (29a)$$

to a series of initial-value problems. In (29a), $y(x)$ is an $(m, 1)$ matrix which represents m unknown functions; x is the independent variable; $A(x)$ denotes the (m, m) coefficient matrix; and $B(x)$ is the $(m, 1)$ matrix of the nonhomogeneous terms. The elements of $A(x)$ and $B(x)$ are given piecewise continuous functions of x. The object is to determine $y(x)$ in the interval $a \le x \le b$ subject to m boundary conditions stated in terms of linear combinations of $y(a)$ and $y(b)$ in the form

$$F_a y(a) + F_b y(b) = G \quad (29b)$$

where F_a, F_b are (m, m) matrices and G is an $(m, 1)$ matrix, which are known from the statement of the boundary conditions of the problem. It should be clear that the governing system of equations (26) derived in the preceding section is stated in the form of (29a), and that the appropriate boundary conditions for a shell of revolution can be expressed in the form of (29b).

Let the complete solution of (29a) be written as

$$y(x) = Y(x)C + Z(x) \quad (30)$$

where the $(m, 1)$ matrix C represents m arbitrary constants, and $Y(x)$ is an (m, m) and $Z(x)$ an $(m, 1)$ matrix which are defined as the homogeneous and particular solutions of (29a) in the form

$$\frac{dY(x)}{dx} = A(x)Y(x) \quad (31a)$$

$$\frac{dZ(x)}{dx} = A(x)Z(x) + B(x) \quad (31b)$$

The initial conditions for determining $Y(x)$ and $Z(x)$ are

$$Y(a) = I \quad (32a)$$

$$Z(a) = 0 \quad (32b)$$

where I is the unit matrix.

Evaluation of (30) at $x = a$ leads at once, in view of (32a, b), to $C = y(a)$, and then (30) at $x = b$ can be written as

$$y(b) = Y(b)y(a) + Z(b) \quad (33)$$

Together with (29b), equation (33) constitutes a system of $2m$ linear algebraic equations from which the $2m$ unknowns, $y(a)$ and $y(b)$, are determined. Once $y(a)$ is known, the solution at any value of x is obtained from (30) provided that the values of $Y(x)$ and $Z(x)$ at that particular x are stored. This completes the reduction of a two-point boundary-value problem defined by (29) to $m + 1$ initial-value problems given by (31, 32).

As stated in the introduction, the solution for shells obtained by means of this procedure suffers a complete loss of accuracy at some critical length of the interval. The reason for this phenomenon can be seen clearly from (33). When the initial-value problems defined by (31, 32) are solved with the use of the equa-

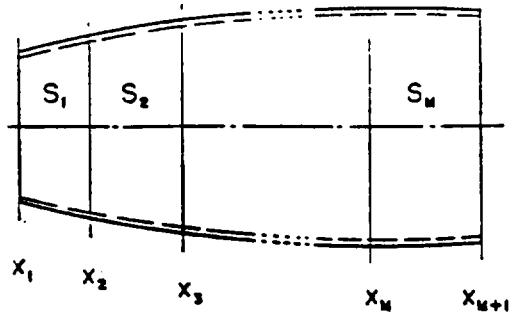

Fig. 2 Notation for division of total interval into segments

tions (26) for shells of revolution, it is observed that the elements of $Y(x)$ and $Z(x)$ increase in magnitude in such a way that if the length is increased by any factor n, then these solutions increase in magnitude approximately exponentially with n.

Consider, for example, the axisymmetric case when the deformation in the shell is caused by some prescribed edge conditions at $x = a$, say, by $M_\phi(a) = 1$ and $N_\phi(a) = Q(a) = 0$. It is reasonable to expect that the corresponding solutions at $x = b$ become smaller and smaller when the interval (a, b) is increased in length. The connection between $y(b)$ and $y(a)$ is given by the matrix equation (33) with the following magnitudes of the elements: $y(b)$-small, $Y(b)$-large, $y(a)$-unity. Clearly, the only way that the matrix product of (33) can give small values of $y(b)$ is that a number of significant digits of the large values of $Y(b)$ subtract out. When the length of the interval is increased, $Y(b)$ increase, while $y(b)$ decrease, and invariably all accuracy is lost at some critical length because all significant digits of $Y(b)$ in (33) are lost. This simple example serves as an illustration for the loss of accuracy encountered in the analysis of shells if the foregoing reduction technique is employed.

A convenient length factor, defined by

$$\beta = l[3(1 - \nu^2)]^{1/4}/(Rh)^{1/2} \tag{34}$$

where l is the length of the meridian of the shell and R is a minimum radius of curvature, can be used for an approximate estimate of the critical length of the shell. If the solutions $Y(x)$ and $Z(x)$ are obtained with a six-digit accuracy, then the foregoing procedure gives good results in the range $\beta \leq 3 - 5$.

However, the loss of accuracy of the solution can be avoided and shells of revolution with much larger values of β can be analyzed by means of the direct integration technique if the multisegment method given in the next section is employed.

Multisegment Method of Integration

Let the shell be divided into M-segments (denoted by S_i, where $i = 1, 2, \ldots, M$) of arbitrary length in each of which $\beta \leq 3$. Denote the coordinates of the ends of the segments by $x = x_i$, where the left-hand edge of the shell is at $x = x_1$ and the right-hand edge is at $x = x_{M+1}$, as shown in Fig. 2. In analogy to (30), the solution in the total interval $x_1 \leq x \leq x_{M+1}$ now can be written as

$$y(x) = Y_i(x)y(x_i) - Z_i(x) \tag{35}$$

where $Y_i(x)$ and $Z_i(x)$ denote the matrices corresponding to $Y(x)$ and $Z(x)$ in each segment $S_i(x_i \leq x \leq x_{i+1})$ and are given by

$$\frac{dY_i(x)}{dx} = A(x)Y_i(x) \tag{36a}$$

$$Y_i(x_i) = I \tag{36b}$$

$$\frac{dZ_i(x)}{dx} = A(x)Z_i(x) + B(x) \tag{36c}$$

$$Z_i(x_i) = 0 \tag{36d}$$

Requiring continuity of all elements of $y(x)$ at the points x_i, $i = 2, 3, \ldots, M + 1$, the following M-matrix equations are obtained from (35):

$$y(x_{i+1}) = Y_i(x_{i+1})y(x_i) - Z_i(x_{i+1}) \tag{37}$$

where $i = 1, 2, \ldots, M$. Equations (37) involve $M + 1$ unknown $(m, 1)$ matrices: $y(x_i)$, $i = 1, 2, \ldots, M + 1$. However, if the quantities prescribed at the edges of the shell are the fundamental variables, then the total number of unknowns is reduced by m, because $m/2$ elements of $y(x_1)$ and $m/2$ elements of $y(x_{M+1})$ are known. The same is true if the boundary conditions are stated in terms of linear combinations of the fundamental variables in the form of (29b). In this case, $y(x_1)$ and $y(x_{M+1})$ should be premultiplied by nonsingular (m, m) transformation matrices F_1 and F_{M+1}, respectively, so that the elements of the products contain the quantities prescribed at each edge. After eliminating $y(x_1)$ and $y(x_{M+1})$ from (37) by means of these products, it is concluded that (37) will retain its form if, after integration and before substitution into (37), $Y_1(x_2)$ is postmultiplied by F_1^{-1}, while $Y_M(x_{M+1})$ and $Z_M(x_{M+1})$ are premultiplied by F_{M+1}. In the following, it will be regarded that this transformation is carried out and that $y(x_1)$ and $y(x_{M+1})$ contain among their elements those quantities which are prescribed at $x = x_1$ and $x = x_{M+1}$, respectively.

Thus for all boundary conditions in the form of (29b), the system of M matrix equations (37) involves exactly M times m unknowns, and formally it can be solved by any method which is applicable to a large number of equations. However, the success of the procedure given in this paper lies in the application of Gaussian elimination directly on the matrix equations (37).

First a rearrangement of elements is performed. Since those $m/2$ elements of $y(x_1)$ and $y(x_{M+1})$ which are known through the boundary conditions can be any $m/2$ of the m-elements, it is necessary to rearrange the rows of $y(x_1)$ and $y(x_{M+1})$ so that the known elements are separated from the unknown elements. It is assumed here that the first $m/2$ elements of $y(x_1)$, denoted by $y_1(x_1)$, are known and that the last $m/2$ elements, denoted by $y_2(x_1)$, are unknown. On the other hand, $y_1(x_{M+1})$ are the unknown and $y_2(x_{M+1})$ are the known elements of $y(x_{M+1})$. Since the order of the variables in the column matrix $y(x)$ is arbitrary, it should be emphasized that this separation of elements does not involve any restriction on the boundary conditions, and that any natural boundary condition in the form of (29b) can be prescribed at each edge. The separation is achieved by a simple rearrangement of the columns of $Y_1(x_2)$ and the rows of $Y_M(x_{M+1})$ and $Z_M(x_{M+1})$ after integrating the initial-value problems defined by (36) to the ends of the segments S_1 and S_M and multiplying by F_1^{-1} and F_{M+1} as stated in the foregoing.

Once it is established which parts of $y(x_1)$ and $y(x_{M+1})$ are known, the continuity conditions (37) are rewritten as a partitioned matrix product of the form

$$\begin{bmatrix} y_1(x_{i+1}) \\ \hdashline y_2(x_{i+1}) \end{bmatrix} = \begin{bmatrix} Y_i^1(x_{i+1}) & Y_i^2(x_{i+1}) \\ \hdashline Y_i^3(x_{i+1}) & Y_i^4(x_{i+1}) \end{bmatrix} \begin{bmatrix} y_1(x_i) \\ \hdashline y_2(x_i) \end{bmatrix} + \begin{bmatrix} Z_i^1(x_{i+1}) \\ \hdashline Z_i^2(x_{i+1}) \end{bmatrix} \tag{38}$$

so that each of the equations (37) turns into a pair of equations given by

$$Y_i^1(x_{i+1})y_1(x_i) + Y_i^2(x_{i+1})y_2(x_i) - y_1(x_{i+1}) = -Z_i^1(x_{i+1})$$

$$Y_i^3(x_{i+1})y_1(x_i) + Y_i^4(x_{i+1})y_2(x_i) - y_2(x_{i+1}) = -Z_i^2(x_{i+1})$$

The result is a simultaneous system of $2M$ linear matrix equations, in which the known coefficients $Y_i^j(x_{i+1})$ and $Z_i^j(x_{i+1})$ are $(m/2, m/2)$ and $(m/2, 1)$ matrices, respectively, and the unknowns $y_j(x_i)$ are $(m/2, 1)$ matrices. Since $y_1(x_1)$ and $y_2(x_{M+1})$ are known, there are exactly $2M$ unknowns: $y_1(x_i)$, with $i = 2, 3, \ldots, M + 1$, and $y_2(x_i)$, with $i = 1, 2, \ldots, M$.

By means of Gaussian elimination, the system of equations (39) is first brought to the form

$$\begin{bmatrix} E_1 & -I & 0 & 0 & 0 & 0 \\ 0 & C_1 & -I & 0 & 0 & 0 \\ 0 & 0 & E_2 & -I & 0 & 0 \\ 0 & 0 & 0 & C_2 & -I & 0 \\ \hdashline 0 & 0 & 0 & 0 & E_M & -I \\ 0 & 0 & 0 & 0 & 0 & C_M \end{bmatrix} \begin{bmatrix} y_2(x_1) \\ y_1(x_2) \\ y_2(x_2) \\ y_1(x_M) \\ \hdashline y_2(x_M) \\ y_1(x_{M+1}) \end{bmatrix} = \begin{bmatrix} A_1 \\ B_1 \\ A_2 \\ B_2 \\ \hdashline A_M \\ B_M \end{bmatrix} \tag{40}$$

where the dots indicate the triangularized equations (39) with $i = 3, 4, \ldots, M - 1$. The $(m/2, m/2)$ matrices E_i, C_i are defined by

$$E_1 = Y_1^2 \tag{41a}$$

$$C_1 = Y_1^4 E_1^{-1} \tag{41b}$$

and for $i = 2, 3, \ldots, M$

$$E_i = Y_i^2 + Y_i^3 C_{i-1}^{-1} \tag{41c}$$

$$C_i = (Y_i^4 + Y_i^3 C_{i-1}^{-1}) E_i^{-1} \tag{41d}$$

The $(m/2, 1)$ matrices A_i, B_i are given by

$$A_1 = -Z_1^1 - Y_1^1 y_1(x_1) \tag{42a}$$

$$B_1 = -Z_1^2 - Y_1^3 y_1(x_1) - Y_1^4 E_1^{-1} A_1 \tag{42b}$$

and for $i = 2, 3, \ldots, M - 1$

$$A_i = -Z_i^1 - Y_i^3 C_{i-1}^{-1} B_{i-1} \tag{42c}$$

$$B_i = -Z_i^2 - Y_i^3 C_{i-1}^{-1} B_{i-1} - (Y_i^4 + Y_i^3 C_{i-1}^{-1}) E_i^{-1} A_i \tag{42d}$$

Finally, for the Mth segment

$$A_M = -Z_M^1 - Y_M^1 C_{M-1}^{-1} B_{M-1} \tag{42e}$$

$$= y_2(x_{M-1}) - Z_M^2 - Y_M^3 C_{M-1}^{-1} B_{M-1} - (Y_M^4 + Y_M^3 C_{M-1}^{-1}) E_M^{-1} A_M \tag{42f}$$

Brevity, in place of $Y_i^j(x_{i-1})$ and $Z_i^j(x_{i+1})$, the symbols Y_i^j and Z_i^j have been used.

By means of (41) and (42), the unknowns of (39) are obtained by

$$y_1(x_{M+1}) = C_M^{-1} B_M \tag{43a}$$

$$y_2(x_M) = E_M^{-1}[y_1(x_{M+1}) + A_M] \tag{43b}$$

and for $i = 1, 2, \ldots, M - 1$

$$y_1(x_{M-i+1}) = C_{M-i}^{-1}[y_2(x_{M-i+1}) + B_{M-i}] \tag{43c}$$

$$y_2(x_{M-i}) = E_{M-i}^{-1}[y_1(x_{M-i+1}) + A_{M-i}] \tag{43d}$$

It should be noted that (41)–(43) must be evaluated in succession, because each equation involves the result obtained by the preceding equation.

Once all the unknowns $y(x_i)$ are found, the fundamental variables are determined from (35) at any value of x at which the solutions $Y_i(x)$ and $Z_i(x)$ are stored during the integration of the initial-value problems of (36). The integration of (36) can be accomplished by means of any of the standard direct integration methods.

On the basis of the system of equations (26) given in an earlier section and the method of solution developed in the last two sections, the author has prepared a computer program[4] which has been applied to many shell configurations having large values of β and successfully tested against known results. One example of a pressurized torus with $\beta = 57$ is presented in the next section.

The program admits arbitrary meridional variations, including discontinuities in all shell parameters. It also admits ring loads in form of prescribed values of N_ϕ, M_ϕ, N, or Q at any value of ϕ on the shell. Such loads introduce discontinuities in the solution for the corresponding stress resultants, and they can be represented at every x_i by an $(m, 1)$ discontinuity matrix which is simply added to the matrix $Z_i(x_{i+1})$ on the right-hand side of (37). This feature is of great value if shell joints are considered. Any discontinuity, either in geometry or in loads, is easily handled by requiring that the end point of a segment coincides with the location of the discontinuity. Since integration is restarted at the beginning of each segment, the precise effect of the discontinuity is obtained. The program outputs all fundamental variables at a number of desired points within each segment, and it also computes the values of $y(x_i)$ twice; once from (43) and then from (35). If a certain number of significant figures of these values match, then the continuity conditions are known to be satisfied to the same number of figures. In this way, a convenient error estimate of the solution is obtained for every case.

[4] The program was written and all calculations were carried out by the author on the IBM 709 computer at the Yale Computer Center. The direct integration of (36) is performed by means of the Adams predictor-corrector method, which selects an optimum step size at every step according to a prescribed accuracy.

Example: Pressurized Torus

In this section the stresses and displacements are determined in a complete torus subjected to a constant internal pressure. It is well known that the solution of this problem, when obtained by means of the linear membrane theory of shells, has a discontinuity in the displacement field. It has been shown by Jordan [16] and by Sanders and Liepins [17] that a satisfactory solution with regard to the displacement field for a sufficiently thin shell can be obtained if the nonlinear membrane theory of shells is employed. Subsequently, Reissner [18] established bounds on certain parameters which show when the nonlinear membrane and when the linear bending theory is applicable. It seems worthwhile to give here the solution for a pressurized torus as predicted by the linear bending theory.

The geometry of the torus is shown in Fig. 3. With regard to the quantities employed in equations (26), the two necessary parameters for a torus are given as

$$R_\phi = b \tag{44a}$$

$$r = a + b \sin \phi \tag{44b}$$

Because of symmetry with respect to the plane XX, Fig. 3, the

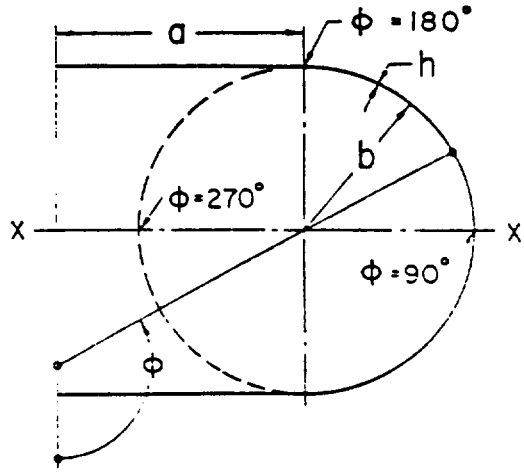

Fig. 3 Geometry of torus considered in example

Table 1 Stresses and displacements of a pressurized torus: $pb/Eh = 0.002$, $a/b = 1.5$, $\nu = 0.3$

ϕ \ h/b	$\sigma_{\phi m}/E \times 10^3$	$(\sigma_{\phi b}/E) \times 10^4$			$(w/b) \times 10^3$		
	0.005	0.05	0.02	0.005	0.05	0.02	0.005
90	1.601	−0.063	−0.031	−0.016	1.249	1.284	1.298
108	1.613	−0.188	−0.093	−0.019	1.261	1.315	1.328
126	1.650	−0.886	−0.123	−0.030	1.359	1.393	1.427
144	1.720	−1.915	−0.908	−0.020	1.786	1.507	1.625
162	1.832	−0.895	−1.378	−0.910	2.520	2.580	2.159
171	1.906	1.002	0.168	−0.605	3.467	3.493	3.297
180	1.990	3.089	2.277	1.482	3.994	4.334	4.815
184.5	2.042	3.890	3.035	1.968	4.150	4.576	5.248
189	2.104	4.270	3.119	1.520	4.208	4.637	5.151
193.5	2.175	4.178	2.580	0.530	4.156	4.509	4.693
198	2.254	3.610	1.589	−0.274	3.998	4.221	4.162
216	2.642	−0.587	−0.957	−0.079	2.652	2.527	2.481
234	3.168	−1.245	−0.291	−0.066	1.273	1.269	1.269
252	3.730	−0.717	−0.344	−0.077	0.416	0.417	0.414
270	3.997	−0.824	−0.331	−0.081	0.103	0.101	0.100

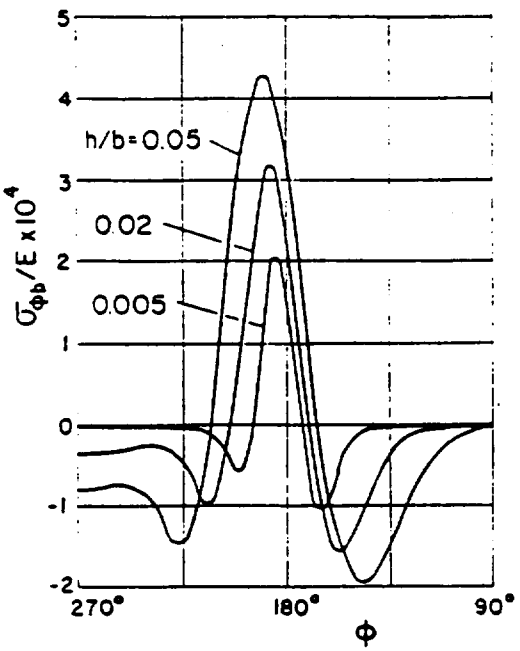

Fig. 4 Meridional bending stress $\sigma_{\phi b}$ at outer fiber versus meridional coordinate ϕ

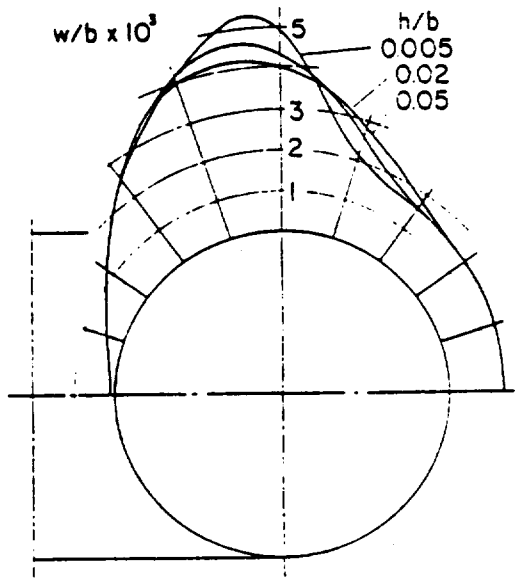

Fig. 5 Normal displacement w versus ϕ showing deformed section

integration of the initial-value problems is carried out from $\phi = 90°$ to $\phi = 270°$, and the boundary conditions at these endpoints are $u_\phi = \beta_\phi = Q = 0$. For the purpose of comparison with the results of [16] and [17], the load parameter is chosen as $pb/Eh = 0.002$ and $a/b = 1.5$.

The numerical values of the normal displacement, meridional membrane stress $\sigma_{\phi m} = N_\phi/h$, and meridional bending stress $\sigma_{\phi b} = 6M_\phi/h^2$ at $\zeta = h/2$ for a pressurized torus are shown in Table 1 and in Figs. 4 and 5. These results were taken from the output of the computer program prepared for an arbitrary shell of revolution after prescribing the geometric parameters as given by (44). The meridional membrane stress distribution agrees very well with that obtained in [17] by means of the membrane theory of shells and it shows only a small variation with h/b. The deformed shapes of the cross section of the torus shown in Fig. 5 for three values of h/b are in qualitative agreement with those given in [16] and [17], but their quantitative agreement cannot be expected because the values of h/b used in this example are outside the range where the bending effects are negligible. This is confirmed by the examination of the bending stresses shown in Fig. 4. The maximum value of $\sigma_{\phi b}$ occurs at $\phi = 189°$ for $h/b = 0.05$ and at $\phi = 184.5°$ for $h/b = 0.005$, which are also the points of maximum normal displacement and curvature as seen in Fig. 5. The comparison of the membrane and the maximum bending stress at various values of h/b is shown in Table 2.

Table 2 Maximum meridional bending stress and meridional membrane stress at $\phi = \phi_0$

h/b	0.05	0.02	0.005
ϕ_0	189°	189°	184.5°
$(\sigma_{\phi m}/E) \times 10^3$	2.053	2.082	2.042
$(\sigma_{\phi b}/E) \times 10^3$	0.427	0.312	0.197
$100\ (\sigma_{\phi b}/\sigma_{\phi m})$	20.8	15.0	9.6

It is of significance to note that even for the thickness ratio $h/b = 0.005$, which for many applications would be regarded as small, the maximum bending stress is about 10 percent of the membrane stress at the same point. Such effects of bending in a torus were previously noted by Clark [19], and they are also in agreement with the statement made by Goldenveizer [20] that when the middle surface touches a closed-plane curve, which in a torus corresponds to $\phi = 180°$, then in the vicinity of this curve bending stresses should be expected and the membrane theory is not applicable.

The boundary layer shown in Fig. 4 is also in agreement with the conclusions reached in [18] to the effect that when a and b given by

$$\mu = [12(1 - \nu^2)]^{1/2}(b/a)(b/h)$$

$$\rho = 12(1 - \nu^2)(p/E)(b/h)^3$$

are large compared to unity, then a boundary layer in the neighborhood of $\phi = 180°$ should be anticipated. For the present example, μ ranges from 44 to 440 and ρ from 9 to 874. However, since p is the only load parameter of the problem, the solutions shown in Figs. 4 and 5 are proportional to p, and the boundary layer remains unaffected if p alone is varied. Of course, for very large values of p the deformation of the torus may exceed the limits of a linear theory which according to [18] restrict ρ to the range $\rho \ll \mu^{1/2}$.

Acknowledgments

This research has been supported by the National Science Foundation Grant #23922. Many ideas leading to this paper originated from the consulting work performed by the author for the United Technology Center, Sunnyvale, California. The author wishes to thank the staff of the Applied Mechanics Department of UTC for many illuminating discussions concerning this subject.

References

1 P. M. Naghdi and C. N. DeSilva, "Deformation of Elastic Ellipsoidal Shells of Revolution," *Proceedings of the Second U. S. National Congress of Applied Mechanics*, 1954, pp. 333–343.

2 W. Lohmann, "Beitrag zur Integration der Reissner-Meissnerschen Schalengleichung für Behälter unter konstantem Innerdruck," *Ingenieur-Archiv*, vol. 6, 1935, pp. 338–346.

3 H. Münz, "Ein Integrationsverfahren für die Berechnung der Biegespannungen achsensymmetrischer Schalen unter achsensymmetrischer Belastung," *Ingenieur-Archiv*, vol. 19, 1951, pp. 103–117, 255–270.

4 E. Klingbeil, "Zur Theorie der Rotationsschalen vom Standpunkt numerischer Rechnungen," *Ingenieur-Archiv*, vol. 27, 1959, pp. 242–249.

5 G. D. Galletly, W. T. Kyner, and C. E. Moller, "Numerical Methods and the Bending of Ellipsoidal Shells," *Journal of the Society of Industrial and Applied Mathematics*, vol. 9, 1961, pp. 489–513.

6 R. K. Penny, "Symmetric Bending of the General Shell of Revolution by Finite Difference Method," *Journal of Mechanical Engineering Science*, vol. 3, 1961, pp. 369–377.

7 P. P. Radkowski, R. M. Davis, and M. R. Bolduc, "Numerical Analysis of Equations of Thin Shells of Revolution," *American Rocket Society Journal*, vol. 32, 1962, pp. 36–41.

8 W. K. Seperoski, C. E. Pearson, I. W. Dingwell, and A. W. Adkins, "A Digital Computer Program for the General Axially Symmetric Thin-Shell Problem," JOURNAL OF APPLIED MECHANICS, vol. 29, TRANS. ASME, vol. 84, Series E, 1962, pp. 655–661.

9 B. Budiansky and P. P. Radkowski, "Numerical Analysis of Unsymmetrical Bending of Shells of Revolution," *AIAA Journal*, vol. 1, 1963, pp. 1833–1842.

10 J. E. Goldberg and J. L. Bogdanoff, "Static and Dynamic Analysis of Nonuniform Conical Shells under Symmetrical and Unsymmetrical Conditions," *Proceedings of the Sixth Symposium on Ballistic Missile and Aerospace Technology*, Academic Press, New York, N. Y., vol. 1, 1961, pp. 219–238.

11 C. R. Steele, "Shells of Revolution With Edge Loads of Rapid Circumferential Variation," JOURNAL OF APPLIED MECHANICS, vol. 29, TRANS. ASME, vol. 84, Series E, 1962, pp. 701–707.

12 R. D. Schile, "Asymptotic Solution of Nonshallow Shells of Revolution Subjected to Nonsymmetric Loads," *Journal of the Aerospace Sciences*, vol. 29, 1962, pp. 1375–1379.

13 E. Reissner, "A New Derivation of the Equations for the Deformation of Elastic Shells," *American Journal of Mathematics*, vol. 63, 1941, pp. 177–184.

14 S. A. Ambartsumyan, "Theory of Anisotropic Shells" (in Russian), *Gosudarstvennoye Izdatel'stvo Fiziko-Matematicheskoi Literatury*, Moscow, USSR, 1961, p. 91.

15 P. M. Naghdi, "On the Theory of Thin Elastic Shells," *Quarterly of Applied Mathematics*, vol. 14, 1957, pp. 369–380.

16 P. F. Jordan, "Stresses and Deformations of the Thin-Walled Pressurized Torus," *Journal of the Aerospace Sciences*, vol. 29, 1962, pp. 213–225.

17 J. L. Sanders, Jr., and A. Liepins, "Toroidal Membrane Under Internal Pressure," *AIAA Journal*, vol. 1, 1963, pp. 2105–2110.

18 E. Reissner, "On Stresses and Deformations in Toroidal Shells of Circular Cross Section Which Are Acted Upon by Uniform Normal Pressure," *Quarterly of Applied Mathematics*, vol. 21, 1963, pp. 177–187.

19 R. A. Clark, "On the Theory of Thin Elastic Toroidal Shells," *Journal of Mathematics and Physics*, vol. 29, 1950, pp. 146–178.

20 A. L. Goldenveizer, *Theory of Elastic Thin Shells*, Pergamon Press, New York, N. Y., 1961, p. 480.

2.12.4 Listing of the PRSVSL Computer Code

```
M PRSVSL      74/74    OPT=1 TRACE                    FTN 4.6+498          07/11/8

      PROGRAM PRSVSL (INPUT,OUTPUT,TAPE5=INPUT,TAPE6=OUTPUT)
C
C     PROGRAM TO CALCULATE THE STRESSES IN THE HEAD AND THE WALLS OF A CYLINDRIC
C     PRESSURE VESSEL WITH A FLAT HEAD.  EQUATIONS FROM CASE 30 IN TABLE XIII
C     OF ROARK, 4TH ED.  PAGE 307.  USES ALSO CASES 1, 14, AND 15 FROM TABLE XI
C     AND CASES 1 AND 12 FROM TABLE X  PAGE 216.
C
C     PROGRAM ASSUMES THE SAME MATERIAL FOR BOTH THE HEAD AND CYLINDER WALLS.
C
C     INPUT READ ON ONE CARD ON AN  8F10.2  FORMAT.
C
C        P     INTERNAL PRESSURE, PSI
C        DIA   INSIDE DIAMETER OF CYLINDER, INCHES
C        T1    HEAD THICKNESS, INCHES
C        T2    CYLINDER WALL THICKNESS, INCHES
C        XF    MAX DISTANCE FROM HEAD AT WHICH STRESSES ARE TO BE EXAMINED, INCH
C        XINC  INCREMENT OF DISTANCES FROM HEAD END FOR STRESS EXAMINATION, INCH
C        E     ELASTIC MODULAS, PSI  (IF BLANK ASSUMES 29.0E6)
C        POI   POISSONS RATIO   (IF BLANK ASSUMES 0.3)
C
C
      REAL MO,LAM,LAMDA
      DD(EE,TT,UN)=EE*TT**3/(12.0-12.0*UN**2)
      LAMDA(UN,RR,TT)=SQRT(SQRT(3.0*(1.0-UN**2)/(RR*TT)**2))
   10 READ (5,501) P,DIA,T1,T2,XF,XINC,E,POI
      IF (EOF(5)) 20,30
   20 STOP
   30 IF (E.LE.0.0) E=29.0E6
      IF (POI.LE.0.0) POI=0.3
      WRITE (6,601) P,DIA,T1,T2,E,POI
      X=0.0
      N=XF/XINC+1
      R=(DIA+T2)/2.0
      D1=DD(E,T1,POI)
      D2=DD(E,T2,POI)
      LAM=LAMDA(POI,R,T2)
      ZA=P*R**3*LAM**2*D2/(4.0*D1*(1.0+POI))
      ZB=2.0*P*R**2*LAM**3*E*T1*D2/(E*T2*(1.0-0.5*POI)*(E*T1+2.0*R*D2*
     1   LAM**3*(1.0-POI)))
      ZC=2.0*LAM+2.0*R*LAM**2*D2/(D1*(1.0+POI))
      ZD=LAM*E*T1/(E*T1+2.0*D2*LAM**3*R*(1.0-POI))
      PRINT *,LAM,ZA,ZB,ZC,ZD
      MO=(ZA+ZB)/(ZC-ZD)
      VO=MO*ZC-ZA
      SC1=P*R/T2
      SCM1=SC1/2.0
      SH1=0.375*P*(R-0.5*T2)**2*(3.+POI)/T1**2
      SH2=-6.0*MO/T1**2
      SH3=VO/T1
      SHT=SH1+SH2+SH3

C     SC1=CYLINDRICAL MEMBRANE HOOP STRESS  EQ1  TABLE XIII
C     SCM1=CYLINDRICAL MERIDIONAL MEMBRANE STRESS  EQ 1  TABLE XIII
```

```
      SH1,SH2,SH3=HEAD STRESSES   EQS 1, 12 TABLE X  AND  EQ 36  TABLE XIII
      SHT=TOTAL HEAD STRESS.
C
      WRITE (6,602) MO,VO
      WRITE (6,603) SH1,SH2,SH3,SHT
      DO 40 I=1,N
      XLAM=X*LAM
      SC2=-2.0*VO*(LAM*R*EXP(-XLAM)*COS(XLAM))/T2
      SC3=2.0*LAM**2*R*MO*EXP(-XLAM)*(COS(XLAM)-SIN(XLAM))/T2
      SCM4=6.0*VO*EXP(-XLAM)*SIN(XLAM)/(LAM*T2**2)
      SCM5=-6.0*MO*EXP(-XLAM)*(COS(XLAM)+SIN(XLAM))/T2**2
      SC4=SCM4*POI
      SC5=SCM5*POI
      SCTCVX=SC1+SC2+SC3+SC4+SC5
      SCTCCV=SC1+SC2+SC3-SC4-SC5
      SCMTCX=SCM1+SCM4+SCM5
      SCMTCV=SCM1-SCM4-SCM5
C
C      SC2,SC3=CYLINDRICAL MEMBRANE HOOP STRESSES  EQS 14 AND 15   TABLE XII
C      SC4,SC5=CYLINDRICAL BENDING HOOP STRESSES  EQS 14 AND 15   TABLE XIII
C      SCM4,SCM5=CYLINDRICAL MERIDIONAL BENDING STRESSES  EQS 14 AND 15 TAB
C      SCTCVX=TOTAL HOOP STRESS ON THE CONVEX SURFACE
C      SCTCCV=TOTAL HOOP STRESS ON THE CONCAVE SURFACE
C      SCMTCX=TOTAL MERIDIONAL STRESS ON THE CONVEX SURFACE
C      SCMTCV=TOTAL MERIDIONAL STRESS ON THE CONCAVE SURFACE
C
      WRITE (6,604) X,SC1,SC2,SC3,SC4,SC5,SCTCVX,SCM1,SCM4,SCM5,SCMTCX
      WRITE (6,605) SCTCCV,SCMTCV
   40 X=X+XINC
      GO TO 10
  601 FORMAT (8F10.2)
  602 FORMAT (1H1,30X,72HSTRESSES IN HEAD AND CYLINDERICAL WALLS OF A FL
     1AT HEADED PRESSURE VESSEL//32X,8HPRESSURE,9X,F9.0,4H PSI,13X,
     2 15HINSIDE DIAMETER,4X,F8.3,3H IN/32X,14HHEAD THICKNESS,5X,F7.3,
     3 3H IN,11X,16HCYLINDER WALL TK,4X,F7.3,3H IN/32X,15HELASTIC MODULU
     4S,2X,1PE9.3,4H PSI,6P,10X,14HPOISSONS RATIO,5X,F8.3//)
  603 FORMAT (32X,10HEND MOMENT,4X,1PE10.3,6H IN-LB,10X,9HEND SHEAR,6X,
     1  E10.3,6H LB/IN///)
  603 FORMAT (61X,13HHEAD STRESSES/61X,13H=============//50X,17HFROM UNI
     1FORM LOAD,3X,F10.0,4H PSI/50X,16HFROM EDGE MOMENT,4X,F10.0,4H PSI/
     2 50X,17HFROM RADIAL SHEAR,3X,F10.0,4H PSI/50X,5HTOTAL,15X,F10.0,
     3 4H PSI///59X,21HCYLINDRICAL STRESSES/59X,21H=====================/
     4 42X,13HHOOP STRESSES,32X,19HMERIDIONAL STRESSES/2X,8HDISTANCE,4X,
     5 8HMEMBRANE,4X,8HMEMBRANE4X,7HBENDING,5X,7HBENDING,
     6 5X,5HTOTAL,4X,12HFROM UNIFORM,2X,9HFROM EDGE,2X,9HFROM EDGE,5X,
     7 5HTOTAL/2X,8HFROM END,2X,12HFROM UNIFORM,2X,9HFROM EDGE,3X,9HFROM
     8 EDGE,3X,9HFROM EDGE,3X,9HFROM EDGE,4X,6HCONVEX,5X,8HPRESSURE,5X,
     9 5HSHEAR,7X,6HMOMENT,6X,6HCONVEX/5X,2HIN,7X,8HPRESSURE,5X,
     1 5HSHEAR,7X,6HMOMENT,6X,5HSHEAR,7X,6HMOMENT, 5X,7HCONCAVE,4X,
     2 7HCONCAVE//)
  604 FORMAT (2X,F8.3,1X,10(F10.0,2X))
  605 FORMAT (71X,F10.0,38X,F10.0/)
      END
```

2.12.5 BMI-1 Basket Drop Tests

In order to demonstrate compliance of the BMI-1 basket with the 30-ft free drop criteria of 10CFR71 a full scale basket with removable bottom was tested in a simulated cask for falls in both the critical angle and horizontal orientations.

(a) Test Specimens - The test basket was constructed according to the design drawings BCL-000-500, Rev. A and BCL-000-501 with the two following exceptions.

(1) The two retractable lifting lugs were not built into the basket since they do not provide any structural support to the basket for the impact conditions. The lifting lugs are designed for lifting loads only and do not contribute to the structure of the basket in any way. The springs are used solely to extend the lugs when the lid has been removed. When the lid is in place, the lugs are pushed back into the retracted position. In the inverted drop position, the lugs do not react any of the impact load except for their individual inertial loads.

(2) For purposes of rapid availability and economy, the boral in the cruciform was replaced with Type 6061-T6 aluminum sheet. This replacement was considered acceptable since the two materials have essentially the same low ductility as evidenced by their similarly low elongation. This latter property is considered highly important since failure of the stainless steel cladding could expose the boral. If the boral were to fracture as a result of the impact and be lost from the cruciform, an unacceptable criticality situation could exist. As can be seen from the photographs of the test basket after the drop test (page 2.135, photographs E6

VIEWS OF TEST BASKET CRUCIFORM

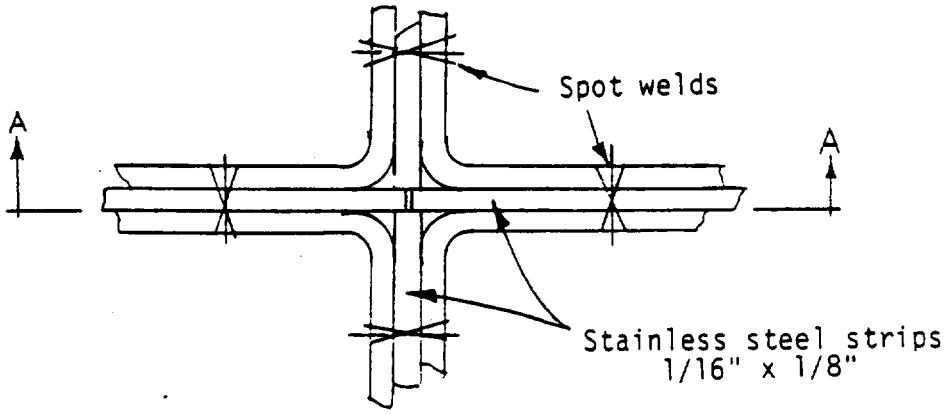

Plan View

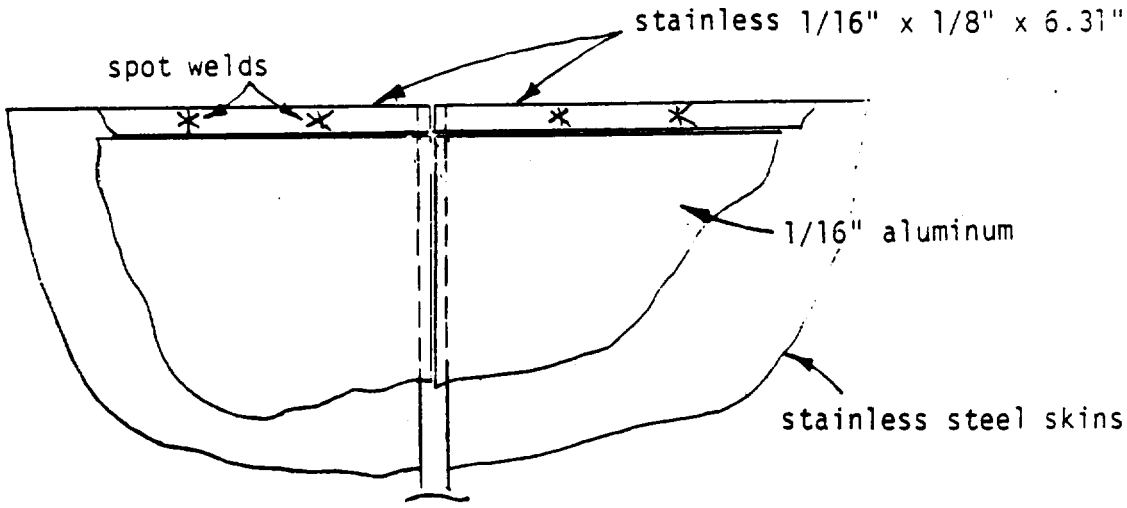

Section A-A cut away view

and E11), the cruciform with the Type 6061-T6 aluminum sheet replacing the boral, while deformed, is still in tact as far as maintaining an acceptable criticality situation. The stainless steel cover sheets have torn along their top edges, but the aluminum sheets are intact and unaffected by the impact. The basic integrity of the four cells has been maintained.

The boral in the actual baskets and aluminum in the test basket are, in effect, filler material for the sandwich. There is no mechanical bond or attachment between the boral (or aluminum) and the stainless steel other than the restraint of the spot welded steel enclosure. As a result of the drop test, the steel sheet covering the aluminum shown on pg. 2.135 tore at the upper end of the basket, but the aluminum sheets remained intact and continued to serve as separators for the four quadrants.

Full quality control procedures as required by Appendix E of 10CFR71 were followed for the fabrication of the basket and removable bottom.

The cask used in the drop tests only simulated the BMI-1 cask since a full size cask model is too heavy to test at the BCL drop test facility. Therefore, the simulated cask was approximately half the length of the BMI-1 and with 4-inch thick lead shielding in the sides and bottom instead of 8-inch as in the side and 7.5-inch as in the bottom of the BMI-1 cask, see sketch on page 2.126. Also, the top of the simulated cask was made of two 1/2-inch thick steel plates laminated together. Four eyes on the side were used to lift and position the simulated cask at the proper orientation. Use of the simulated cask is considered conservative because this lighter cask will be stopped more rapidly upon impact and will thus experience <u>higher impact G-loads</u> than will the heavier BMI-1 cask.

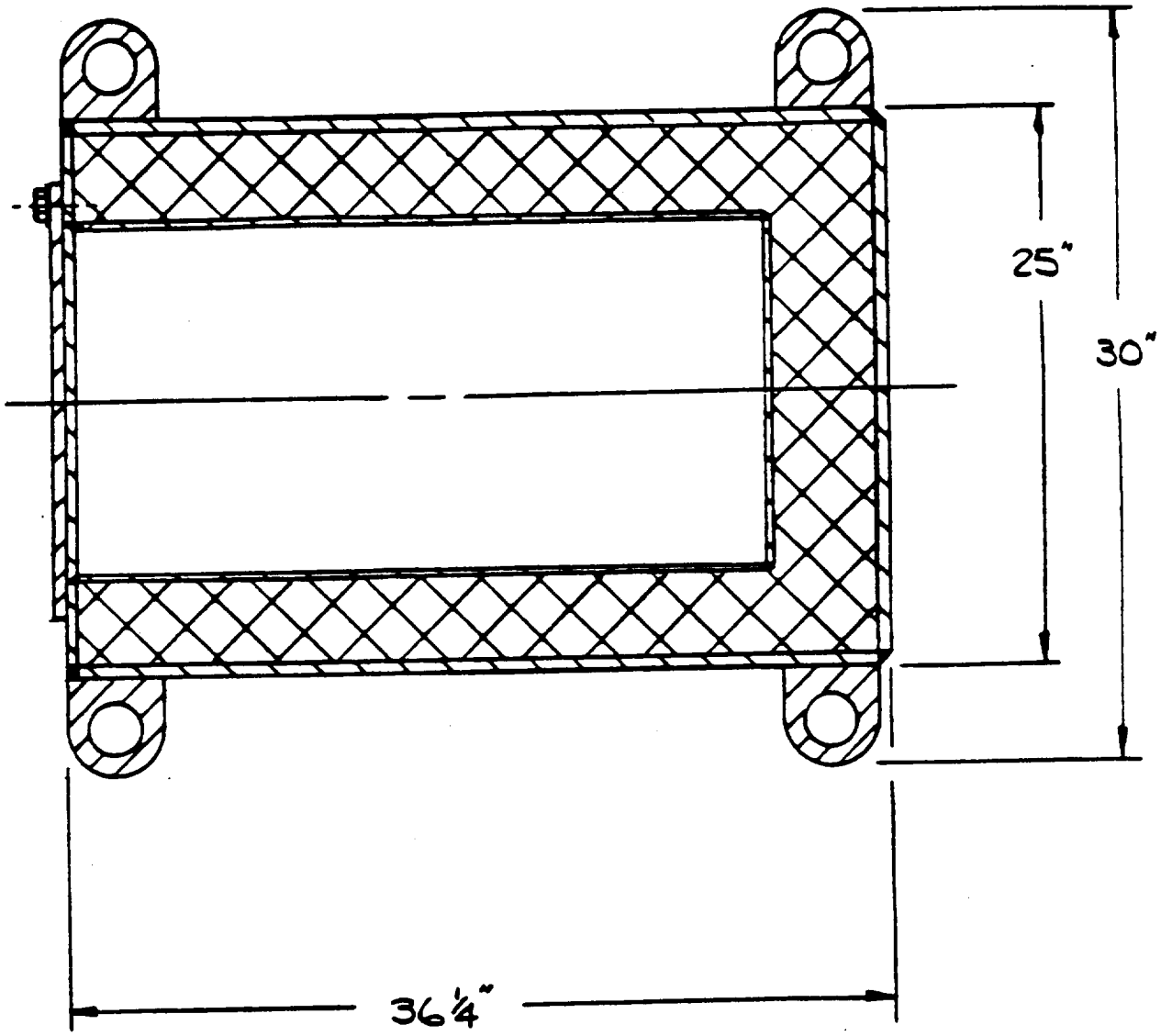
25"
30"
36¼"

Steel plates with wooden ends were used to simulate the loading of the fuel elements in the basket, see sketch on page 2.128. For the corner impact test the "elements" were placed upright in the basket cells as shown with the plane of the steel plate perpendicular to the grid of the removable bottom. In this way the appropriate impact load from an actual full element was produced. The wooden ends kept the plate centered and tended to distribute the load.

In an actual cask shipment the lower basket rests on the cask bottom, and the upper basket is supported on the four corner braces of the lower basket which extend 1.0-inch above the lower basket. In order to reproduce this type of four-point support, four 1/2-inch square bars were tack-welded to the bottom of the removable bottom at the points at which the corner braces would make contact, see sketch on page 2.128. In this way the basket grid was free to deform under the impact load of the simulated fuel elements.

When the cask undergoes end or corner angle impact, the impact load of the upper basket acts on the lower basket. This condition produces severe loads in several key locations including the corner braces, their attachment to the upper cage, the structural angles of the basket and the cruciform. In order to represent this loading, a lead filled steel can was made which would have the same weight as a loaded upper basket. Due to shrinkage during lead pour, the weight of the lead/steel can was 169 lb rather than the 178 lb calculated as the weight of a fully loaded basket. The error is only 5 percent and this was considered sufficiently close to permit use of the weight to represent the upper basket.

FIGURE WITHHELD UNDER 10 CFR 2.390

:- ~rH K.,

STh E BAR7

REMOVABLE 50TT0M

U-9ED *FOR* -r E.S

REV. D, 11/23/82

The weight of the test components was as follows:

Simulated Cask	4,600 lb
Basket and Bottom	72 lb
12 fuel elements @ 8 lb	96 lb
Lead/Steel Weight (upper basket)	169 lb
Total Weight	4,937 lb

(b) Test Procedures - Three tests were performed, a critical angle corner impact, a horizontal impact, and a puncture test. These were performed in that sequence. For the critical angle test, the basket was inserted into the simulated cask cavity with the walls of the fuel element cells oriented parallel and perpendicular to the "tilt plane" of the cask. The grid of the basket bottom was parallel to the "tilt plane" and the "fuel elements" were placed in the cells so the plane of the steel plates was perpendicular to the basket grid. The lead/steel weight to simulate an upper basket was placed on the top of the test basket. Impact-o-graph* accelerometers with trip values of 100, 150, 200, 250, and 300 g's were attached to the cruciform near the bottom of the basket. They were located in a cluster in an inner cell on the underside of the "spoke" of the cruciform which was perpendicular to the tilt angle. The Impact-o-graph accelerometers are "go-no go" mechanical accelerometers which indicate by release of small balls and springs when a preset G-load is experienced. They are 3-directional, i.e., they will trigger if the preset load level occurs along any of the three axes or at any angle between the axes. The reported accuracy is ±15 percent.

*Trade Name.

A similar cluster of five acceleromters was placed on the top of the cask. They were located on the cask head adjacent to the cover on the side diagonally opposite from the impact corner.

For the horizontal drop test and the puncture test the walls of the basket cells were positioned parallel and perpendicular to the impact direction. The wooden ends of the steel "fuel elements" were not used. Rather the steel plates were laid directly on the bottom side of each basket cell. A cluster of five accelerometers was placed on the underside of one of the center cells. They were attached near the bottom of the basket on a horizontal spoke of the cruciform. A similar cluster of accelerometers was placed on the top of the cask opposite the impact side. The impact side of the simulated cask was 180 degrees from the impact edge for the critical angle impact.

(c) Results of Critical Angle Impact. After impact the cask rebounded toward an upright position and continued rotating so that it landed on the side opposite the impact corner. The impact footprint on the bottom corner extended 5.0 inches, radically inward from the original edge. However, the side of the outer shell was partially "rolled under" and also formed part of the footprint. The side was also bulged out producing the common "elephants foot" appearance evident in end-on axial impacts of lead casks. All of the accelerometers on the outside of the cask had triggered indicating an impact load on the cask in excess of 300 G.

The cask cover was easily removed. There was no visible damage to the top of cask. The basket was readily removed. The accelerometers had all triggered indicating that the impact load on the basket had exceeded 300 G. The four corner braces supporting the lead/steel box representing an upper basket were

not visibly deformed. The welds of the braces to the upper cage were all intact. Two of the light gage cell walls suffered broken welds at the top end and were bent, see photographs on p. 2.132. One cell wall was also bowed slightly at the top end. The cruciform was intact and was not visibly deformed. The grid of the removable bottom was deflected downward a maximum of 7/32-inch on the center grid bars and lesser amount on the others.

The accelerometers indicated that an impact load in excess of 300 G was experienced by the basket. In order to estimate the possible value of the impact load, the following analysis was performed: elsewhere in this SARP the predicted critical angle corner impact load was calculated as

$$G = 2\ H/x$$

where

H = drop height = 360 inches

x = maximum deformation

The deformation x is shown on the following sketch, p. 2.133. In that sketch, 5.0 inches is the radial dimension of the footprint. Then

$$x = 5 \sin 23.5$$
$$= 1.99 \text{ inch}$$

and

$$G = (2)\ (360)/1.99 = 361 \text{ g}$$

Since this represents an equivalent force vector, the axial component can be determined as

$$G_{axial} = (361)\ (\cos 23.5)$$
$$= 331 \text{ g.}$$

C-10

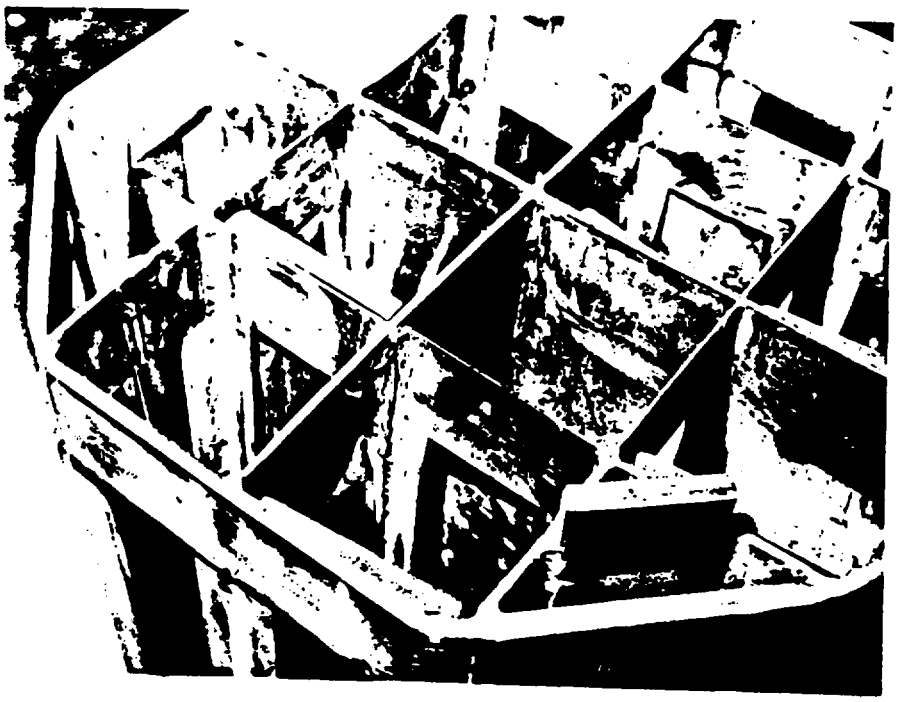

C-11

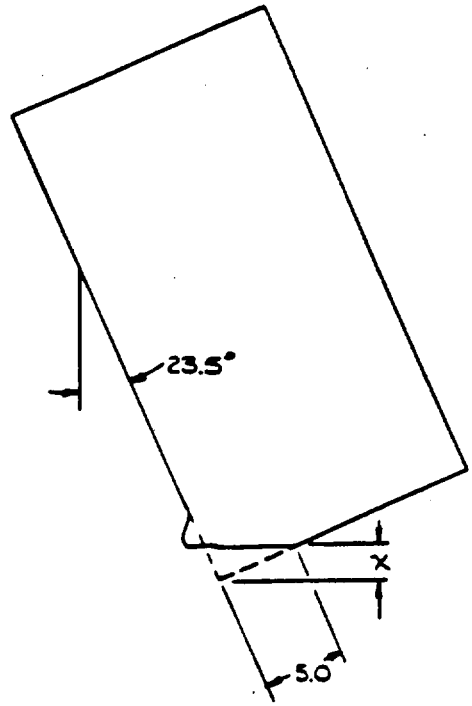

(d) Results of Horizontal Impact Test. Upon impact, the eight 3/8-inch bolts holding the light cover on fractured and the lead/steel weight on top of the basket fell out. Examination of the fractured surface of the bolts leads to the conclusion that the bolts probably sheared due to deformation of the head of the simulated cask. This is not indicative of the expected performance of the BMI-1 cask since the head, cover, and bolting design on the simulated cask is significantly different and of less rigidity than the BMI-1 cask design.

All accelerometers on the outside of the cask had triggered indicating that an impact load in excess of 300 g had occurred.

Inspection of the top of the basket before removal revealed that most of the welds on the light gage components forming the cells within each quadrant were broken. The cruciform, however, was intact although bent. This observation was confirmed after the basket was removed. The head of the cask was oval and

moderate force was required to slide the basket out. The basket was slightly oval at the top end probably from the action of the cask walls.

All accelerometers on the cruciform in the basket were triggered indicating an impact load in excess of 300 g was experienced. At the top end of the basket, the horizontal spokes of the cruciform were bent down about 1/2 to 3/4 inch at the midspan of each spoke, see photograph on p. 2.135. All welds of the cruciform to the basket outer walls were intact. Similarly the juncture of the four cruciform spokes was intact the full axial length of the basket. However, at the ends of the cruciform adjacent to the juncture of the four spokes, the end clad weld joints which sealed the simulated boral in the cruciform was torn, see photographs on p. 2.135. The edge of the simulated boral was visible for about 1-inch of the radial direction on the vertical spokes, and for less than 1/2inch on the two horizontal spokes. The simulated boral was intact and no chips or cracks were visible. Moreover, the edges of the simulated boral were straight. The nature of the "tear" in the edge indicates that it was caused by a "pulling apart" of the cladding on the vertical spokes by the horizontal spokes as they deformed. This observation is confirmed by the relatively unaffected straight and intact condition of the simulated boral.

The basket cells were deformed, especially those below the horizontal spokes of the cruciform. Many of the welds of the light cell walls were broken. The walls of two of the 1/8 x 3/4 x 3/4 angles forming the basket corners were broken at the bottom end.

The following conclusions can be made regarding the results.

(1) the neutron poison cruciform structure maintained isolation of the four quadrants of the basket. Thus the subcritical conditions of the contents are maintained.

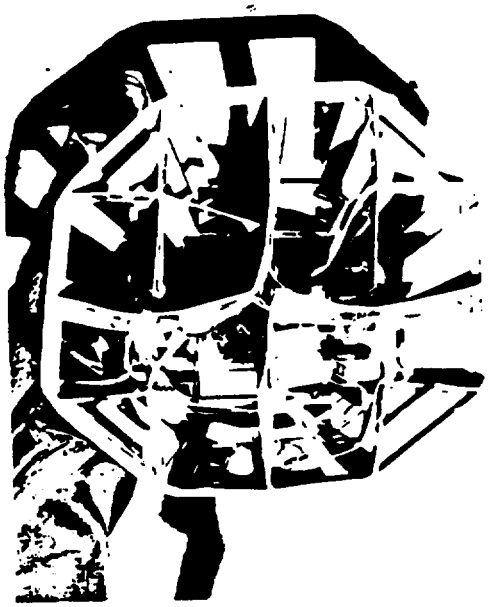

E 6

E 11

(2) Deformation of the fuel elements due to basket deformation is not significant.

(3) The basket retained sufficient structural integrity to permit post-accident handling without special procedures.

(e) Evaluation of Other Rotational Orientations for Horizontal Impact. As noted above, the 30-foot droptest was performed with the walls of the basket cells oriented parallel and perpendicular to the direction of impact (Surface A impact in the sketch below).

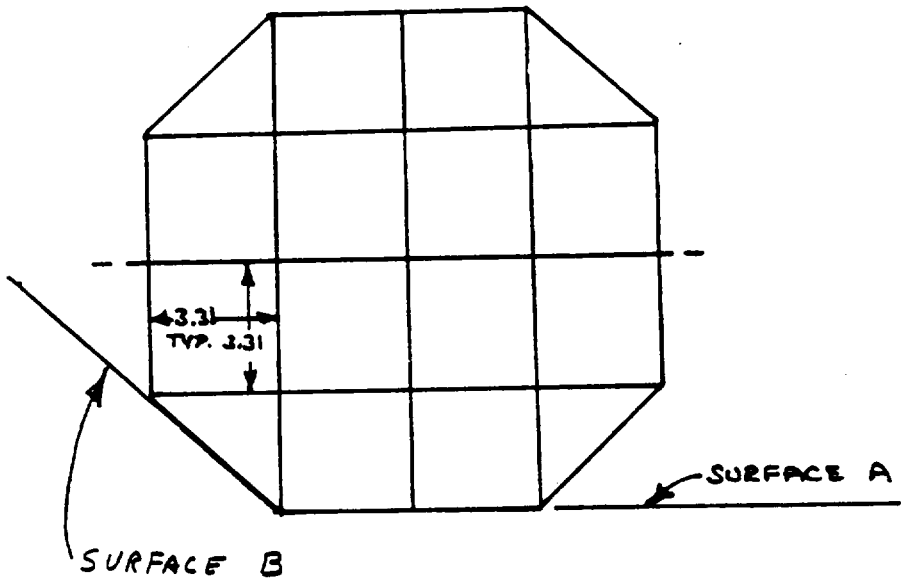

This orientation produces the most severe loading condition for impact in the horizontal position. This is shown by comparing the magnitude of the loads on the basket members for this and other orientations, for example a Surface B impact in the preceeding sketch.

The structure of the basket cells is shown in Drawing BCL-000-500, Rev. A. The structure of the cruciform member is shown in Drawing 0048, Rev. A. The light gage cell walls (Item 12 in Drawing BCL-000-500, Rev. A) provide negligible support to the strength of the cruciform since they have large rectangular holes in them to facilitate heat transfer between cell cavities and they are attached to the cruciform with skip welds. Thus their contribution is neglected. The construction of the cruciform is such that the cladding panels, Item 6 in Drawing 0048, Rev. A, are firmly bonded to each other at the top, bottom, and outside edges where they are welded to common edge cladding, Items 2 and 3. There is also a less secure attachment between the panels at the spot welds between the panels and internal spacers, Item 5. These spot welds are light welds made to facilitate fabrication. Their contribution to bonding the cladding panels on opposite sides of the cruciform to each other so they act in unison rather than separately is unknown. However, as will be shown, this knowledge is not necessary for comparison of the loading patterns to establish the most severe one.

The loading on the cruciform for both the Surface A and Surface B impact orientations is shown in the sketch on page 2.138. The model assumes that the impact loads produced by each element are equal and have a value of Wg.

A free body diagram of the four panels is shown in the sketch on page 2.139. The panels are welded to a common edge clad/spacer at the ends of the cruciform arms (location of reaction forces R_1, R_2, R_3, and R_4). However, since the panels are also welded to the basket sides, the reaction forces at the outside edges of the panel can be assumed to be indepedent of

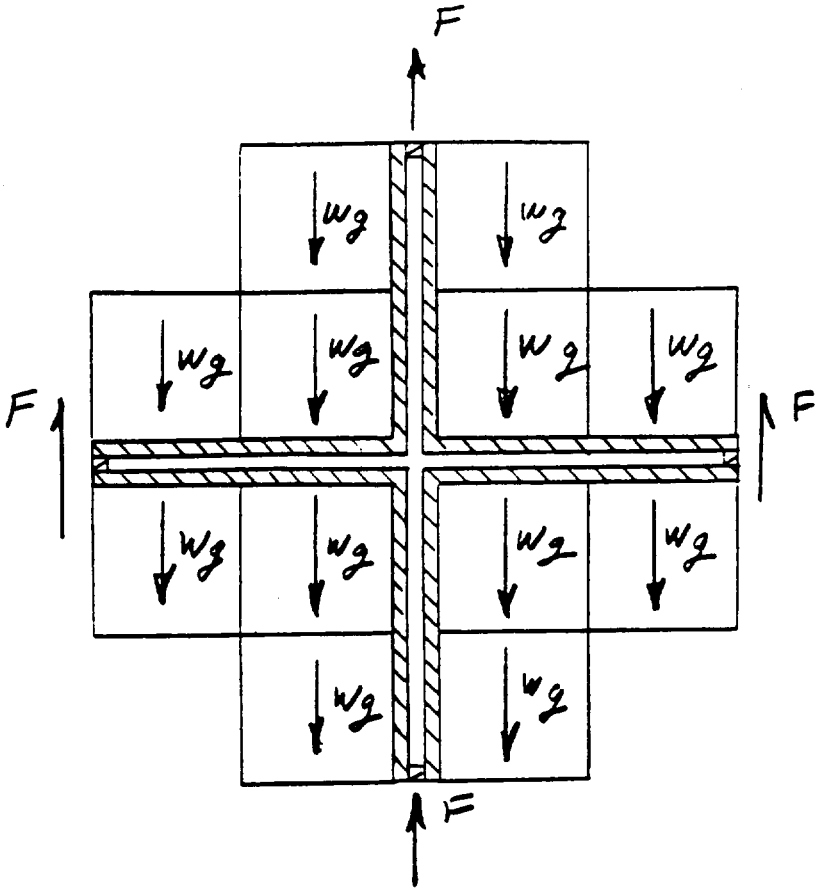

LOADING ON CRUCIFORM FOR SURFACE A IMPACT

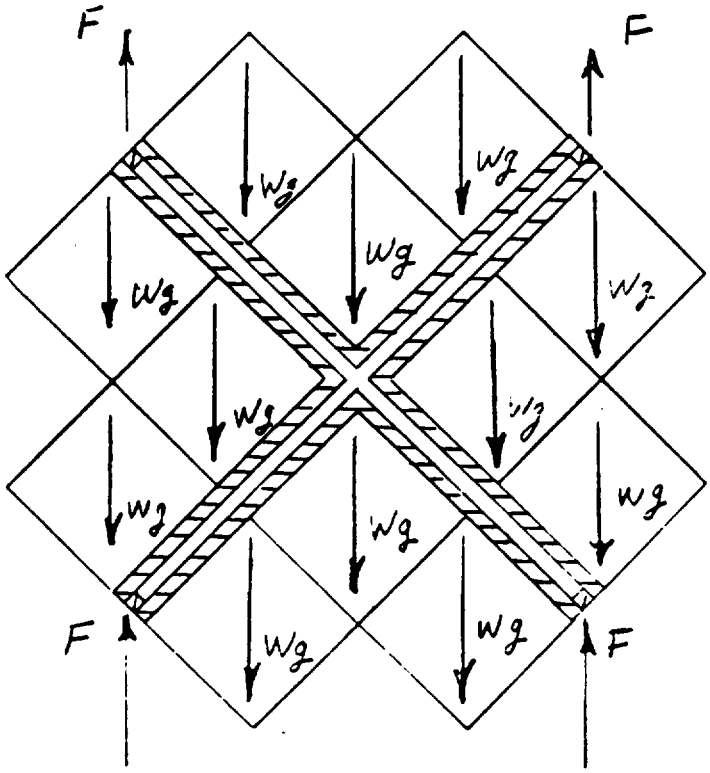

LOADING ON CRUCIFORM FOR SURFACE B IMPACT

REV. E, 12/28/83

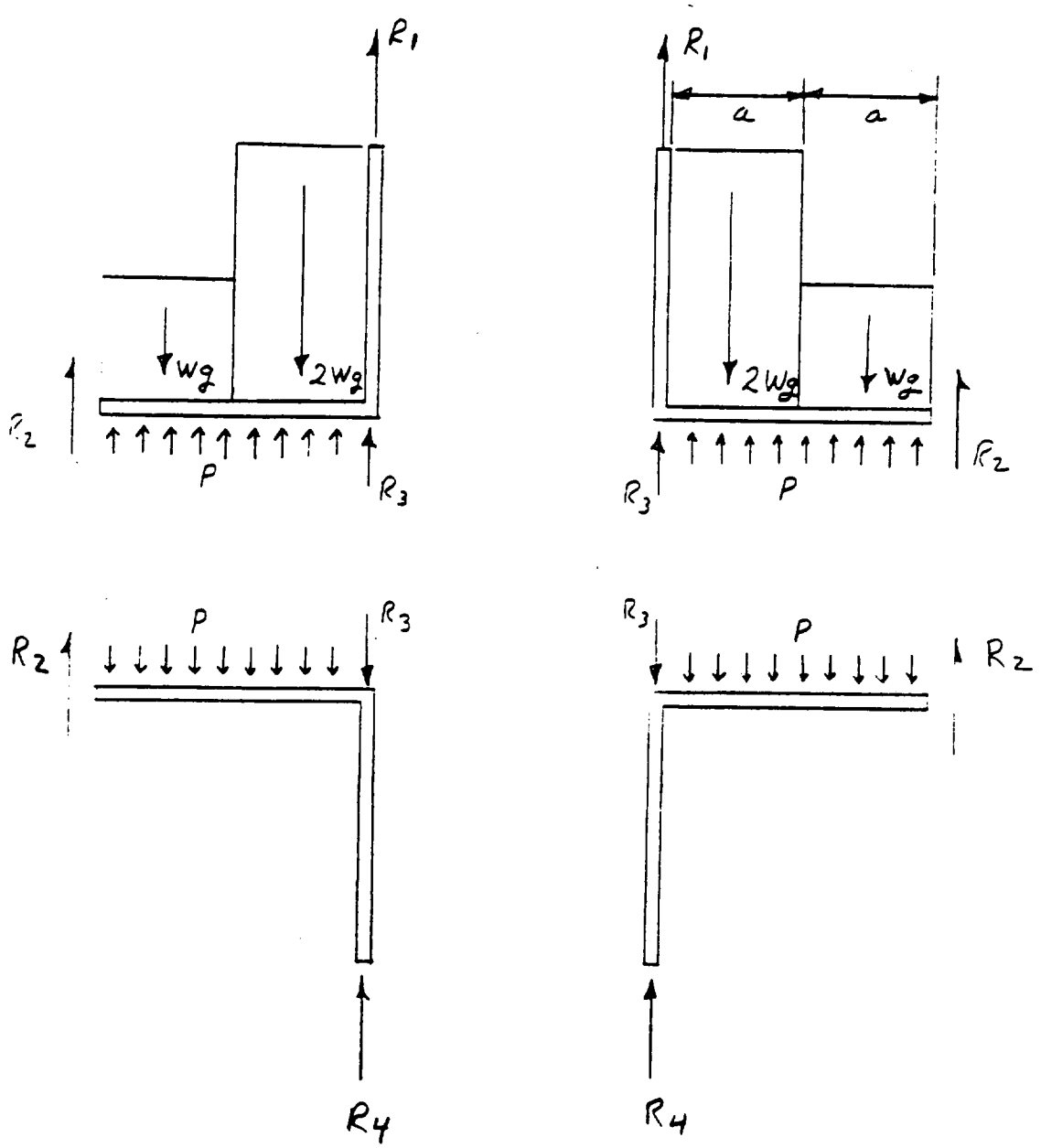

Note: P is the force per unit length.

FREE BODY DIAGRAM FOR SURFACE A IMPACT

REV. E, 12/28/83

each other. The impact loading on the panels from each fuel element is Wg. The effect of the light cell dividers within each quadrant is neglected and the elements are assumed to be in intimate contact. The pressure force, P, between the panels forming the horizontal arm is the area pressure between the panels (through the boral). The reaction force R_3 is the direct reaction between the vertical arms of the adjacent panels. The width and breadth of the fuel elements are "a". Consider an upper quadrant in the sketch. Summing forces in the vertical direction yields

$$R_1 + R_3 + R_2 + P(2a) = 3\ Wg\ . \qquad \text{(Eq. 1)}$$

Similarly, for the lower quadrant,

$$R_3 + P(2a) = R_4 + R_2\ . \qquad \text{(Eq. 2)}$$

Substitution of Eq. 2 into Eq. 1 yields

$$R_1 + R_4 + 2R_2 = 3\ Wg\ . \qquad \text{(Eq. 3)}$$

Equations 1 and 3 indicate the obvious--that for the test orientation (Surface A impact) the sum of the reaction forces acting on the cruciform panels total to the impact force of the three fuel elements resting on it. This value can now be compared with similar equations for the Surface B impact orientation.

A free body diagram for a Surface B impact is shown in the following sketch, Page 2.141. For the top quadrant, summing moments about Point A yields

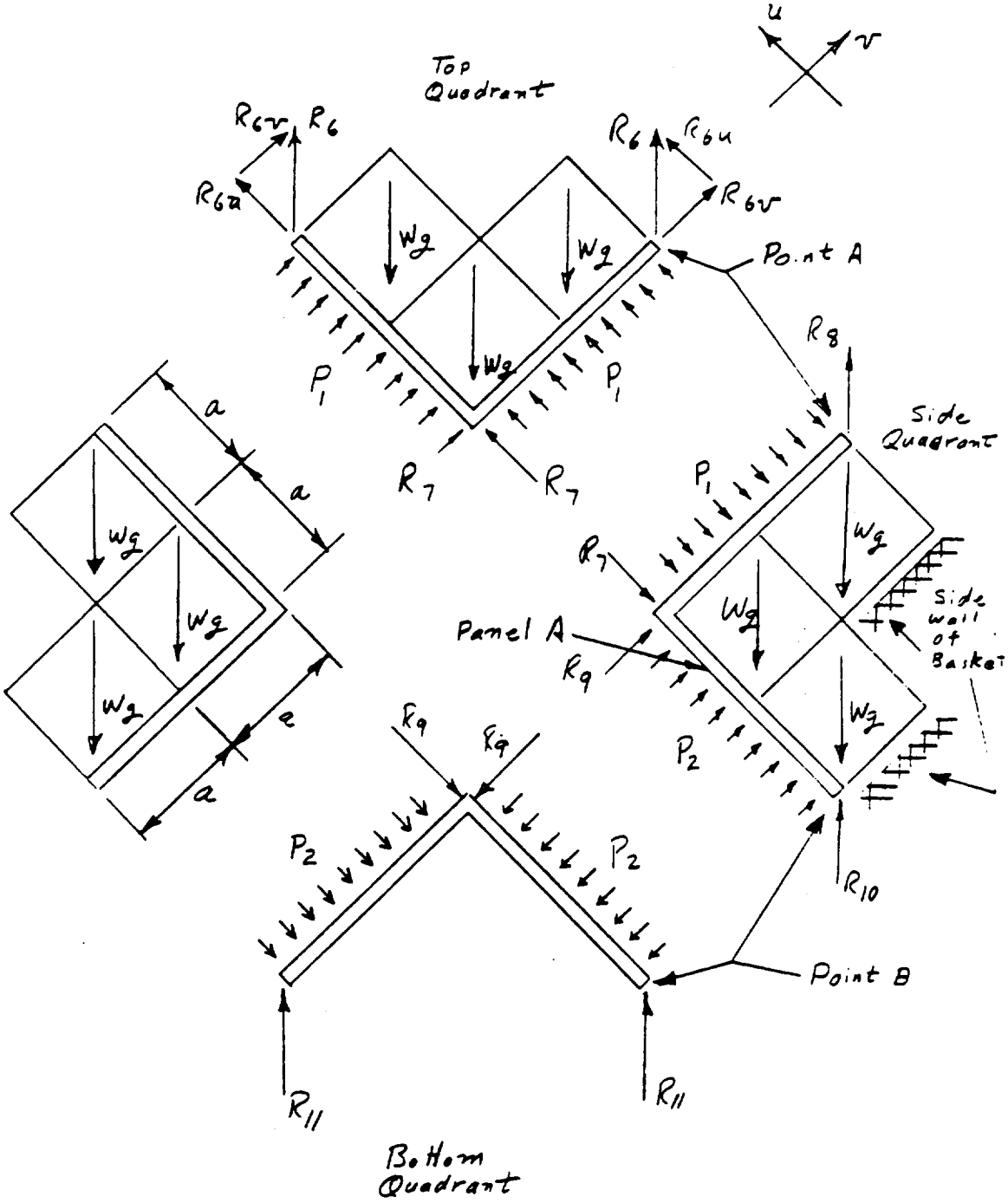

Note: P_1 and P_2 are forces per unit length.

FREE BODY DIAGRAM FOR SURFACE B IMPACT

$$R_{6u}(2a) + R_{6v}(2a) + 2\,[P_1(2a)a] + R_7(2a) =$$

$$0.707\ (2Wg)\ (3a/2) + 0.707\ (Wg)(a/2) + 0.707\ (2Wg)(a/2) +$$

$$0.707\ (Wg)\ (3a/2)$$

$$R6_u + R6_v + 2P_1a + R_7 = 2.121\ Wg \quad .$$

However, $R_{6u} = R_{6v} = 0.707\ R_6$.

Then

$$1.414\ R_6 + 2P_1a + R_7 = 2.121\ Wg \qquad \text{(Eq. 4)}$$

$$0.707\ R_8 + R_9 + P_2(2a) +$$

$$0.707(R_{10}) = 3(0.707\ Wg) \quad . \qquad \text{(Eq. 5)}$$

Summing forces in the "u" direction yields

$$R_7 + P_1(2a) = 0.707\ R_8 + 0.707\ R_{10} \qquad \text{(Eq. 6)}$$

(The impact forces, Wg, do not act on the cruciform along this axis but bear on the side of the basket.) Summing moments about Point A yields

$$P_1(2a)(a) + R_7(2a) + P_2(2a)(a) =$$

$$2\ (.707\ Wg)(a/2) + (.707\ Wg)(3a/2)$$

$$P_1a + P_2a + R_7 = 0.884\ Wg \quad . \qquad \text{(Eq.}$$

(As above, the Wg force components along the "u" axis do not act on the cruciform.) Summing moments about Point B yields

$$R_9\ (2a) + P_2(2a)(a) + P_1(2a)(a) =$$

$$2\ (.707\ Wg)(3a/2) + 0.707\ Wg(a/2)$$

$$R_9 + P_2a + P_1a = 1.237\ Wg \quad . \qquad \text{(Eq. 8)}$$

Equations 5 through 8 are <u>not</u> mutually independent but are presented to show the interaction of the several reaction forces and their relationship to the impact forces, Wg. The observation which is made from examination of the four equations is that the sum of the reaction forces is less than the sum for a Surface A impact, Eq. 1.

Considering the lower quadrant and summing forces in the vertical direction yields

$$2(0.707)R_9 + 2(0.707)(P_2)(2a) = 2R_{11}$$

$$R_9 + 2P_2a = 1.414\ R_{11} \quad . \qquad \text{(Eq. 9)}$$

This can be combined with Eq. 6 to give

$$R_9 + 1.414\ R_{11} + 2P_1a = 2.474\ Wg \qquad \text{(Eq. 10)}$$

All of the above equations indicate that the <u>sum</u> of the reaction forces acting on the cladding panels is less severe for the Surface B impact orientation than for the Surface A impact orientation which was used in the test. One feature, however, is not considered above, that of the in-plane compression loading for certain panels.

Referring to the sketch for the Surface B impact, Page 2.141, attention is called to the side and bottom quadrant free body diagrams--specifically the panel arms in the plane of the "u" axis. These arms are acted on by R_7 and $(0.707)R_{10}$, and by

R_9 and $(0.707)R_{11}$. These two pair of forces are opposed and place the respective panels in compression. Moreover, the panel is subjected to a pressure from P_2 and the "v" axis vector of the impact forces, Wg. The exact magnitude of the forces and their effect can not be determined without extensive computer analysis or testing. The magnitude and effect can be inferred, however, by examination of the photographs on Page 2.135 and the free body diagram for Surface A impact, Page 2.139. In the free body diagram it is noted that the forces R_3 and R_4 act mutually opposite in the plane of the panel. From the photographs it is noted, however, that although some minor buckling of the panel occurred it was not extreme. The nature of the bowing which the horizontal arm of the cruciform experienced indicates that the force R_3 reached the value necessary to initiate buckling of the lower vertical arm. However, as motion occurred, the force R_1, rapidly increased relieving the buckling force R_3. Meanwhile, the action of the fuel element impact load was to produce significant bowing in the panel with most of the reaction being produced by forces R_1 and R_2. A similar occurrence would be expected for impact in the Surface B impact orientation. Consider the cladding panel mark "Panel A" in the free body diagram, Page 2.141. As the impact event progresses, the force R_7 would increase and might initiate buckling of the lower diagonal arm of the cruciform. However, the R_6 forces in the upper quadrant would rapidly increase, force R_7 would drop, and buckling as such would halt (similar to panel response for the test orientation). The side force on Panel A would tend to continue the bowing of the panel due to the v-axis vector of the impact force Wg which is slightly countered by pressure, P_2. The loading pattern is analogous but less severe to that shown for the upper quadrant of the free body diagram on page 2.139 for a Surface A impact (v vector of R_8 analogous to R_1, R_9 analogous to R_3, etc). Thus, the panel would be expected to bow <u>no more</u> than the amount shown

in the photographs on p. 2.135 and no failure other than the minor separation of the edge welds such as experienced by the test basket would be expected.

The above evaluation did not require knowledge about the structural integrity of the spot welds at the center spacers of the cruciform arms. It is assumed that their influence on panel response and performance, whether major or minor, would be the same for either a Surface A or Surface B impact orientation.

The above evaluation also did not consider the nature of the reaction forces, i.e., tensile, shear, etc. For the test orientation, Surface A impact, the force R_1 is a tensile force while R_2 is a combination shear and bending. The reaction forces for the Surface B impact are similar, i.e., tension, shear and bending. Thus, similar performance of the weld joints between the panels and the side of the bracket would be expected.

The above evaluation indicates that the <u>sum</u> of all the reaction forces acting on any one panel for a Surface B impact orientation is less than for a Surface A orientation, the orientation which was tested. Although the values of the individual reactor forces could not be evaluated, the analysis indicated that none are higher for the Surface B orientation than for the Surface A orientation. For example compare Eq. 1 and Eq. 4.

Eq. 1. (Surface A) $R_1 + R_2 + R_3 + 2Pa = 3\ Wg$

Eq. 4. (Surface B) $1.414\ R_6 + R_7 + 2P_1a = 2.121\ Wg$

Multiplying Eq. 4 by 1.414 yields

Eq. 4a. $2R_6 + 1.414\ R_7 + 2.828\ P_1a = 3\ Wg$

Then if it is assumed that $2R_6$ is analogous to $R_1 + R_2$, R_3 analogous to R_7 and Pa analogous to P_1a, R_6 is less than R_1 since there is greater support from the other reaction forces R_7 and P_1a. Even if R_7 and P_1a were nil, R_6 would be no greater

than R_1 or R_2. Consider the free body diagram, Page 2.139. If $R_3 = 0$ and $P = 0$, then $R_1 > R_2$; but since $R_1 + R_2$ equal $2R_6$, then $R_6 < R_1$. Similar logic shows that other reaction forces are less than experienced by the test basket during the fall in the Surface A impact orientation. Thus, it is shown that the Surface A impact orientation is the most severe. Any orientation for a rotational angle between Surface A and Surface B impact orientation would result in reaction forces between those for the A and B orientations.

(f) Results of 40-inch Drop Puncture Test

The test basket was subjected to a 40-inch puncture test on the side of the package following the 30 foot side drop test. Results of this test can be seen in the photographs on page 2.147. As can be seen from the photographs, there were some slight additional deformation of the light gage cell walls. However, the cruciform boral sheets dividing the quadrants display rather small amounts of increased deformation and remain essentially intact. The net effect of the puncture test was to clamp the "cask" shell more tightly around the basket making it virtually impossible to remove the basket. However, it was still possible to remove the fuel element without difficulty.

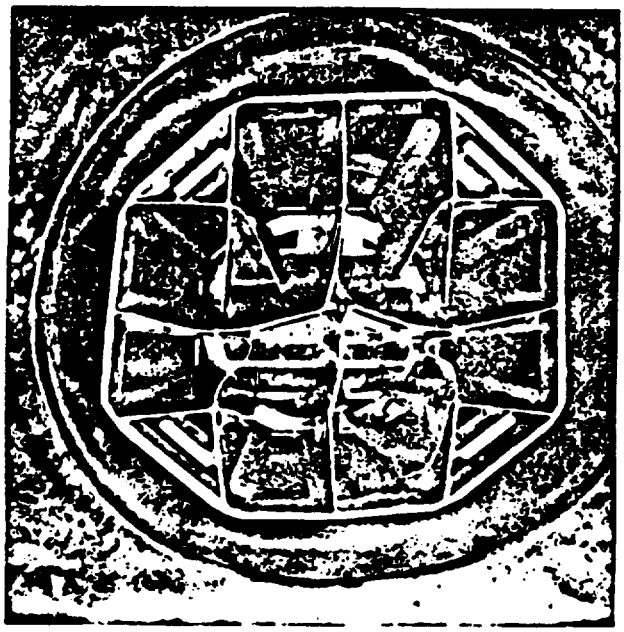

PUNC-10

(g) <u>Texas A&M MTR Fuel--Drop Analysis</u>. The Texas A&M fuel, as shown as BCL Drawing No. 000-236 is covered by the poison plates except for approximately 1/8 in. at the bottom end. The poison plate is 24-1/2 in. long (Ref. BCL Dwg. No. 0048), the active fuel length is 24.62 in. The design of the Texas A&M fuel element is such that it is unlikely that there will be any significant movement of the fuel below or above the poison plates in the event of a 30 ft. end drop at either end.

The following analysis shows that the fuel elements will not fail under end drop conditions on either end. The worst case situation is for the plug end drop (bottom) with the fuel element resting in the steel bars (2/16 in. x 7/16 in.) as shown on BMI-1 Fuel Basket Modification Drawing BCL-000-501. In this situation eight of the twelve elements could be located such that only 50 percent of the end of the plug is supported by the steel bars.

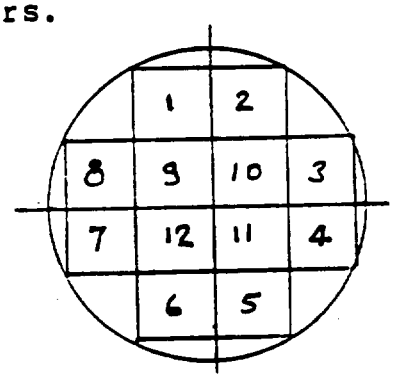

Elements 1, 2, 5, 6, 9, 10, 11, and 12 can have as little as one half of the end plug bearing surface in contact with the steel grid.

The maximum bearing stress occurs on the edge of the 6061-T6 aluminum plug as shown below.

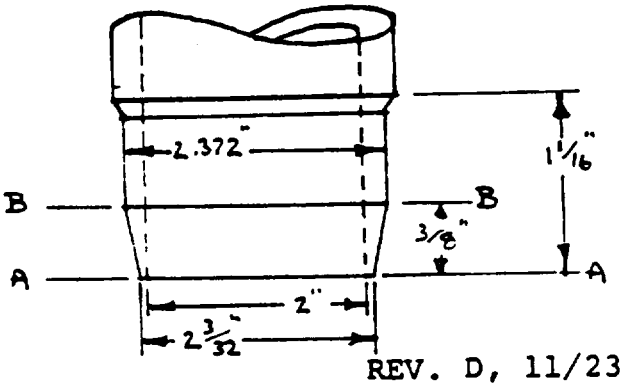

Inside Diameter = 2.0 in.

<u>Section A-A</u>. end

Area = $\pi/4\ (2.094^2 - 2^2)$

= .211 in.^{2}

One-half is in contact

.211 in.^{2}/2 = .10 in.^{2}

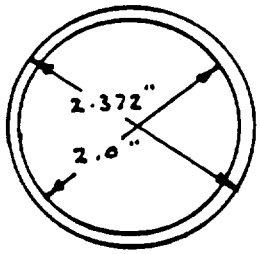

Section B-B
Area = $\pi/4\ (2.372^2 - 2^2)$
= 1.53 in.^{2}.

The allowable bearing yield stress for the 6061 fitting is 22,000 psi. The weight of the Texas A&M MTR fuel element is 10.5 lb. The acceleration is a bottom end drop is 368 gs (ref. page 2.86) 10.5 x 368 = 3,864 lb.

$$f_{bry} = \frac{P}{A} = \frac{3864\ \text{lbs}}{.10\ \text{in}^2} = 38{,}640\ \text{psi}$$

This exceeds the allowable bearing yield stress by a factor of 1.76 and will result in yielding of the thin edge of the 6061 end plug until sufficient area has been flattened out to support the fuel element at the allowable yield stress. Conservatively assuming that yielding will cease when an area three times that given above, 3 x .10 = .30 in.^{2}, the fuel element will have moved approximately 1/16 of an inch. At that point the bearing yield stress will be:

$$f_{bry} = \frac{4063.5}{.30} = 13{,}545\ \text{psi}$$

$$F_{bry} = 22{,}000\ \text{psi}$$

$$M.S._y = \frac{22{,}000}{13{,}545} - 1 = .62$$

The movement of approximately 1/16 of an inch is considered insignificant.

Top End Drop - Texas A&M MTR Fuel

The top end drop for the Texas A&M MTR fuel is less severe than the bottom end drop. By constrast, the maximum impact force is 87.5 G on the top of the cask. Conservatively assuming no attenuation, this shock force is also applied to the fuel.

The end view of the aluminum side plates which hold the fuel plate is shown below:

FIGURE WITHHELD UNDER 10 CFR 2.390

End area = (3.15)(.154) + (19)(.122)(.033) 2 = 1.1232 in. ^{2}

The fuel elements bear against a smooth steel plate in the top end drop. The weight of the fuel element is 10.5 lb. The impact force is 10.5 lb x 87.5 G,. 918.75 lb. The allowable bearing yield stress for 6061-76 is 22,,-0 psi.

M.S. 22,000 -i 1 high

(Paragraph deleted)

2.12.6 Structural Evaluation of BMI-1 Cask with Eight MURR Spent Fuel Elements

Cask Containment

The containment criteria specified in 10 CFR 71.51 and therein referenced part 71 sections are met by the BMI-1 Type B package. Analysis of this is presented in the BMI-1 SAR, Section 2. When used to ship irradiated MURR fuel assemblies, the cask itself will be as described in the SAR. We comment below on some specific points, in particular those involving the MURR fuel and cask basket.

Closure Bolts

In SAR Section 2.6, p. 2.30, the total net outward force on the lid due to 100 psig internal pressure and rubber sealing gasket compression is 34,130 pounds. No credit is taken for the 1,100 pound weight of the lid (p. 1.5). Using a bolt cross-section area of 0.563 in^2, the stress in each of the 12 bolts is 5,052 psi. This is well below the tensile yield stress for 304 stainless steel of 30,000 psi, and the ultimate stress 75,000 psi, given in SAR Table 2.23 on p. 2.2. The bolt (stud) material is stated in 3.4.2 as 304 SS.

In addition to the above 5,052 psi stress, we may consider a pre-load due to torque on the bolt nuts when the lid is initially tightened down. The pre-load force is

$$F_l = \frac{T}{cd_B} = \frac{50 \text{ ft.lb.}}{(.15)(.8466 \text{ in.}/12)} = 4{,}725 \text{ lb.}$$

where T is the torque, c is a lubricated bolt-nut friction factor, and d_B = .8466 inch is the bolt minor (inside threads) diameter. This equation is from

Machine Design: Theory and Practices (Macmillan Publishing Co.) p.816. The pre-load bolt stress is then 4725 lb/0.563 in^2 = 8,393. psi and the sum of the stresses is 5,052 + 8,393 = 13,445 psi. This is a factor 2.2 below the yield stress and well below the ultimate stress.

Minimum Coolant Temperatures

With the most unfavorable ambient temperature of T_a = - 40°F = 420°R [10 CFR 71.71(b)(2)], a decay power of 0.5 kW = 1700 Btu/hr, a cask surface area of 49.7 ft^2, and heat transfer coefficient

$$h = (0.40)(T_s - T_a)^{1/3}$$

the cask surface temperature T_s is found from

$$1700 = (0.173)(0.5)(49.7)\left[\left(\frac{Ts}{100}\right)^4 - \left(\frac{420}{100}\right)^4\right] + (0.40)(49.7)(Ts-420)^{4/3}$$

This equation is explained in our Thermal Evaluation section. The solution is T_s = -16°F. With a 10°F rise through the lead and steel walls, and 10° across the cavity-basket water gap and fuel, the water in the fuel annulus would be just above 0°F.

If we consider the unfavorable but less extreme ambient temperature T_a = - 20°F, [10 CFR 71.71(b)], the cask surface temperature is + 3°F and the water in the fuel annulus center would be about 25°F. This could be raised above the freezing temperature of water by following SAR Section 3.4.3 and covering the cask with a heat-transfer reducing blanket.

In any shipment at sub-zero °F ambient temperature, we will consider the actual decay power and our measurement of the cask surface temperature under the blanket. If there is a risk of coolant freezing, sufficient antifreeze will be added to the cask to prevent damage of any component of the package by freezing, (reference Certificate of Compliance No. 5957).

Pressure Relief Valve Test

The pressure relief valve will be tested on an annual basis, either by Cintichem, Inc., the BMI-1 cask owner, or by MURR.

Normal Conditions of Transport

SAR Section 2. Structural Evaluation and Section 3. Thermal Evaluation, and the MURR submissions explain that the radioactivity containment requirements of 71.51(a)(1) for normal conditions of transport are met by the cask integrity.

In addition, for radioactive material to escape from the fuel elements, the plate cladding must be penetrated by forced cutting, or by temperatures above the normal transport conditions. The stainless steel basket with its lid holds the elements firmly in place. It is not credible that the cask lid come off. Therefore it is not credible that any significant amount of radioactivity can be released from a fuel element.

Hypothetical Accident Conditions

As in the paragraph above, even in accident conditions, the cask lid does not come off. In the hypothetical fire, fuel plates do not get to failure temperatures, as explained in our Thermal Evaluation.

Accordingly, we conclude that there would be no escape of krypton-85 exceeding 10,000 curies in one week and no escape of radioactive material exceeding A_2 in one week. The last paragraph of our Shielding Evaluation shows that in a hypothetical accident, there would be no external radiation dose rate exceeding one rem per hour at one meter from the external surface of the package. The requirements of 10 CFR 71.51(a)(2) are met.

2.12.7 Analysis of MITR Fuel Assemblies in BMI-1 Cask

Normal Conditions of Transport

As explained in the BMI-1 Safety Analysis Report, the integrity of the BMI-1 cask meets containment requirements of 71.51(a)(1) for normal conditions of transport.

In addition, the MITR-II elements will be secured using spacers inside the Missouri basket so as to preclude any movement within the cask which might cause fuel damage. The cladding integrity has been tested for all MITR-II fuel elements with no fission product leakage indicated. The lower limit of detection for this testing is well below that of 10^{-6} A_2 per hour, as prescribed in 10 CFR 71.51(a)(1).

Thirdly, normal conditions of transport will not result in any changes in external radiation levels. Even in an absence of the spacers, the fuel elements would only shift towards the outside of the cask a total distance of less than one inch, resulting in an insignificant increase in external radiation levels.

Hypothetical Accident Conditions

As also explained in the BMI-1 SAR the cask integrity is maintained during hypothetical accident conditions. Even if the fuel were damaged, there would be no escape of Krypton-85 exceeding 10,000 curies in one week and no escape of radioactive material exceeding A_2 in one week. Therefore the requirements of 10 CFR 71.51(a)(2) are met.

The University of Missouri analyzed the Missouri basket under the hypothetical fire accident conditions and concluded that the maximum fuel temperature would reach 724 °F, which is well below the clad failure temperature. This analysis is exactly applicable to the MITR-II fuel. It should be noted however, that there is a larger gap between the fuel and basket in the MITR-II case, so that there will be an overall lower fuel temperature. Section 5.4.2.1 of the BMI-1 SAR also explains that the only shielding loss in the hypothetical fire accident is a 3 inch drop in lead level at the corner of the cask, which resulted in a dose less than 1 Rem/hr at 1 meter. Since an MITR-II shipment contains less volume and has a lower external dose rate than that analyzed in the SAR, hypothetical radiation levels will be even less.

Finally, 10 CFR 71.51(a)(2) requires that there be no escape of Krypton-85 greater than 10,000 curies in one week. There is presently no combination of eight MITR-II spent fuel elements that approaches an inventory of 10,000 curies of Kr-85.

2.12.8 Stress Analysis - HFBR Baskets

E-2.1 Introduction

The function of the baskets is to provide structural support and maintain separation between fuel assemblies during transport. During the hypothetical drop accident, the fuel assemblies and baskets will be subjected to an impact load due to their inertia.

The structural analysis for the BMI-1 Package (Appendix E-1) indicated the Package would be subjected to the following "g" loads.

Bottom impact - the cask deforms 1.92 inches (Appendix E-1, p 2.32).
$g = 2 \times 360 / 1.92 = 375$

Top impact - the cask deforms 1.06 inches (Appendix E-1, p 2.35).
$g = 2 \times 360 / 1.06 = 680$

Side impact - the cask deforms 1.44 inches (Appendix E-1, p 2.38).
$g = 2 \times 360 / 1.44 = 500$

Corner impact - the cask deforms 5.63 inches (Appendix E-1, p 2.40).
$g = 2 \times 360 / 5.63 = 128$

The "g" loading on the fuel/baskets will be less than the above values due to damping in the cask body. This analysis conservatively assumes that the entire "g" load is transmitted to the internals.

From Drawing No. BNL 93-001 (Rev. 1), it can be seen that the basket is fabricated from 3/16 inch thick and 1/4 inch thick 304 stainless steel plates. Each basket contains 10 rectangular fuel compartments with a length of 25-3/8 inches. The fuel compartments are about 3 inches square. Fuel assemblies are supported at the bottom of each compartment by 3/16 inch thick by 1 inch wide pieces welded to the uprights which define compartments. The basket lifting lugs are 1 3/4 inch wide by 1/4 inch thick pieces welded to the compartment exterior at two locales 180 degrees apart. The opposing sides have 1/4 inch square separators.

The envelope diameter defined by the basket is 15 1/8 inches while the interior diameter of the cask is nominally 15 1/2 inches diameter. The resulting diametral clearance, 3/8 inch, minimizes basket movement from side to side. Each basket is 25 3/4 inches long and the spacer plate is 3/8 inch thick for a total length of 51 7/8 inches. The nominal internal height of the internal cavity is 54 inches. The clearance in the cavity is 2 1/8 inches.

Component weights relevant to the basket stress analysis are as follows:

Fuel assembly (lbs) - 9.9
Spacer plate (lbs) - 18
Basket total (lbs) - 185

All internals (lbs) - 586
Single basket plus fuel (lbs) - 284

This Appendix presents the analysis to show that the basket is not adversely affected when the cask is subjected to the 30 foot drop accident. Since the load under the 30 foot drop condition is the worst case, the basket can safely react to the designated loads for both normal and accident conditions.

The allowable yield stress for 304 stainless steel at 200 degrees F is 25,000 psi. The ultimate stress at this same temperature is 71,000 psi. These values were used throughout the stress analysis.

E-2.2 Bottom Drop

Downward or axial loads are carried by the 1 inch strips (3/16 inch thick) at the bottom of the basket. For a single assembly at 9.9 lbs, the load on the strips is:

$$P = 9.9 \times 375 = 3{,}713 \text{ lbs}$$

E-2.2.1 Strip Plate Bending Stress

From the referenced drawing, all compartments have 6 square inches of support strip at the compartment bottom. The uniformly distributed load, W on the strip plate is:

$$W = P/6 = 3{,}713/6 = 619 \text{ lbs/in}^2$$

The maximum bending stress at a 3" x 1" strip plate are calculated from:

$$S_b = 0.798 \times W\ (1)^2 / (3/16)^2 = 14{,}050 \text{ psi}$$

The allowable bending stress is the yield stress (S_a) or 25,000 psi.

The margin of safety is:

$$MS = (S_a/S_b) - 1$$

$$MS = (25{,}000/14{,}050) - 1$$

$$MS = +0.78$$

E-2.2.2 Strip Plate Shear Stress

Shear stress in the plate is:

$$S_s = P / (2 \times 3/16 \times (3 + 1 + 1))$$

$$S_s = 1{,}980 \text{ psi}$$

The allowable shear stress is 60 percent of the yield stress:

$S_a = 0.6 \times 25{,}000 = 15{,}000$ psi

The margin of safety is:

$MS = (S_a/S_s) - 1$

$MS = (15{,}000/1{,}980) - 1$

$MS = +6.57$

E-2.2.3 Strip Plate To Basket Weld Stress

From the referenced drawing the strip plate is attached to the basket with a 1/8 inch fillet weld. The load on the plate is P/2 or 1,857 lbs.

The weld area is:

$A = (3 + 1 + 1) \times 0.125 = 0.625$ in^2

The weld stress is:

$S_w = 1{,}857 / (0.625 \times 0.707 \times 0.85)$

$S_w = 4{,}944$ psi

The allowable weld stress (S_a) is 30 percent of the ultimate stress:

$S_a = (0.3) \times 71{,}000$ psi $= 21{,}300$ psi

The margin of safety is:

$MS = (S_a/S_w) - 1$

$MS = (21{,}300/4{,}944) - 1$

$MS = +3.31$

E-2.3 Top Drop

During the top drop case, fuel assemblies are not contained and the spacer plate is loaded by assemblies in the bottom basket.

E-2.3.1 Spacer Plate Bending Stress

For a single assembly at 9.9 lbs, the load on the 3/8 inch thick spacer plate is:

$P = 9.9 \times 680 = 6{,}732$ lbs

The maximum bending stress on a 3 x 3 inch square section of spacer plate, simply supported at all edges, is:

$$S_b = 0.287 \times P / (3/8)^2$$

$$S_b = 13{,}740 \text{ psi}$$

The allowable bending stress (S_a) is the yield stress or 25,000 psi.

The margin of safety is:

$$MS = (S_a/S_b) - 1$$

$$MS = (25{,}000/13{,}740) - 1$$

$$MS = +0.82$$

E-2.3.2 <u>Spacer Plate Shear Stress</u>

Shear stress in the plate is:

$$S_s = P / (3/8 \times (3 + 3 + 3 + 3))$$

$$S_s = 6{,}732 / 3/8 \times 12 = 1{,}496 \text{ psi}$$

The allowable shear stress (S_a) is 60 percent of the yield stress:

$$S_a = 0.6 \times 25{,}000 = 15{,}000 \text{ psi}$$

The margin of safety is:

$$MS = (S_a/S_s) - 1$$

$$MS = (15{,}000/1{,}496) - 1$$

$$MS = +9.03$$

E-2.3.3 <u>Basket Frame Yield Stress</u>

Axial loads are carried by the 1/4 inch thick frame plates (21) with a total cross sectional area of:

$$A = 1/4 \times (2x14 + 2x10 + 13x3.25 + 2x2.25 + 2x0.25) + 1/2 \times 2 \times 3$$

$$A = 26.81 \text{ in}^2$$

The total axial load on the basket frame is:

$$P = (10xP_a + P_b + P_s) \times 680 = 302 \times 680 = 205{,}360 \text{ lbs}$$

Where:

P_a = Fuel assembly weight (9.9 lbs)
P_b = Basket weight (185 lbs)
P_s = Spacer plate weight (18 lbs)

The maximum yield stress is:

$$S_m = P/A = 205{,}360 / 26.81 = 7{,}660 \text{ psi}$$

The allowable yield stress (S_a) is 25,000 psi.

The margin of safety is:

$$MS = (S_a/S_m) - 1$$

$$MS = (25{,}000/7{,}660) - 1$$

$$MS = + 2.26$$

E-2.4 Side Drop

During the side drop, the fuel assemblies in the two top tiers of compartments plus the basket, will produce compressive loads on the basket bottom compartment plates. In the same orientation, the lifting lug plates will be loaded in compression and the compartment plate attached to the lifting lug will be in bending.

E-2.4.1 Basket Plate Stress

The seven assemblies in the upper compartments will load the three lower compartments. The lower compartments will conservatively see a combined load equal to the weight of seven assemblies plus the basket weight, or 255 lbs.

$$P = (7xPa + Pb) \times 500 = 127{,}150 \text{ lbs}$$

Where:

P_a = Fuel assembly weight (9.9 lbs)
P_b = Basket weight (185 lbs)

The total cross sectional area of the plates is:

$$A = 4 \times 1/4 \times 25.37 = 25.37 \text{ in}^2$$

The yield stress on the plates is:

$$S_p = P/A = 127{,}150 / 25.37 = 5{,}012 \text{ psi}$$

The allowable yield stress (S_a) is 25,000 psi.

The margin of safety is:

$$MS = (S_a/S_p) - 1$$

$$MS = (25{,}000/6{,}692) - 1$$

$$MS = +3.99$$

E-2.4.2 Basket Lifting Lug Compression

All ten assemblies in the basket plus the basket will load the lifting lug.

$$P = (10xP_a + P_b) \times 500 = 142,000 \text{ lbs}$$

Where:

P_a = Fuel assembly weight (9.9 lbs)
P_b = Basket weight (185 lbs)

The total cross sectional area of the plate is:

$$A = 1/4 \times 25.37 = 6.34 \text{ in}^2$$

The yield stress on the plates is:

$$S_p = P/A = 142,000 / 6.34 = 22,440 \text{ psi}$$

The allowable yield stress (S_a) is 25,000 psi.

The margin of safety is:

$$MS = (S_a/S_p) - 1$$

$$MS = (25,000/22,400) - 1$$

$$MS = +.116$$

E-2.4.3 Bending of Compartment Plate

All ten assemblies in the basket plus the basket will load the lifting lug and subject the bottom compartment to bending. This location has been reinforced with a 1/2 inch plate to stiffen the compartment at this location.

$$P_c = (10xP_a + P_b) \times 500 = 142,000 \text{ lbs}$$

Where:

P_a = Fuel assembly weight (9.9 lbs)
P_b = Basket weight (185 lbs)

$$\text{Moment}(M) = P \times L / 8 = 142,000 \times 3 / 8$$

$$M = 53,250 \text{ lb in}$$

$$I = 25.37 \times (3/4)^3 / 12 = .892 \text{ in}^4$$

The bending stress on the plate is:

$Sb = (M/I) \times 3/8 = (53,250 / 0.892) \times 0.375$

$Sb = 22,386$ psi

The allowable bending stress (S_a) is 25,000 psi.

The margin of safety is:

$MS = (S_a/S_b) - 1$

$MS = (25,000/22,386) - 1$

$MS = +.116$

E-2.5 Corner Drop

Because the corner drop orientation results in substantially reduced "g" loads and produces axial and lateral components less than those of the side and end drop conditions, they are not presented.

3. THERMAL EVALUATION

3.1 Discussion

3.1.1 Summary of Results

For normal operation with 1.5 kw decay heat with a 130 F ambient temperature, the cask inner liner temperature will be about 227 F. During the hypothetical fire accident, the inner liner temperature will be about 560 F.

The Fermi fuel subassembly will be shipped in the BMI-1 shipping cask, which has been provided with a special basket. During shipment, the cask cavity is filled with water. The void spaces between the fuel rods in the subassembly are filled with a settled bed of copper shot in water. The cask is to be shipped by truck so that under normal conditions the maximum fuel and water temperature is about 230 F.

3.1.2 Maximum and Minimum Decay Heat

(a) BRR/MTR Fuel

The total fission product decay heat is calculated from the data in ORNL-2127[1]. Following the analysis in Reference (1), the Number U-235 atoms in a BRR fuel element is:

$$N = \frac{3.2 \times 10^{10} P}{\sigma \phi}$$

where

P = irradiation power (watts)

σ = fission cross section used in Tables = 580 barns

ϕ = thermal neutron flux.

(1) References to Section 3. found in Section 3.6.1.

The maximum U-235 burn-up in a BRR element is 17.5 percent For a fuel loading of 162 g U-235, with a capture to fission ratio of 1.18, the fission product production is 24.1 g. For an irradiation time of 313 days, the irradiation power is P = 24.1 MwD/313 D = 7.7×10^4 watts per element (assuming 1 g U-235 = 1 MwD). Thus, for $\phi = 10^{14}$ n/cm^2 sec:

$$N = \frac{(3.2 \times 10^{20})(7.7 \times 10^4)}{(580)(10^{14})} = 4.25 \times 10^{22} \text{ atoms U-235 per element.}$$

From the data in Reference (1), the total decay heat (beta plus gamma) for an irradiation time of 313 days and a cooling time of 90 days (with $\phi = 10^{14}$) is $q = 10^{-21}$ watts/atom U-235, or:

$$Q = (10^{-21})(4.25 \times 10^{22}) = 42.5 \text{ watts/element} \quad .$$

For 24 elements with the same irradiation history, the decay heat is 24 x 42.5 = 1.02 kw = 3,480 Btu/hr.

(b) Fermi Fuel

(Paragraph deleted)

(c) TRIGA Fuel

The fission product activity was estimated to be 250 curies per element in November, 1970 (based on radiation measurement made at that time). Assuming 2 MEV per event, the decay heat of the fuel is:

$$250 \text{ curies/element} \times 3.7 \times 10^{10} \text{ events/sec/curie} \times$$
$$2 \text{ MEV/event} \times 1.6 \times 10^{-13} \text{ watts/MEV/sec}$$
$$= 2.96 \text{ watts/element} \quad .$$

The total heat load for the cask is 112.5 watts. This is a very conservative estimate since the fuel has cooled ~ 2 years and has a cooling factor greater than 3.0. The BMI-1 cask is licensed to handle up to 1.5 kw of decay heat. Thus, the thermal inventory for this shipment is well within the limits for the cask.

(Paragraph deleted)

(d) EPRI Crack Arrest Capsules

The total decay heat generated by the capsule at discharge is 197 watts. The axial heat rate over the height of the capsule is (197)(12)/21.5 = 110 watts/ft. The cask is rated for contents whose decay heat is up to 1,500 watts. The cavity length is 54 inches. Thus, the axial heat rate permitted for the cask is (1,500)(12)/54 = 333 watts/ft. Thus, the decay heat is within permissible levels.

(e) Union Carbide Process Uranium Oxide Container

The total decay heat of the process oxide may vary up to a maximum of 20 watts per container. Thus for a shipment of twenty-four (24) containers, each producing the maximum decay heat, the total heat generation of the contents is 480 watts. This is below the 1500 watt rating of the cask.

(f) Union Carbide Target U^{235} Special Form Capsules

The total decay heat for the U^{235} target material may vary. The number of capsules permitted per shipment shall be limited so that the total aggregate decay heat generation will not exceed 1500 watts, the rating of the BMI-1 cask.

(g) MURR Fuel Assemblies

A thermal analysis of the case of eight MURR fuel assemblies in the BMI-1 cask was performed. This analysis showed that the maximum surface temperature of the cask would be 182°F, slightly in excess of the 180°F limit permitted by 10 CFR 41.43(g). Starting with data from experimental studies on a GE 700 cask, it was concluded, however that the BMI-1 will experience a 170°F maximum surface temperature. These analyses further concluded that the fuel temperature rise and maximum internal pressure are within acceptable limits. See Appendix 3.6.3.

(h) MITR-II Fuel Elements

In the worst case of a MITR-II fuel element which remains in the MITR core during continuous 5-day-per-week operation until 45% burnup is reached and is then allowed only 90 days cooling, the calculated decay heat is 127 watts. For the maximum eight MITR-II fuel elements permitted, the maximum decay heat load is 1016 watts, less than the 1500 watt rating of the cask. See Appendix 3.6.4.

(i) HFBR Fuel Assemblies

The decay heat from all sources for a 20 HFBR assembly payload was determined using ORIGEN2. The case considered was based on 60 days operation at 60 MW with a full core of 28 assemblies. The ORIGEN2 output was reduced by a factor of 0.71 (20/28) to reflect a 20 HFBR assembly payload. An average fuel assembly decay time of 470 days results in a decay heat load below the MTR fuel limit of 1.02 kw. See Appendix 3.6.5.

3.1.3 Solar Heat

From Reference (3), p 1,636, the solar heating is:

$$Q = 429T \left\{ \epsilon_H A_H \cos \theta_H + \epsilon_V A_V \cos \theta_V \right\}$$

where

T = atmospheric transmittance = 0.6

ϵ = absorptivity = 0.5

A = area of surface

H. = refers to horizontal surface or top of cask

V = refers to vertical surface or side of cask

At noon during the summer solstice, at 40 degrees latitude:

$$\cos \theta_V = 0.96$$
$$\cos \theta_H = 0.284$$

The outside of the cask is 33 inches in diameter and 72.375 inches in height. Thus:

$$A_H = \frac{\pi}{4} D^2 = 5.93 \text{ feet}^2$$

$$A_V = DH = 16.6 \text{ feet}^2 \text{ (protected area).}$$

The solar heat is:

$$Q = 429(0.6) \left[(0.5)(5.93)(0.96) + (0.5)(16.6)(0.284) \right]$$

$$= 732 + 607 = 1{,}339 \text{ Btu/hr.} = 0.392 \text{ kw}$$

3.2 Summary of Thermal Properties of Materials

The materials' thermophysical properties which were employed are shown in Table 3.1. Also, since it has been well demonstrated that the lead will contract away from the outer shell after casting (fabrication experience indicates a potential gap of 0.060-0.100 inch), the thermal model included a variable air gap (Node 118) which has an effective thermal conductivity that increases with temperature as shown in Figure 3.1.

3.3 Technical Specifications of Components

Relief Value - 75 psig

Pressure gauge - 30 in Hg vacuum to 100 psig pressure.

3.4 Thermal Evaluation for Normal Conditions of Transport

3.4.1 Thermal Model

The analysis for normal operation were performed assuming only radia. heat flow from the contents through the cask walls to the environment.

TABLE 3.1 THERMOPHYSICAL PROPERTIES EMPLOYED FOR LEAD, STEEL, AND ALUMINUM

Lead

Density = 705 pounds/feet^3
Melting Temperature = 621 F
Latent Heat = 10.5 Btu/pounds

Temperature, F	Thermal Conductivity, Btu/hr-ft-F	Specific Heat, Btu/lb	Emissivity
32	20.1	0.0303	1.0
212	19.6	0.0315	1.0
572	18.0	0.0338	1.0
621	8.8	0.0337	1.0
900	8.9	0.0326	1.0

Steel

Density = 488 pounds/feet^3
Latent Heat = 120 Btu/lb
Melting Temperature = 1,800 F

Temperature, F	Thermal Conductivity, Btu/hr-ft-F	Specific Heat, Btu/lb	Emissivity
32	8.0	0.11	0.8[a], 1.0[b]
212	9.4	0.11	0.8, 1.0
572	10.9	0.11	0.8, 1.0
932	12.4	0.11	0.8, 1.0
1,800	15.0	0.11	0.8, 1.0

(a) For steel surface exposed to flame, ε = 0.8.

(b) For steel surfaces viewing each other across internal air gaps, ε = 1.0.

TABLE 3.1 THERMOPHYSICAL PROPERTIES EMPLOYED FOR LEAD, STEEL, AND ALUMINUM (Continued)

Aluminum, 6061-T6

Density = 169 pounds/feet^3
Melting Temperature = 1,140 F
Latent Heat - 128 Btu/pounds

Temperature, F	Thermal Conductivity, Btu/hr-ft-F	Specific Heat, Btu/lb	Emissivity
77	89.5	0.214	0.15
600	135.0	0.214	0.15

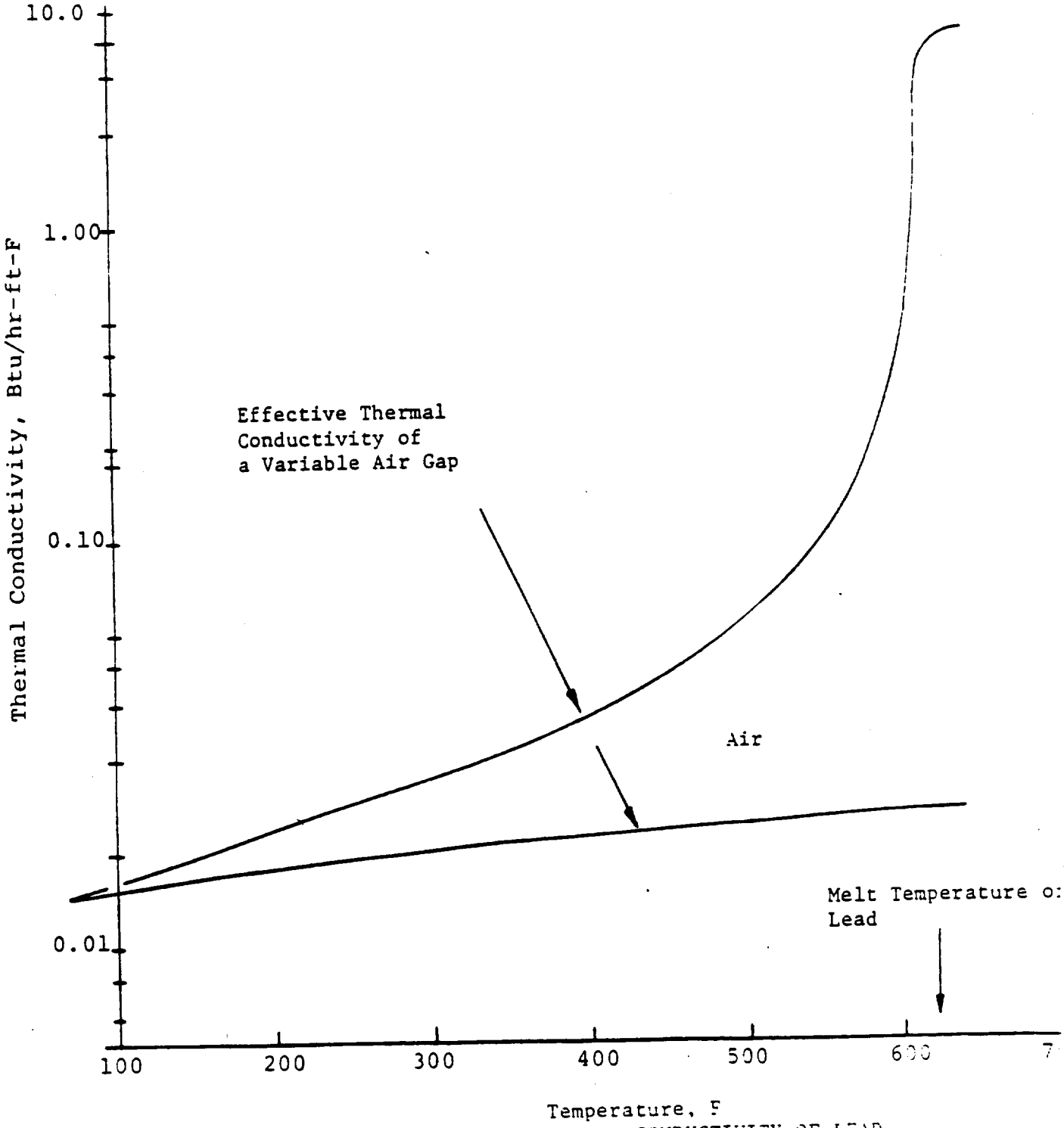

FIGURE 3.1. EFFECTIVE THERMAL CONDUCTIVITY OF LEAD TO-SHELL INTERFACE, GAP (NODE 118)

3.4.2 Maximum Temperature

3.4.2.1 BRR/MTR Fuel

(a) External Heat Transfer

During normal operation, heat is dissipated from the outside surface of the cask by radiation and natural convection in air. The heat transferred by radiation is:

$$Q_r = 0.173\ \varepsilon A \left[\left(\frac{T_o}{100}\right)^4 - \left(\frac{T_a}{100}\right)^4 \right],$$

and the heat transferred by convection is:

$$Q_c = h_c A_c (T_0 - T_a) \quad ,$$

where

ε = surface emissivity = 0.5 for steel

T_o = cask surface temperature

T_a = ambient temperature = 100 F

$h_c = 0.19(T_o - T_a)^{1/3}$ (McAdams[4], p 173)

$A_r = A_c$ = heat transfer area .

Heat transfer from the outside corners and top of the cask is partly obstructed due to the air pockets built into the lead to provide for lead meltdown space in case of fire. The air pockets also insulate the cask from solar heating. Two estimates of the maximum heat load are made. In the first case, the full solar load and total cask surface area are considered.

In the second case, heat transfer from areas obstructed by air pockets is neglected, and only the solar load on the side is included. In the first case, the total heat load on the outside surface of the cask is Q = 3,480 + 1,339 = 4,819 Btu/hr; and, the heat-transfer area including the top and bottom is A = 52.1 + 11.86 = 63.96 ft^2. In the second case, the solar load is 540 Btu/hr for a total heat load of 4,020 Btu/hr; and the heat-transfer area, neglecting the top and corners, is A = 46.3 + 3.4 = 49.7 ft^2. In the first case, the heat flux is 75.4 Btu/hr ft^2, and in the second case is 80.9 Btu/hr ft^2. The second case is calculated below since it leads to conservative results (higher surface temperatures).

The total heat, removal capacity of the cask is: $Q=Q_r + Q_c$, or

$$Q = (0.173)(49.7)(0.5)\left[\left(\frac{T_o}{100}\right)^4 - \left(\frac{560}{100}\right)^4\right] + 0.19(49.7)(T_o - 560)^{4/3} .$$

For:

$$Q = 3{,}480 + 540 = 4{,}020 \text{ Btu/hr}, \quad 4{,}020 = 4.29\left[\left(\frac{T_o}{100}\right)^4 - 981\right]$$

$$+ 9.44(T_0 - 560)^{4/3} ,$$

and:

$$T_0 = 617 \text{ R} = 157 \text{ F}.$$

Thus, the maximum cask surface temperature will be 157 F, assuming there is no heat loss (or addition), through the top and corners of the cask. The surface temperature is below 180 F, which meets the AEC requirements.

(b) Heat Transfer in Cask Wall

The temperature drop across the lead in the wall of the cask is:

$$\Delta T = \frac{Q}{2\pi kL} \ln D_2/D_1 = 4.05 \text{ F},$$

where

$$Q = 3{,}480 \text{ Btu/hr}$$
$$k = 19$$
$$L = 5 \text{ feet}$$
$$D_2 = 32 \text{ inches}$$
$$D_1 = 16 \text{ inches} \quad .$$

The total temperature drop across the inside (thickness = 0.25 inches) and outside (thickness = 0.5 inch) steel plates is ΔT = 0.7 F.

As the lead solidifies in the manufacturing process, a small air gap is formed between the outside steel shell and the lead. The thickness of this gap is estimated to be 0.0817 inch. The heat transferred by conduction and radiation across the gap is:

$$Q = \frac{kA\Delta T}{t} + 0.173 \text{ FA } \frac{4T^3 \Delta T}{10^8}$$

where

$$Q = 3{,}430 \text{ Btu/hr}$$
$$A = 50.2 \text{ ft}^2$$
$$t = 0.0817 \text{ inch}$$

$$F = 0.231$$
$$T = 180\ F = 640\ R \quad .$$

The total temperature drop across the cask wall is ΔT = 23.8 F. It is expected that the lead will settle during transportation and close the air gap. Thus, the temperature drop across the wall of the cask should decrease in later shipments.

The total temperature drop across the cask wall is ΔT = 4.05 + 0.7 + 23.8 = 28.6 F. The temperature at the inside surface of the cask wall is T = 157 + 28.6 = 185.6 F.

(c) Internal Heat Transfer

During normal operation, the cavity of the cask is filled with water, and the fuel elements are cooled by natural circulation of the water. The water flows up through and around the fuel elements to the top of the cavity and then flows down through the space between the cask wall and the fuel elements. The heat absorbed by the water as it flows up through the elements is dissipated as the water flows down past the cooler cask wall.

The natural convection heat transfer can be calculated from the pertinent pressure drop and heat balance equations. These equations have been solved and placed in a form convenient for calculation in Reference 5. According to the analysis in Reference 5, the equations which must be solved for the maximum water temperature T(L) are:

$$T(L) = T_c = \frac{\gamma}{1-e^{-\alpha L}}$$

$$\gamma = T(L) - T(o) = \frac{Q}{C\rho}\left(\frac{1}{AV}\right) \tag{2}$$

$$\alpha L - 2(F_A - 1) = \frac{384}{\rho g \beta}\left[(A_i D_i^{\,2})^{-1} + (A_o D_o^{\,2})^{-1}\right]\left(\frac{AV}{\gamma}\right) \tag{3}$$

$$\alpha L = \frac{P_H L}{C\rho}\left(\frac{h_o}{AV}\right) \tag{4}$$

$$h_o = 0.05\left[\frac{\rho^2 k^2 g \beta c}{\mu}\right]^{\frac{1}{3}}\left(\frac{\gamma}{\alpha L}\right)^{\frac{1}{3}} \tag{5}$$

where

$T(L)$ = maximum water temperature (at top of cask)
$T(o)$ = water temperature at bottom of cask
T_c = cask cavity wall temperature
Q = decay heat
AV = flow velocity (ft^3/hr)
A_i = total element flow area (up-flow region)
D_i = equivalent diameter of element region
A_o = flow area of down-flow region
D_o = equivalent diameter of down-flow region
F_A = axial peaking factor
PH_L = heat-transfer area = area of cavity wall
g = gravitational constant

water properties:

c = specific heat
ρ = density
μ = viscosity
β = volume expansivity (F^{-1})
k = thermal conductivity

The required numerical data are:

$T_{av} \sim 195$ F

$C = 1.0$ Btu/16 F

$\rho = 60.2$ pounds/ft^3

$\frac{384\mu}{\rho g \beta} = 0.28 \times 10^{-4}$

$\left[\frac{k^2 \rho^2 g \beta C}{\mu} \right]^{\frac{1}{3}} = 487$

$F_A = 1.40$

$A_o = 68.5$ inches^2

$D_o = 2.76$ inches

$A_i = 88.7$ inches^2

$D_i = 0.477$ inches

$P_H = 48.7$ inches

$L = 52.5$ inches

$Q = 3{,}480$ Btu/hr

Using these numerical data, Equations (2), (3), (4), and (5) become:

$$\gamma = 57.8/AV \tag{2}$$

$$\alpha L = 0.8 + 0.03\ (AV/\gamma) \tag{3}$$

$$\alpha L = 0.295\ (h_o/AV) \tag{4}$$

$$h_o = 24.4\ (\gamma/\alpha L)^{\frac{1}{3}} \tag{5}$$

The solutions to these equations are $\gamma = 4.3$ F, $\alpha L = 0.896$, $AV = 13.5$ ft^3/hr, and $h_o = 41.2$ Btu/hr ft^2 F. From Equation (1), $T(L) - T_c = 7.3$ F.

From Section 3.4.2.1(b), the maximum inside cask wall temperature is $T_c = 185.6$ F. The maximum water temperature is $T(L) = 185.6 + 7.3 = 192.9$ F.

The design pressure of this cask is 100 psig so that the maximum permissible operating pressure is 50 psig. Thus, the

maximum operating temperature (193 F) is well below the boiling point (298 F) at the maximum permissible operating pressure.

3.4.2.2 Fermi Fuel

(Paragraphs deleted up to Section 3.4.2.3, p. 3.18)

Material Deleted

Material deleted

3.4.2.3 EPRI Crack Arrest Capsules

It was shown in the September 8, 1969 Addendum that for a 130 F maximum temperature and 1500 watt thermal load, the

outside wall temperature is about 190 F and the cask wall it is about 37 F. For a 100 F ambient with 1,500 watts decay heat the outside wall temperature would be 190-30 = 160 F. For the reduced heat load of 110 watts/ft, the outside wall temperature would be approximately (160-100)(110/333) + 100 = 120 F. The Δt through the cask wall would be (37)(110/333) = 12 F. Thus, the cavity wall temperature would be about 120 + 12 = 132 F. These temperatures are conservatively high since they assume no radial heat flow in the cask wall.

The temperature of the capsule is calculated assuming that all cooling take place by convection and radiation. The capsule will be transported without a canister. However, a wire mesh basket having a maximum wire size of 11 gage (0.125-inch) and minimum mesh size of 1.0 inches may be used to aid in handling the capsules. Thus, it is assumed that convection and radiation heat transfer will take place directly between the capsule wall and the cask inner cavity wall, Figure 3.2.

In order to facilitate the calculations, it is assumed that the cavity wall is a plane, as wide as the capsule (14 inches), as tall as the capsule (21.5 inches), and located approximately 4 inches away. From McAdams[6] the convection heat transfer correlation is given by:

$$Nu = \frac{C}{(L/x)^{1/9}} (Gr \cdot Pr)^n \quad .$$

where

$$Nu = \frac{hx}{k}$$

x = distance between planes = 1/3 ft

k = fluid thermal conductivity

L = height of planes = 1.79 ft

$Gr = a\, x^3\, \Delta t$

a = fluid property constants in Grashof Number

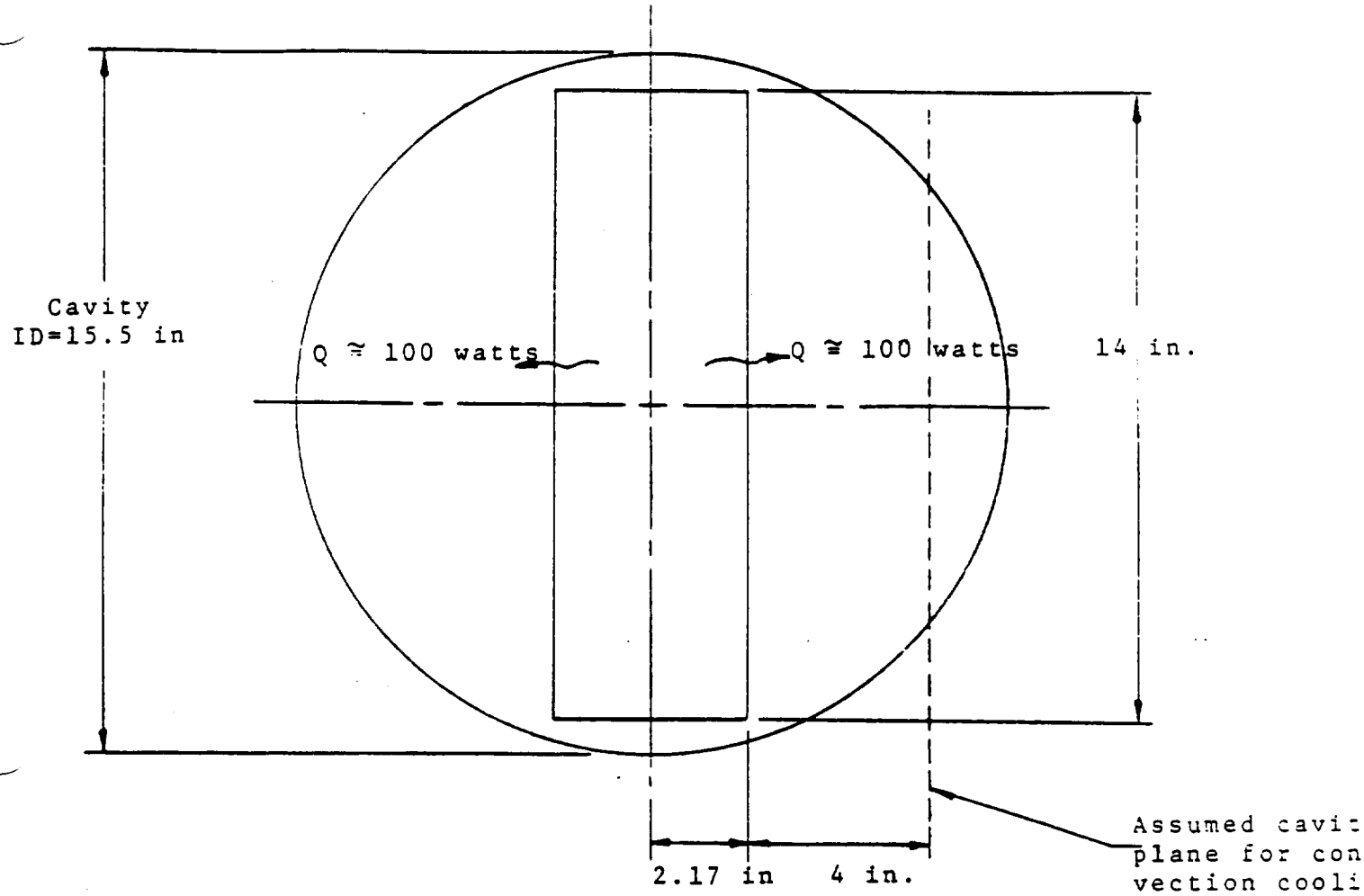

FIGURE 3.2. SKETCH OF MODEL FOR HEAT FLOW FROM EPRI CRACK ARREST CAPSULE TO CAVITY WALL

Pr = Prandl number which is function of fluid property.

For

$$Gr > 2(10^4);\ C = 0.071 \text{ and } n = 1/3 \quad .$$

Thus

$$h/k = 0.0589\ (aPr)^{1/3}\ \Delta t^{1/3}$$

Heat transfer by convection is expressed by:

$$Q_{cv} = hA\Delta t$$

A = area of plane surface = (14)(21.5)/144 = 2.09 ft^2

h = coefficient from above correlation .

Then

$$Q_{cv} = 0.123\ k\ (aPr)^{1/3}\ \Delta t^{4/3}$$

Heat transfer by radiation is expressed by:

$$Q_r = FeFa\sigma A(T_1^{\ 4} - T_2^{\ 4})$$

where Fe = emissivity factor

$$= \frac{1}{\frac{1}{E_1} + \frac{1}{E_2} - 1}$$

E_1 = emissivity of capsule = 0.2

E_2 = emissivity of cask wall = 0.5

$Fe = 0.167$

Fa = view factor = 1.0

$\sigma = 1.73\ (10^{-9})\ R^4$

$A = 2.09\ ft^2$

T_1 = capsule temperature, R

T_2 = cask cavity temperature, R

Thus

$$Q_r = 6.04\ (10^{-10})(T_1^{\ 4} - T_2^{\ 4})$$

It is assumed that the Δt is about 200 F and that the mean air temperature between the capsule and the cask wall is about 230 F. Then the air properties are:

$k = 0.0188$ Btu/hr ft F

$a = 4.78(10^5)/ft^3$ F

$Pr = 0.68$

$T_1 = 460 + 132 + 200 = 792$ R

$T_2 = 460 + 132 = 592$ R

Substituting the values in the equations above results in the following:

$$Q_{cv} = 186 \text{ Btu/hr}$$

$$Q_r = 163 \text{ Btu/hr}$$

And the total heat flow is 349 Btu/hr = 102 watts. Thus, the capsule temperature for normal transportation is about 332 F.

3.4.2.4 Union Carbide Process Uranium Oxide Containers

During normal transport the heat is transferred from the containers to the inner wall of the cask by free air convection and radiation. The length of the internal volume of the containers is approximately 10.75 inches. However, the process oxide contents will fill only about 10 percent of this volume. In order to determine if the axial temperature gradient of the container would be significant for internal heat transfer calculations, an analytical model of a single isolated container was developed, Figure 3.2(a). The model assumed that all the oxide was in a powder bed, 1-inch deep at the bottom of the container. It was further assumed that heat transfer from the oxide bed to the container was by conduction at the oxide-container interface and by radiation from the top of the bed to the inner surface of the container walls. Transfer of heat from the container to the environment was assumed to be by convection only. These assumptions were made for purposes of convenience and are considered conservative. Any convection within the container would tend to decrease the axial temperature difference and "flatten the gradient". The effect of radiation from the outer surface would also be to flatten the gradient. Thus neglecting internal convection and external radiation would tend to result in a higher axial gradient of the container.

The external boundry temperature was estimated as the approximate cavity liner temperature for normal transportation. Its acutal value is of minor significance since the objective of these analyses was to determine the axial temperature gradient and not absolute values. The problem was solved using the TRUMP computer program[7]. Properties for the UO_2 powder bed are as follows:

Node 1: UO_2 Powder; 20 Watts decay heat
Nodes 9 to 22: 6061-T6 Aluminum

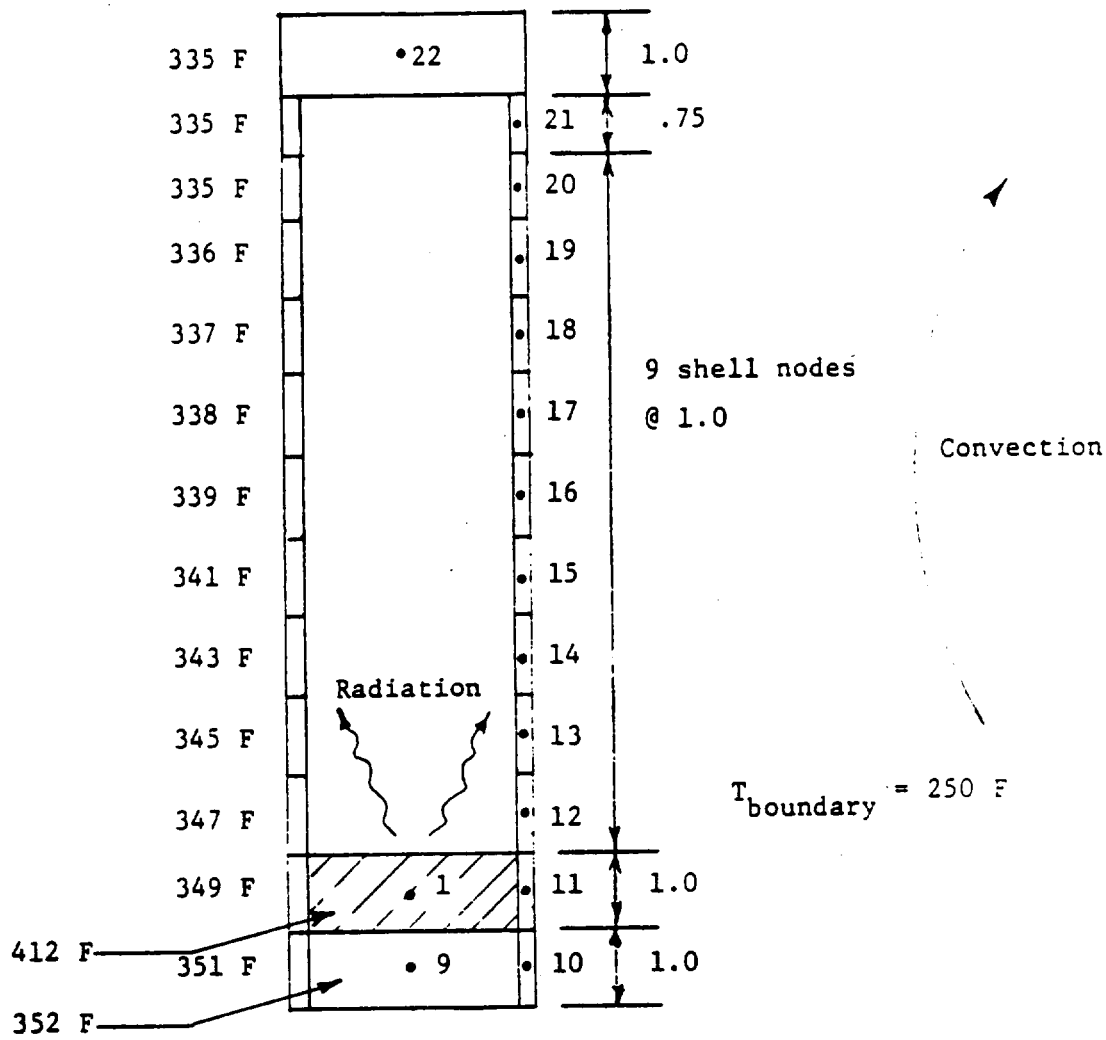

Figure 3.2(a) Analytical Thermal Model of Union Carbide Process Uranium Oxide Container and Steady-State Temperature Profile

UO_2 powder: emissivity = 0.9

Conductivity

Temperature, F	Value, BTU/hr-ft-F
500	1.45
1000	1.27
1500	1.15

Interface Conductance

Node Interface	Value, BTU/hr-ft^2-F
1 to 9	34
1 to 11	14

The results of the analyses shown on Figure 3.2(a) indicate that there is only a 16 F temperature gradient along the length of the container. Thus, if in subsequent internal heat transfer calculations, the container is assumed to be isothermal, the resulting error would be only about 8 F.

The BMI-1 cask currently is designed for shipment in which two baskets, stacked one on the other, are used to transport MTR type fuel elements. Each basket can carry twelve (12) elements. It is planned to use these baskets to hold the Union Carbide process oxide containers. Thus a maximum of twenty-four (24) containers can be shipped. The maximum decay heat from the oxide in each container is 20 watts. Thus, the total decay for 24 containers is 480 watts.

The temperature of the cask and containers during normal transportation was determined by analyses using the TRUMP[7] computer program. A steady state thermal analyses of the BMI-1 cask was initially performed to obtain the cavity liner (wall) temperature. The analytical model of the cask is shown in Figure 3.2(b). The sketch of Figure 3.2(b) shows a longitudinal section of the model which consisted of concentric steel and lead nodes as shown.

The 480 watts decay heat was applied uniformly to the cavity walls along a 25.50 inch axial length (equal to the length of two containers without the collars). All heat flow through the cask walls to the environment was assumed to be radial.

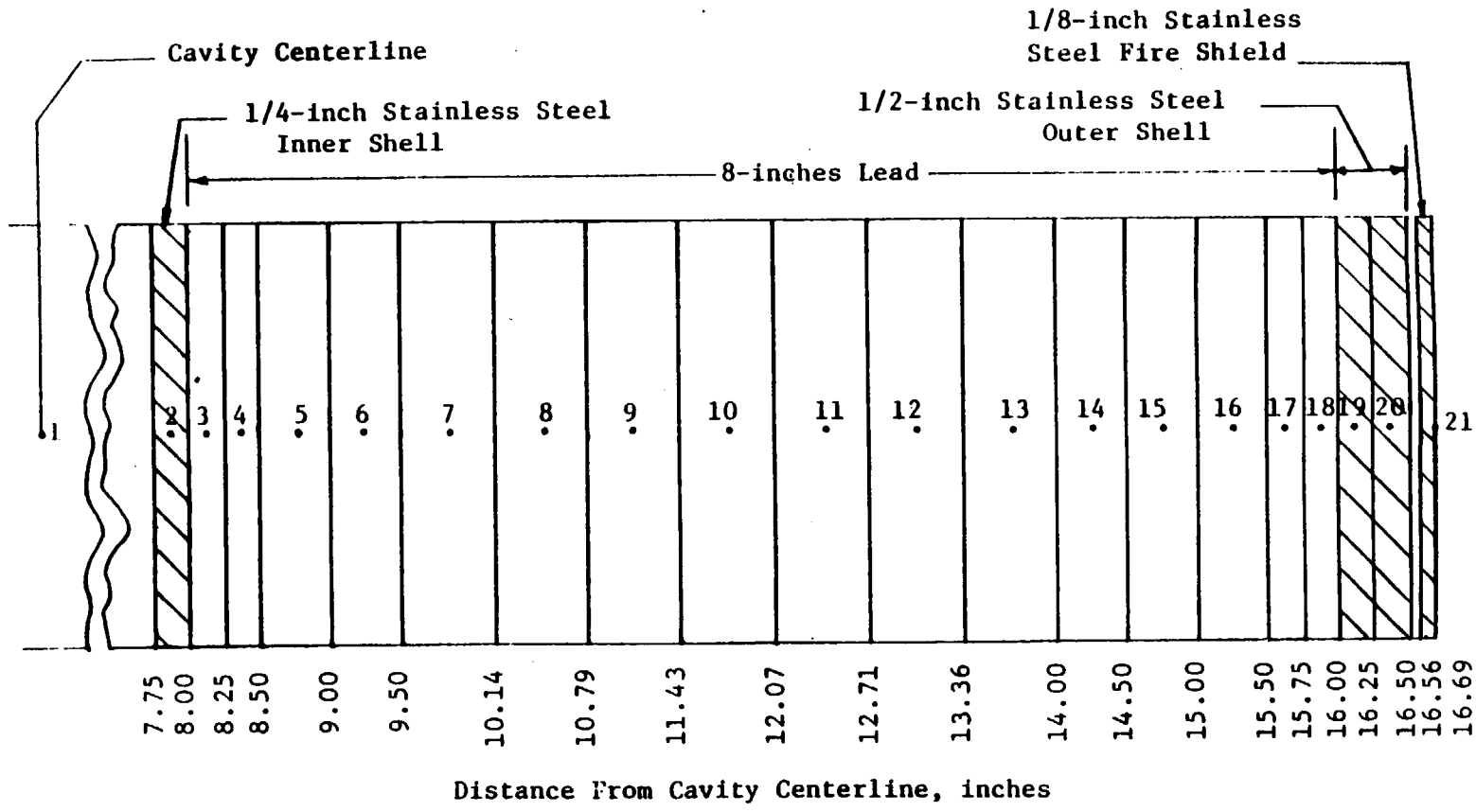

Figure 3.2(b) Thermal Model of Cask

This is conservative since the cavity is 54 inches long and the 28.5 inches of cavity length as well as the cask ends are neglected for heat transfer from the contents through the cask walls and to the environment.

The solar heat load, from Section 3.4.2.1(a) was taken as 80.9 BTU/hr-ft^2 and the surface emissivity was taken as 0.5 The ambient temperature was taken as 100 F, the temperature permitted for the start of the hypothetical fire accident. With this ambient temperature the cask cavity liner temperature was calculated to be 227 F. If the ambient were 130 F, the cavity liner temperature would be approximately 30 F greater or 257 F.

The model for determining the temperature of the containers within the baskets is shown in Figure 3.2(c). The model considered radiation and free air convection heat transfer between the containers and the liner. Heat transfer by convection from the containers to the cavity liner was expressed by

$$Q = h_c A_c (T_c - T_w)$$

where

h_c = heat transfer coefficient

A_c = heat transfer area

T_c = container temperature

T_w = cavity liner temperature.

The heat transfer coefficient, h_c, was defined by:

$$H_c = 0.29 \left(\frac{T_c - T_w}{L} \right)^{0.25} \qquad \text{(Reference 8)}$$

The equation is part of the TRUMP program. Radiation between the container, and between the containers and the cavity wall was accounted for using the procedure and data presented below in Section 3.5.4.2(a), (pages 3.34 to 3.36).

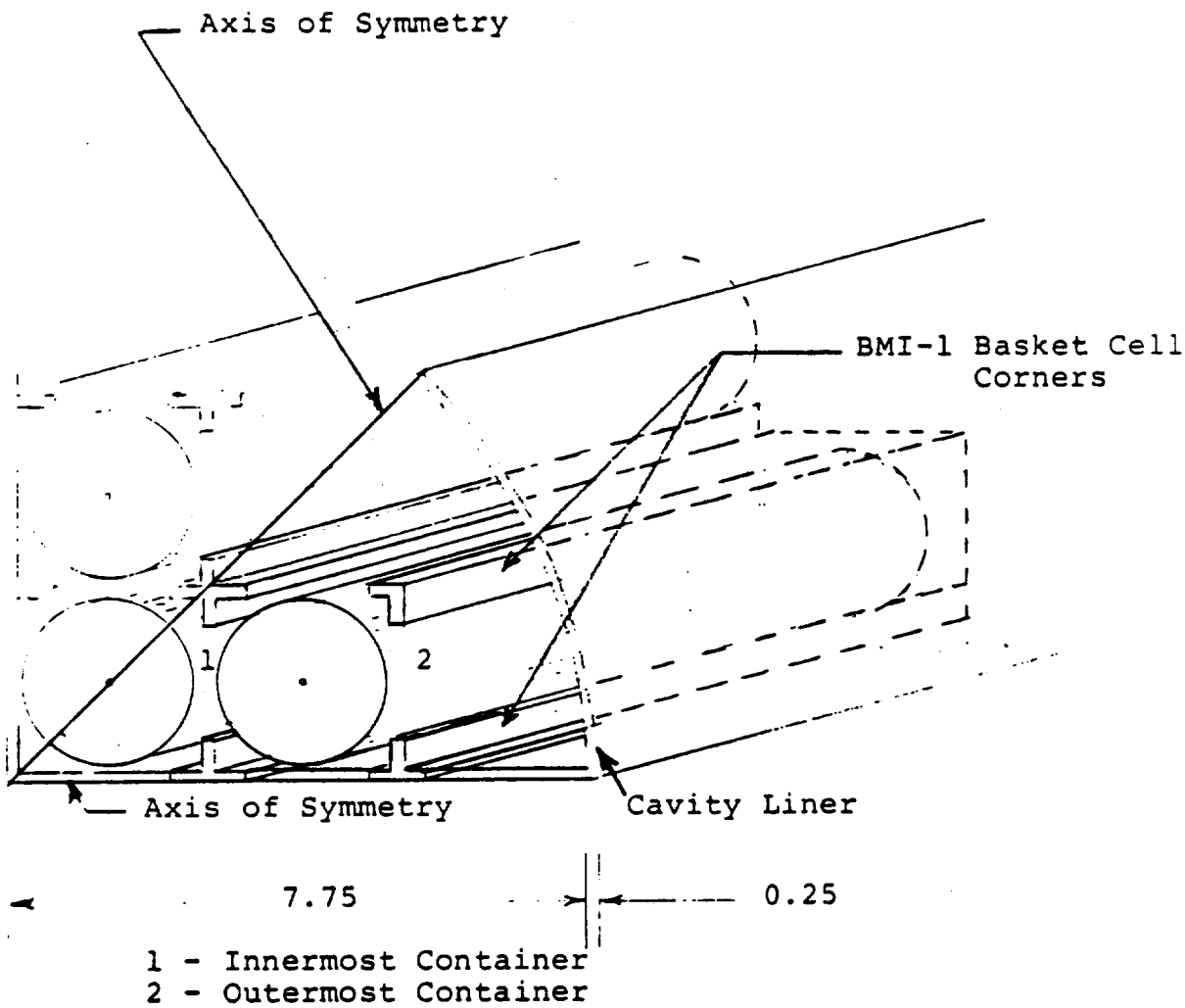

Figure 3.2(c) Sketch of Thermal Model of Union Carbide Process Uranium Oxide Containers in BMI-1 Basket

The analyses indicate that the following temperatures exist:

Ambient:	100F	130F
Cavity wall:	227F	257F
Outer most containers:	253F	283F
Inner most containers:	305F	335F

3.4.2.5 Union Carbide Target U^{235} Special Form Capsules

The maximum heat that the aggregate of up to twenty-four special form capsules shipped may generate is 1500 watts. However, the amount of decay heat within the capsules may vary. Thus, analyses were performed to show that in the limit case, a single capsule could be shipped in which the total decay heat of 1500 watts is concentrated.

The surface temperature of the cask and capsule during normal transportation was determined by analysis using the TRUMP computer program. The cavity liner temperature was obtained from an analysis using the model shown in Figure 3.2(b). It was assumed that the 1500 watts of heat would be rejected by the cask over only 18 inches of axial length, the same as the length of the special form capsule. This assumption made for convenience is very conservative and will result in higher cask temperatures than if credit were taken for "smearing" the heat over the full 54 inches of the cask cavity plus the ends. The analyses show that for a 100 F ambient temperature, the 1500 watt decay heat applied over 18-inches of the cask length would result in a cavity liner temperature of 398 F. For a 130 F ambient temperature, the liner temperature would be about 428 F.

The temperature of the special form capsule and the basket was determined using the analytical model shown in Figure 3.2(d).

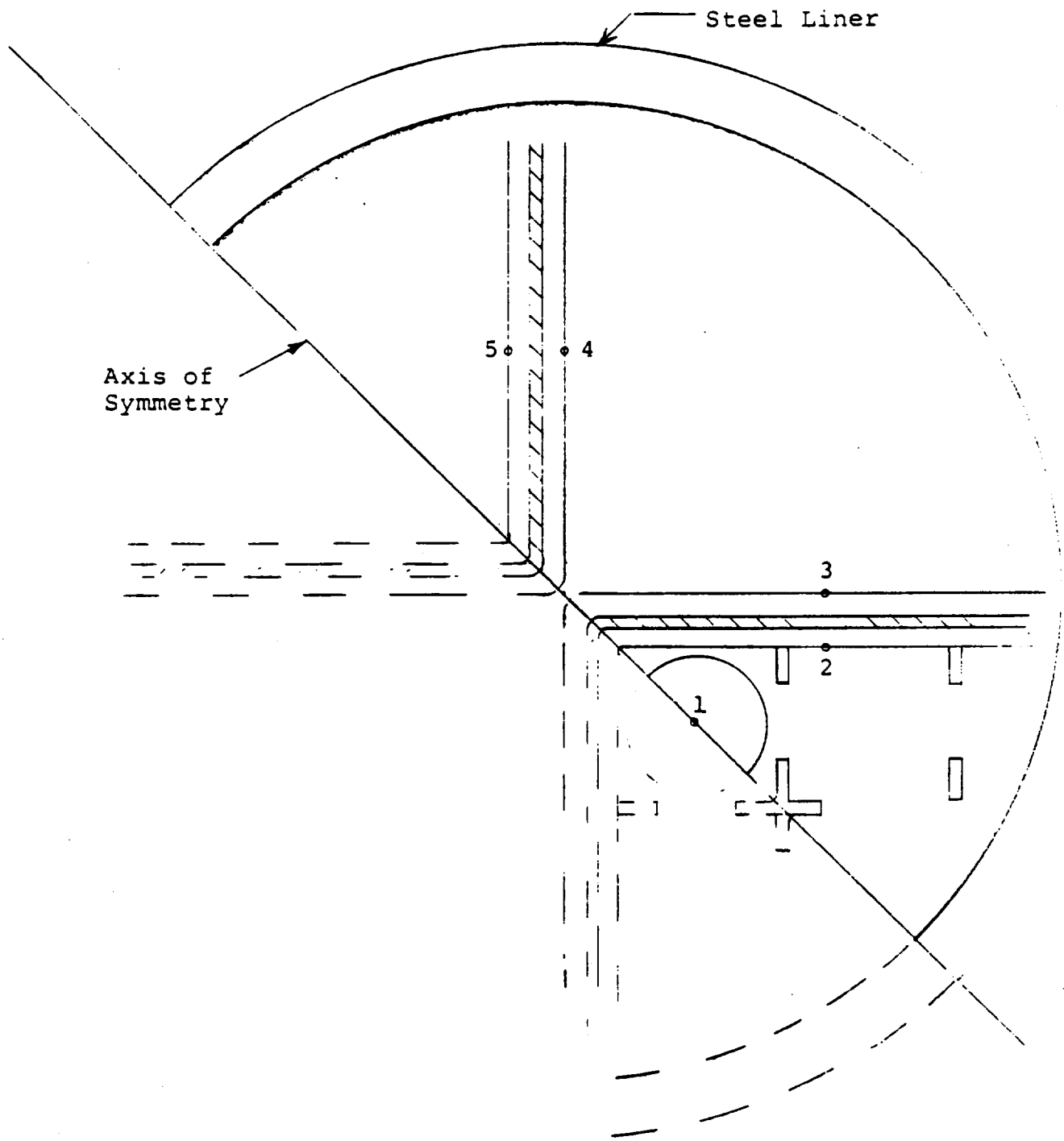

Figure 3.2(d) Analytical Thermal Model of Union Carbide Target U^{235} Special Form Capsule in BMI-1 Cask

The capsule is assumed located in one of the four innermost basket positions. This assumption will result in the highest capsule and basket temperatures. The capsule is centered in the basket cell by an open structure similar to that shown in Figure 3.2(e). This open structure will hold the capsule in place while permitting free radiation and convection heat transfer. The model is two dimensional, i.e., heat flow is considered radially and tangentially (angularly) within the cavity and basket but not axially. Thus, the entire 1500 watts is assumed to be transferred to the cask cavity, through the walls and to the environment within the 18-inch axial dimension of the capsule. This is very conservative since it neglects the axial distribution of heat within the cavity and basket which will significantly decrease the capsule temperature.

Because of symmetry of the cask cavity, only one-half of the cavity cross section was modeled. Natural convection heat transfer within enclosed spaces, especially between Nodes 2 and 3 and between Nodes 4 and 5 is conduction controlled. Nodes 2 and 3, and 4 and 5 form sandwiches around the boral poison plates. The resistance to heat flow through the boral was considered small compared to the interface conductance between the sandwich faces (Nodes 2 and 3 for example) and the boral plate. Therefore, the boral was not modeled. Rather an interface conductance for two 0.010 inch thick (assumed) air gaps (between the stainless steel plates and the boral) was used between the sandwich faces. These values are represented by the expression

$$h_c = k/x$$

where

k = conductivity of air

x = gap thickness.

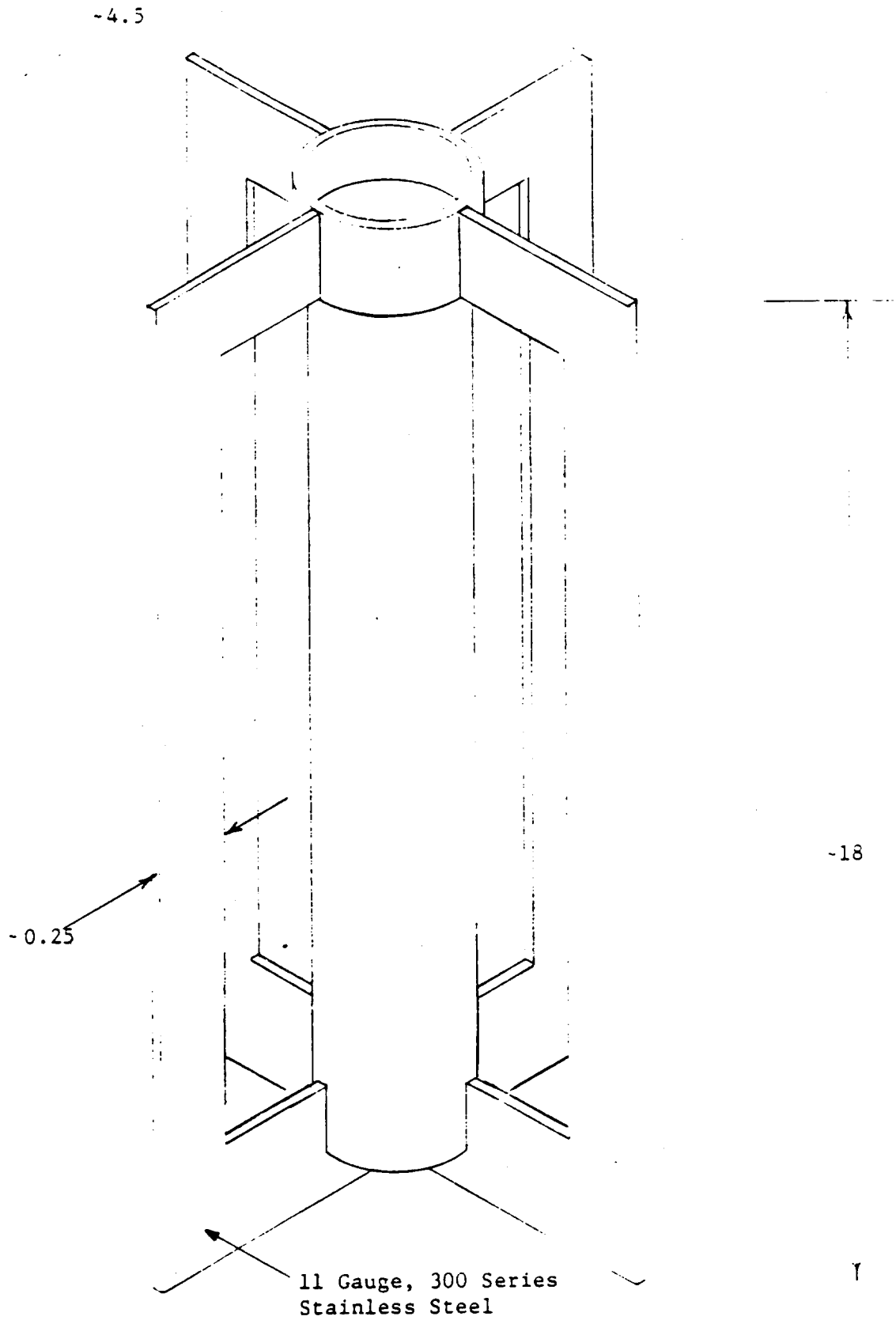

Figure 3.2(e) Sketch of Typical Rack for Supporting Union Carbide U^{235} Special Form Capsule in BMI-1 Basket.

Rev. B. 8-1-80

For radiation heat transfer between the sandwich plates and the cavity liner, the plates and liner were treated as parallel planes, view factor = 1.0. For radiation between the two perpendicular sandwich plates, the view factors for perpendicular planes was used (0.39).

The results indicate that the maximum capsule temperature for normal transportation (130 F) will be 1290 F. This is well below the 1475 F temperature which the capsule must be able to withstand in order to be certified as a special form capsule.

3.4.3 Minimum Temperatures

From Section 3.4.2.1(c), the minimum water temperature is 192.9 - 4.3 = 188.6 F for an ambient temperature (T_a) of 100 F and a decay heat load (Q) of 3,480 Btu/hr. With no solar load, the water temperature is 180 F. For other values of T_a and Q, the water temperature (T) is approximately:

$$T = (180 - 100)\left(\frac{Q}{3,480}\right) + T_a \quad .$$

The water will freeze when T = 32 F, or T_a = 32 - Q/43.5. The water will not freeze at an ambient temperature of T_a = -20 F if the decay heat is greater than Q = 2,260 Btu/hr = 0.662 kw. When these conditions are satisfied, no antifreeze is needed in the water.

In later shipments it is expected that the temperature drop across the cask wall will decrease due to settling of the lead and closing of the air gap between the lead and outer steel shell. In this case, the water temperature may decrease from 180 F to about 160 F under normal conditions. Thus, in later shipments the decay heat will have to be over Q = 0.88 kw to prevent freezing at T_a = -20 F. Provisions will be made to cover the cask with a canvas blanket (which will decrease heat transfer from the outer surface) when ambient temperatures and cask internal temperatures indicate the possibility of freezing.

3.4.4 Maximum Internal Pressures

The design pressure of this cask is 100 psig so that the maximum permissible operating pressure is 50 psig. The maximum operating temperature (230 F) is 68 F below the boiling point (298 F) at the maximum permissible operating pressure.

3.5 Hypothetical Accident Thermal Evaluation

The thermal analysis presented in this section examines the thermal response, and associated effects, of the modified BMI-1 cask when subjected to the environmental fire condition outlined in Appendix B of 10-CFR-71. The fire is defined as a radiant thermal source having a temperature of 1,475 F lasting for 30 minutes. In addition, the "standard fire" is defined to have an effective source emissivity of 0.9, and the thermal absorptivity of the exposed cask surface is defined to be 0.8.

3.5.1 Thermal Model

The thermal transient analysis was carried out using the THT-D heat-transfer code (a generalized heat-transfer program available at Battelle). A cylindrical section, representative of the center region of the BMI-1 cask, was analyzed. Figure 3.3 illustrates the thermal model and THT-D node identification.

The primary modification to the BMI-1 cask, which is directed at fire survival, is the addition of a 1/8-inch-thick outer stainless steel shell (a thermal buffer shell) which encapsulates the existing 1/2-inch steel outer shell. The planned use of evenly spaced weld spots, 1/16-inch high, will assure an air gap between buffer shell and original outer shell. This air gap will impede the thermal pulse resulting from the hypothetical fire. A constant 0.060-inch air gap was employed in the transient calculations although it can be shown that a 1/8 - 3/16-inch air gap would exist due to differences in thermal expansions during the fire period.

FIGURE WITHHELD UNDER 10 CFR 2.390

FIGURE 3.3. THERMAL MODEL EMPLOYED FOR BMI-1 FIRE THERMAL ANALYSIS

3.5.2 Package Conditions and Environment

The starting temperatures (at start of the 30-minute fire) of the cask system, shown in Figure 3.4, were calculated for conditions corresponding to a 130 F day and a cask thermal load of 1.5 kw_t. The correlation of analytics with experimental data is shown in Figure 3.5, where the variation of cask outer surface temperature is shown as a function of thermal load and environmental temperature. The experimental point, measured for the BMI-1 cask without an outer shell, shows a measured outer shell temperature of 130 F on a 70 F day for a 1.4 kw_t thermal load. The calculated result is 133 F on a 70 F day. The external area change due to the addition of a 1/8-inch fire shell can be considered negligible. In addition, the experimental data for the 1.4 kw_t thermal load can be scaled to calculate an inner liner temperature of 227 F for the conditions of a 130 F day with a thermal load of 1.5 kw_t. Therefore, normal shipment with the contents contained in water will not result in any pressurization problems if the 1.5 kw_t heat load is not exceeded. The data contained in Figure 3.4 and 3.5 can be readily employed to assess other ambient and thermal load conditions.

For conservatism, the thermal capacitance of material(s) within the cask internal cavity was neglected, or an empty cavity was assumed for the thermal transient calculations.

Paragraph deleted

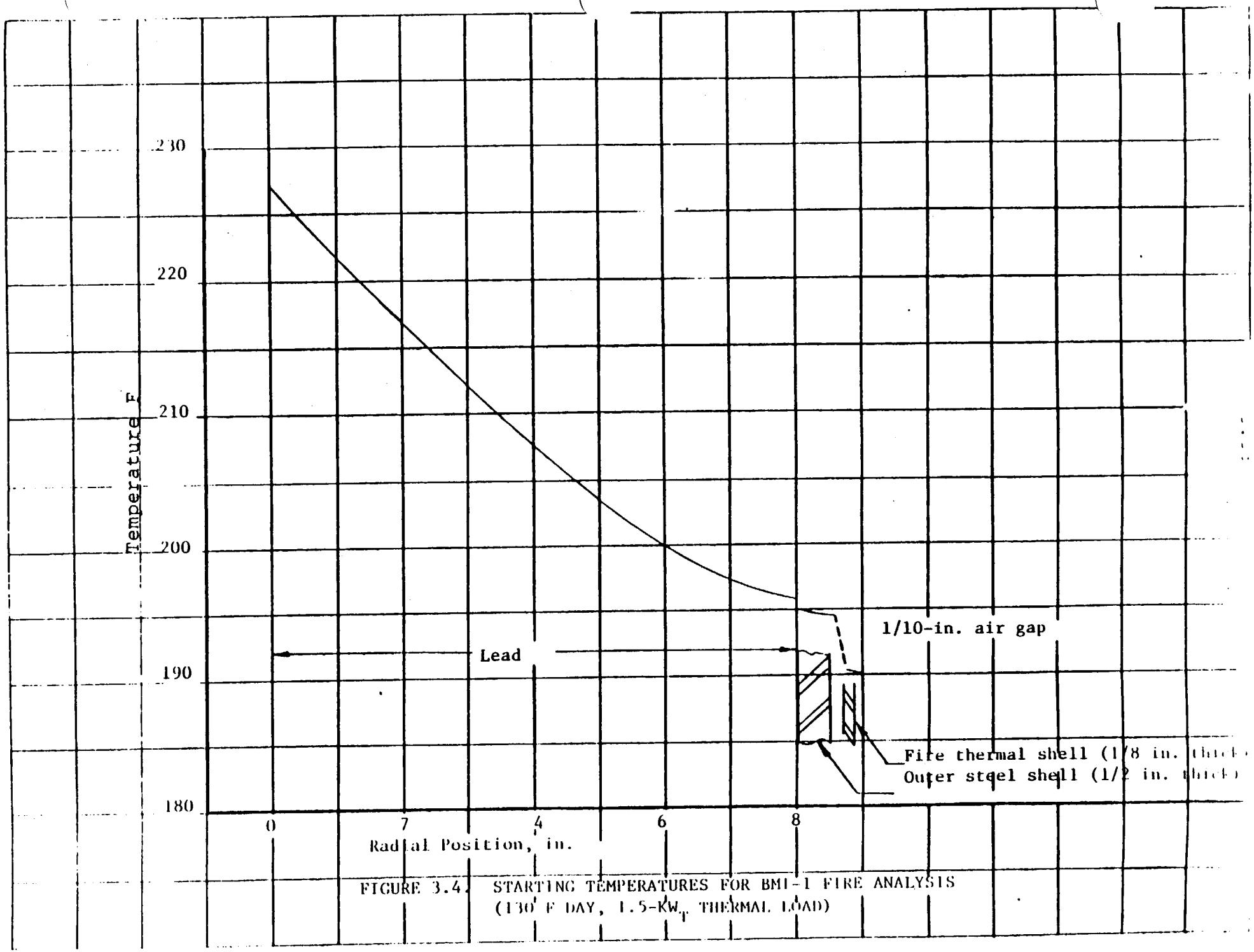

FIGURE 3.4. STARTING TEMPERATURES FOR BMI-1 FIRE ANALYSIS
(130° F DAY, 1.5-KW_T THERMAL LOAD)

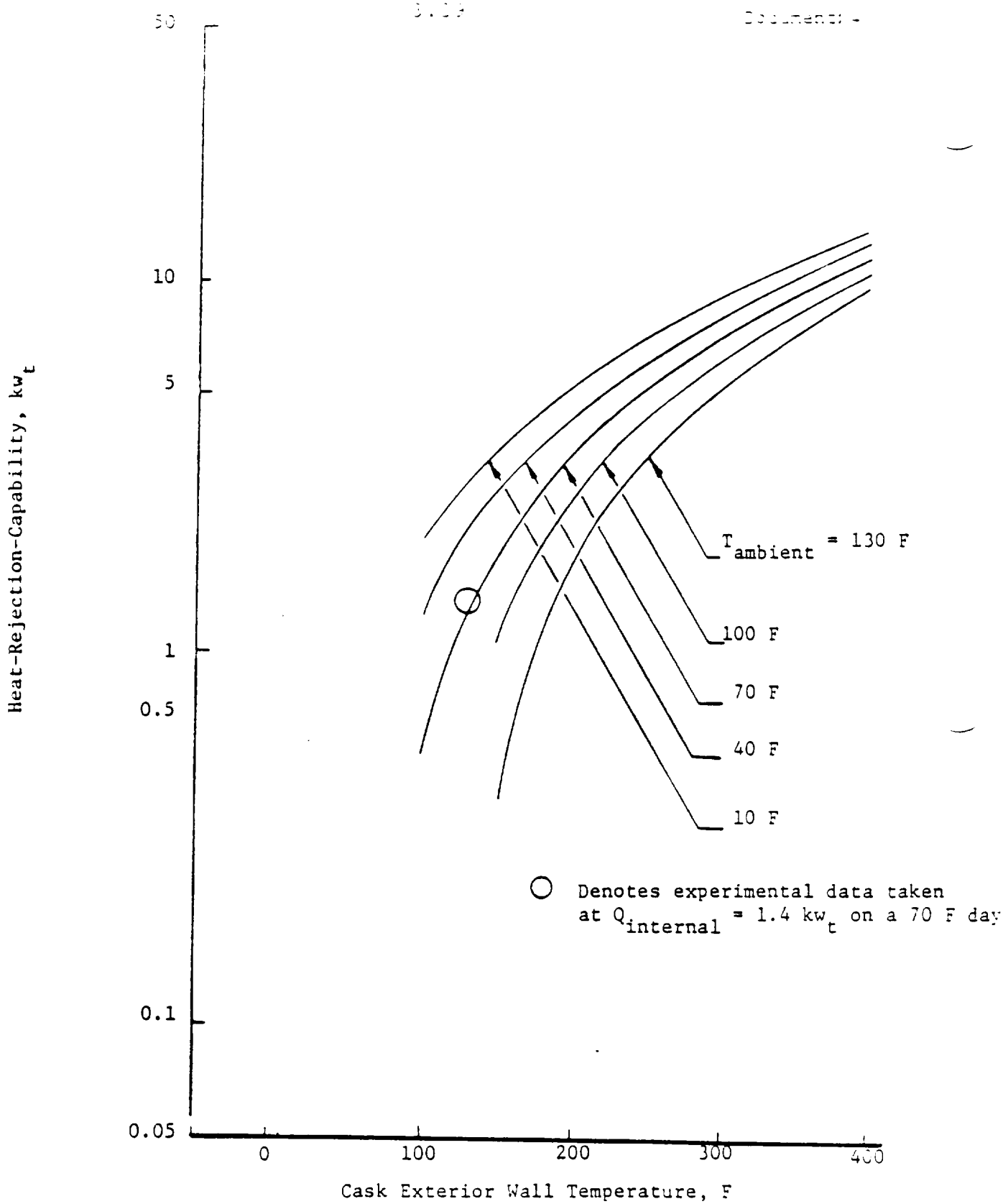

FIGURE 3.5. CALCULATED HEAT-REJECTION CAPABILITY VERSUS EXTERIOR WALL TEMPERATURE AND AMBIENT TEMPERATURE FOR BMI-1

3.5.3 Package Temperatures

The calculated thermal history of selective nodes (see Figure 3.3 for identification) is shown in Figure 3.6. The 1/8-inch outer shell, represented by Node 124 (a shell surface node), has little thermal capacitance and, therefore, responds very rapidly to the fire pulse. The outer shell, 1/2 inch thick, follows in succession, and since it also has only a nominal thermal capacitance, results in the closure of the internal air gap (Node 118). Commencement of lead melting is calculated to be at 16 minutes and the absorption of heat via latent heat capacity causes a reversal in the temperature response (see Figure 3.6) for a short time period. As the melt front travels inward, the outer shells then continue their temperature rise. The temperature reversal, and retardation, mentioned above are also the result of the thermal capacitance of the lead shield which has now become thermally coupled to the outer shell due to the lead-shrinkage gap (Node 118) being closed.

The "melt-front" boundary is shown in Figure 3.7, as a function of radial position and time.

3.5.4 Evaluation of Package Performance for the Hypothetical Accident Thermal Condition

3.5.4.1 Lead Melt

The cylindrical region of the BMI-1 cask was analyzed in detail to assess the potential for lead melting during a postulated hypothetical fire. The analysis assumed temperatures at commencement of fire corresponding to normal operation on a 130 F day with a 1.5 kw_t internal heat load.

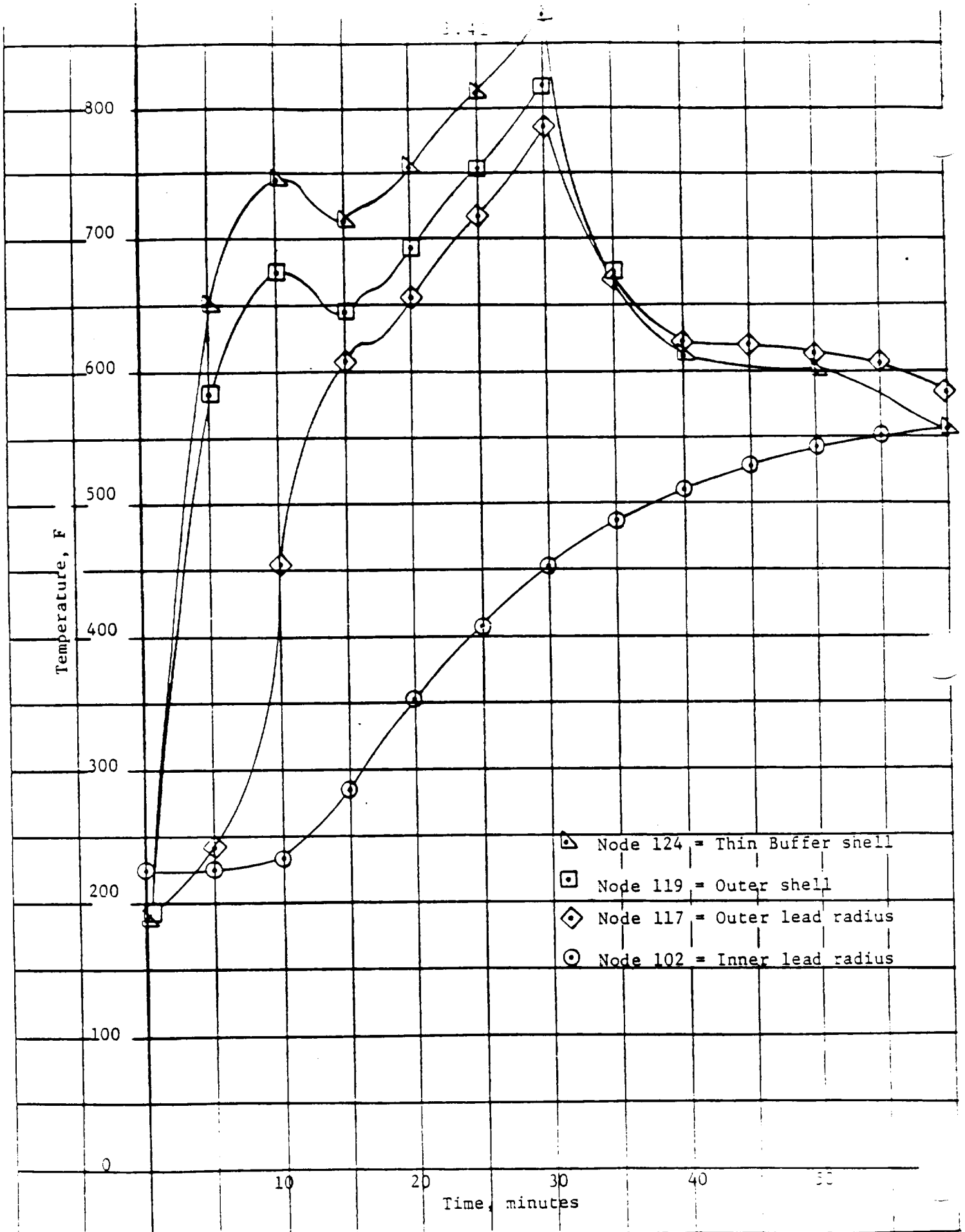

FIGURE 3.6. CALCULATED THERMAL HISTORY FOR THE MODIFIED BMI-1

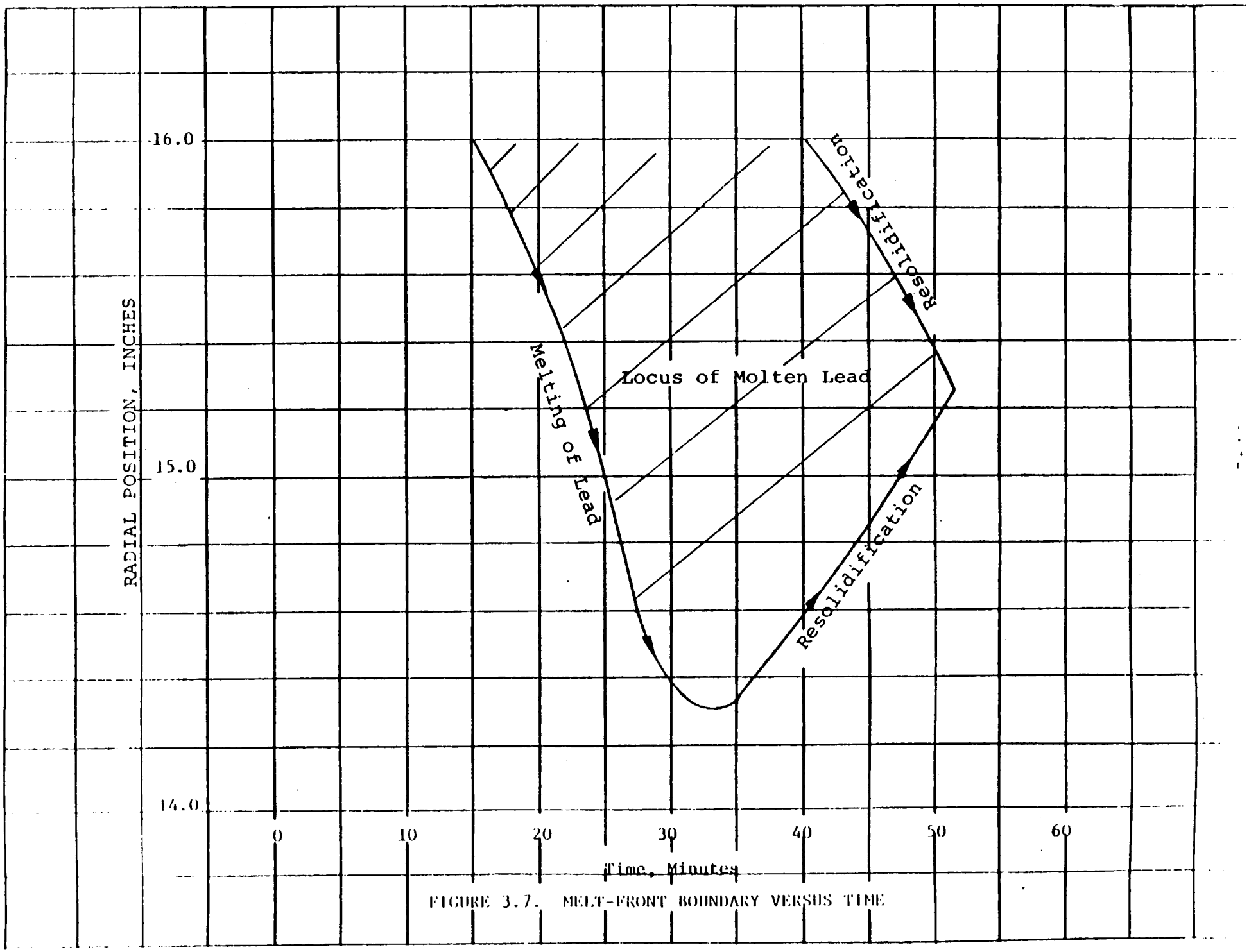

FIGURE 3.7. MELT-FRONT BOUNDARY VERSUS TIME

This analysis considers heat transfer through the cylindrical wall of the cask. This is the most severe thermal condition which could exist since the cover lid, corners, and bottom of the cask have sufficient thermal protection in the form of thick structural plates (i.e., 1-1/4-inch lid plate), skid I-beams, and corner lead-expansion voids. These structures provide a significant thermal capacitance and/or resistance.

The results of the thermal transient analysis indicate lead melt, within the outer regions of the lead shield.

The outer radius of the lead is 16.0 inches, and melting is calculated to proceed inward to a radial depth of 1.65 inches. Lead melting does not occur at the inner regions. Resolidification begins at about 33 minutes within the lead interior, followed by resolidification at the outer radius starting at 40 minutes. The results of these transient calculations indicate a maximum potential lead melt of 34 volume percent of the total lead if the cask is at the starting temperatures used in the calculation. Since expansion volume is provided for by shrinkage from the original casting, the expansion void needs only to accomodate the 3.8 percent increase in volume of the lead that melts. The built-in expansion void (752 inches^3) is more than sufficient to accommodate the excess volume of molten lead (574 inches^3), therefore, no pressure will be exerted on the wall of the cask. Also, no lead is lost. The adequacy of lead shielding after resolidification is discussed in the shielding section.

The lid, bottom, and corner volumes were not analyzed specifically since it is felt that the analysis presented above contains sufficient conservatism to permit extrapolation to those cask regions. For example, the lid cover is 1-1/8 inches thick and the corners at the loading end have 3/4-inch steel plates, respectively. The thermal capacitance of these plates, along with the internal air gaps (1/4 inch in the cover and expansion volumes in the corners) will very likely result in zero lead

melt for those regions. The bottom of the cask also has corner-expansion volumes, and a 1-inch base plate. The base plate is furthermore thermal radiatively shielded by the I-beams employed in the skid. Previous calculations (i.e., NRBK-43) on similar cask systems have shown that the I-beam structure provides sufficient shielding from the fire to preclude, or minimize significantly, lead melting. Therefore, the bare cylindrical sides are the most susceptible to melting from a hypothetical fire, and were analyzed in detail. Based on the above analysis, the maximum canister flange temperature reached during/after a fire test is estimated to be less than 600 F.

3.5.4.2 Maximum Contents Temperature

(a) BRR/MTR Fuel, Loss of Coolant

The fuel element baskets in this cask contain two solid sheets of steel (neutron poison) which divide the baskets into quadrants containing three elements each. Since no heat is transferred between quadrants, the solid sheets have no effect on heat transfer. The three fuel elements in each quadrant are held in place by means of vertical steel strips on the corners of the elements. These strips partially obstruct radiation heat transfer, but have no effect on conduction or convection heat transfer.

Figure 3.8 is a sketch of one quadrant of the basket. Heat is transferred from Element 2 to Element 1 by radiation and conduction in air. Heat is transferred from Element 1 to the inner cask wall by radiation and convection. Analytically this is expressed as:

$$Q_{21} = 0.173\ F_{21}A_2 \left[\left(\frac{T_2}{100}\right)^4 - \left(\frac{T_1}{100}\right)^4 \right] + \frac{kA_2}{t}\,(T_2 - T_1) \qquad (6)$$

$$Q_{1c} = 0.173\ F_{1c}A_1' \left[\left(\frac{T_1}{100}\right)^4 - \left(\frac{T_c}{100}\right)^4 \right] + h_c A_1\ (T_1 - T_c) \quad . \quad (7)$$

As discussed later, conduction in the aluminum elements smoothes out the axial temperature distribution so that the axial power peaking factor does not have to be included in Q_{21} or Q_{1c}. From Section 3.1.2(a), the total decay heat per element is 145 Btu/hr. Thus, Q_{21} = 145/2 = 72.5 Btu/hr and Q_{1c} = 145 x 3/2 = 218 Btu/hr. The heat transfer coefficient h_c is:

$$h_c = \frac{0.071}{\left(\frac{L}{t}\right)^{\frac{1}{9}}} \left[\frac{\rho^2 k^2 g \beta c}{\mu} \right]^{\frac{1}{3}} (T_1 - T_c)^{\frac{1}{3}} \quad . \quad \text{(McAdams}^{(4)}\text{ p 181)}$$

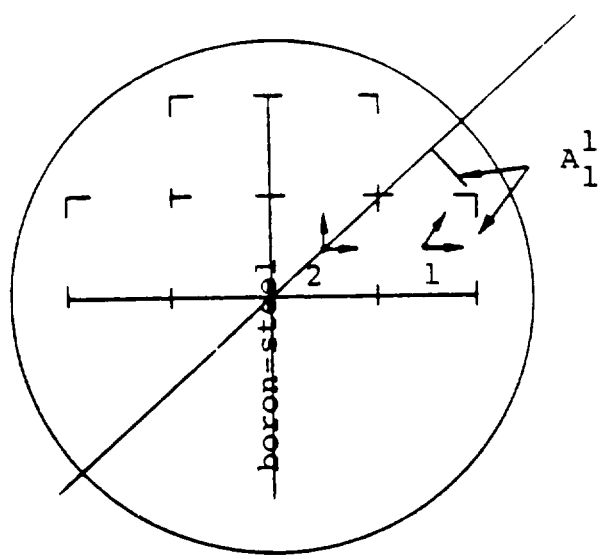

FIGURE 3.8. SKETCH OF FUEL BASKET

The numerical data needed to calculate h_c are:

$$T_{av} = 390 \text{ F}$$

$$L = 25 \text{ inches}$$

$$t = D_o/2 = 1.38 \text{ inches}$$

$$\left[\frac{\rho^2 k^2 g\beta c}{\mu} \right]^{\frac{1}{3}} = 1.25$$

and

$$h_c = 0.0643 \ (T_1 - T_c)^{\frac{1}{3}} \quad .$$

Neglecting the effect of the corner strips, the radiation interchange factors F_{12} and F_{2c} are:

$$F_{21} = (2/\varepsilon_{Al} - 1)^{-1} = (2/0.15 - 1)^{-1} = 0.081$$

$$F_{1c} = (1/\varepsilon_{Al} + 1/\varepsilon_{Fe} - 1)^{-1} = (1/0.15 + 1/0.5 - 1)^{-1}$$

$$= 0.131 \quad .$$

For two steel surfaces, F = 0.333.

Now, consider the effect of the corner strips on radiation heat transfer. Assume that the surfaces A_1, A_2, and A_3 are parallel and that heat is transferred by radiation from A_1 to A_2 to A_3. Then:

$$Q_{12} = \sigma F_{12} A_1 (T_1^4 - T_2^4)$$

$$Q_{23} = \sigma F_{23} A_2 (T_2^4 - T_3^4)$$

and

$$\frac{Q_{12}}{\sigma F_{12} A_1} + \frac{Q_{23}}{\sigma F_{23} A_2} = T_1^4 - T_3^4 \quad .$$

Since $Q_{12} = Q_{23} = Q_{13}$ and $A_1 = A_2 = A_3$,

$$Q_{13} = \sigma \left[\frac{F_{12} F_{23}}{F_{12} + F_{23}} \right] A_1 (T_1^4 - T_3^4) \quad .$$

Thus, for the portion of the area between Elements 1 and 2 where the steel strips obstruct radiation heat transfer:

$$F_{21} = \frac{0.131 \times 0.131}{0.131 + 0.131} = 0.065$$

For the obstructed area between Element 2 and the cask wall:

$$F_{1c} = \frac{0.131 \times 0.333}{0.131 + 0.333} = 0.0935 \quad .$$

The steel corner strips obstruct one inch of the three inch element width. Averaging the radiation factors over the element width:

$$F_{21} = \frac{1(0.065) + 2(0.081)}{3} = 0.076 \quad ,$$

and

$$F_{1c} = \frac{1(0.0935) + 2(0.131)}{3} = 0.118 \quad .$$

The assembled numerical data needed to calculate T_2 and T_1 are:

$Q_{21} = 72.5$ Btu/hr $\qquad t = \frac{0.75}{12} = 0.0625$ ft

$Q_{1c} = 218$ Btu/hr $\qquad A_2 = 3 \times 25/144 = 0.52$ ft^2

$F_{21} = 0.076$ $\qquad A_1 = 2A_2 = 1.04$ ft^2

$F_{1c} = 0.118$ $\qquad A_1 = (1 + 1/\sqrt{2})\ A_2 = 0.89$ ft^2

$T_c = 186$ F $= 646$ R $\qquad k = 0.0239$ Btu/hr ft F .

$h_c = 0.0643(T_1 - T_c)^{\frac{1}{3}}$

Using these data, Equations (6) and (7) become:

$$72.5 = 0.00683 \left[\left(\frac{T_2}{100}\right)^4 - \left(\frac{T_1}{100}\right)^4 \right] + 0.199(T_2 - T_1) \qquad (6)$$

$$218 = 0.01815 \left[\left(\frac{T_1}{100}\right)^4 - 1{,}732 \right] + 0.067(T_1 - 646)^{4/3} \qquad (7)$$

The solutions to these equations are $T_1 = 461$ F and $T_2 = 615$ F. Thus, the maximum element temperature during loss of coolant is 615 F.

In the calculations above, the axial power peaking factor has been neglected since the aluminum in the fuel elements effectively evens out the axial temperature distribution. For a triangular power distribution with an axial peaking factor of 1.4, the fraction $(1.4-1)/4 = 0.1$ of the power is generated at a power greater than average. The temperature drop required to conduct this 10 per cent excess heat from the center to the end of the element is approximately:

$$\Delta T = \frac{0.10\left(\frac{Q}{2}\right)L}{kA}$$

where

$$Q = 145 \text{ Btu/hr}$$

$$L = 25/2 = 12.5 \text{ inches}$$

$$k = 135 (\text{aluminum at } 600 \text{ F})$$

$$A = 2.55 \text{ inches}^2 \quad .$$

$$\Delta T = \frac{(0.10)(72.5)(12.5)(12)}{(135)(2.55)} = 3.16 \text{ F} \quad .$$

Thus, the axial peaking factor increases the element temperature by 3.2 F.

It has also been assumed in the work above that the fuel elements are isothermal. The temperature drops across the elements themselves depend on the orientation of the fuel elements in the basket. In the worst case, the temperature drop would be about 15 F.

In conclusion, considering all the factors discussed above, the maximum fuel element temperature during loss-of-coolant will be $T_2 = 615 + 3 + 15 = 633$ F. This is a safe temperature for aluminum plate-type fuel elements.

Steam produced in the cask cavity during a fire is vented through a 1/16-inch-thick filter with a flow area of 20 inches^2. According to data obtained for pressure differentials (ΔP) up to about 20 psi, the flow capacities of these filters are $W/A = 26.5\ \Delta P + 50$ ft^3/min per ft^2 of filter area. Using this equation to extrapolate to $\Delta P = 75$ psi, the flow capacity is $W = 283$ ft^3/min. (The pop-off value is set at $\Delta P = 75$ psi.) At 89.7 psia, 283 pounds of water forms 1,382 feet^3 of steam. Thus, the cavity can be vented in $t = 1{,}382/283 = 4.9$ minutes. Ten minutes is considered a reasonable time to empty the cask. Thus, a 100 per cent safety factor in the design has been allowed, which is more than adequate to compensate for the possibility that the extrapolated filter-flow-capacity data is not accurate at $\Delta P = 75$ psi.

(b) Fermi Fuel, Loss of Coolant

(Paragraphs deleted through page 3.51)

Material deleted

(c) EPRI Crack Arrest Capsules

It was shown in the September 8, 1969 SAR Amendment, that for a full heat load of 1,500 watts, and starting into the hypothetical fire accident from condition for a 130 F ambient temperature, the maximum cask cavity wall temperature during the incident is about 560 F. Conservatively it is assumed that the Δt from the cask wall to the capsule is the same as for the steady state condition. Then the maximum capsule temperature during the hypothetical accident is 560 + (332 - 132) = 760 F. This is well below the melting temperatures for all the materials in the capsule. The maximum temperature of 760 F is a conservative value for the following reasons:

(1) The starting conditions are for an ambient temperature of 130 F. However, a 100 F ambient is allowed for determining starting conditions.

(2) The heat capacity of the capsule is neglected which will lower the maximum temperature in reality.

(3) The Δt from the capsule to the cask cavity wall is assumed to be a constant over the temperature range. In reality, radiation heat transfer will become more dominant at the higher temperatures resulting in lower maximum capsule temperatures.

(d) Union Carbide Process Uranium Oxide Container

The models shown above in Figures 3.2(b) and 3.2(c) were used to determine the temperature of the cask and contents during the hypothetical accident. The hypothetical accident was defined as a radiant heat source having a temperature of 1475 F and an effective emissivity of 0.9. Initially, a thermal transient analysis was performed for the fueled shipping cask (absorptivity = 0.8) to determine cavity liner temperature as a function of time. No solar heat load was included during the 30 minute fire. The resulting temperature/time profile was then used as the boundary condition in the contents/cavity transient thermal simulation.

The results of the analyses, shown in Figure 3.8(a), indicate that the cavity wall of the cask reaches a peak temperature about 1 hour after the start of the hypothetical fire and then cools rapidly. The temperatures of the capsules continue to "coast up", however, peaking about 3 hours after the start of the fire. The maximum temperature of about 586 F is acceptable for the 6061-T6 aluminum alloy from which the containers are made. The structural condition of the container is considered in Section 2.0.

(e) Union Carbide Target U^{235} Special Form Capsule

The models shown above in Figures 3.2(b) and 3.2(d) were used to determine the temperature of the cask and contents during the hypothetical fire accident. The cavity liner temperature/time profile was obtained from thermal analysis of the entire cask and used as the input boundary condition to determine the capsule temperature/time profile. The conditions for the "fire" were as used for analyses of the Union Carbide process oxide containers, Section 3.5.4.2(d).

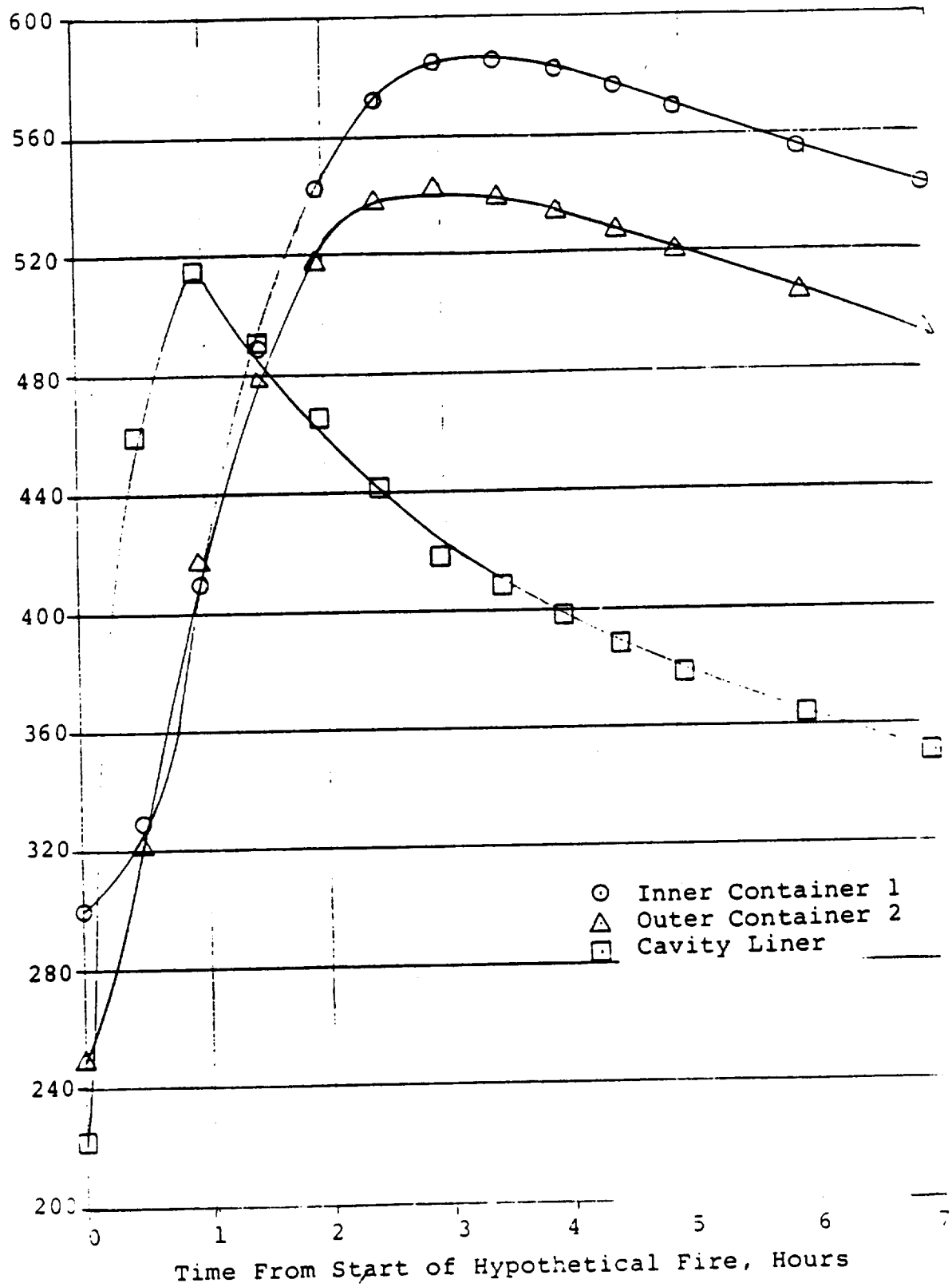

Figure 3.8(a) Calculated Thermal History Union Carbide Process Uranium Oxide Canisters in the Basket of the BMI-1 Cask

The results of the analyses, shown in Figure 3.8(b), indicate that the capsule reaches a maximum temperature of 1325 F about 1 hour after the start of the hypothetical fire. This is well below the temperature of 1475 F which the capsule must withstand in order to be certified as a special form capsule. The stainless steel shells of the basket experience a maximum temperature of 785 F. This is acceptable for stainless steel and is well below the melting temperature of the aluminum matrix of the boral sandwiched between the stainless steel shells. At these temperatures aluminum has sufficient strength to resist "slumping" due to its own weight. Moreover, the stainless boral sandwich is fabricated with stainless pins extending through the boral and welded to the two stainless shells. This reinforcement will prevent "bulging" of the shells due to the elevated temperature and thus also help keep the boral from shifting.

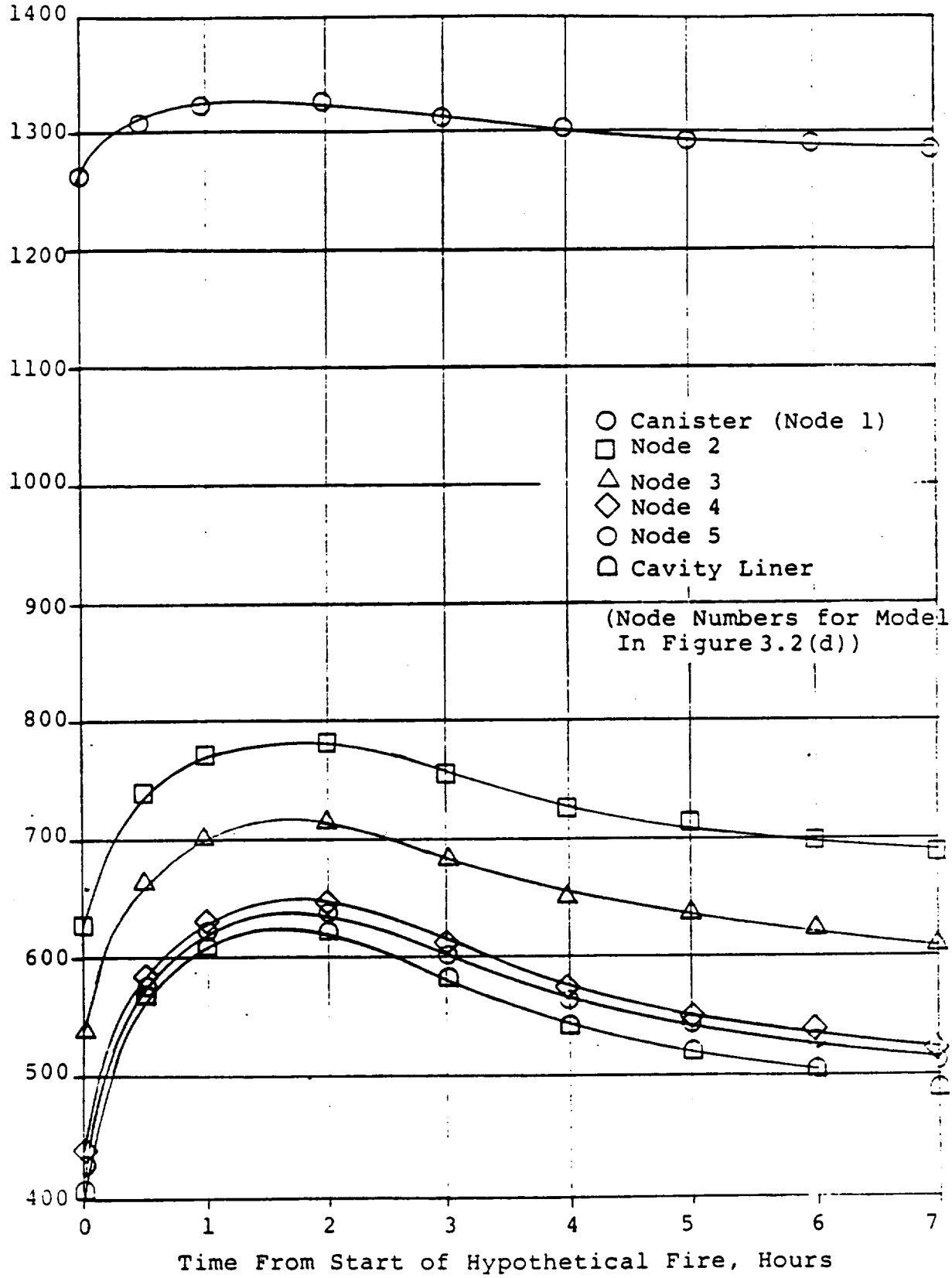

Figure 3.8(b) Calculated Thermal History for a Special Form Capsule with Decay Heat of 1500 Watts in the Innermost Position in the Basket of the BMI-1 Cask

3.6 Appendix

3.6.1 References

(1) J. O. Blomeke and M. F. Todd, "U-235 Fission Product Production as a Function of Flux, Irradiation Time, and Decay Time", ORNL-2127, Part I, Vol 2 (1957).

(2) Nims, J. B., "Generalized Subassembly Decay Heat Curves", APDA Memo P-64-11, January 14, 1964.

(3) L. S. Marks, "Marks' Handbook", McGraw-Hill, Inc. 5th Ed. (1951).

(4) W. H. McAdams, "Heat Transmission", McGraw-Hill, 3rd Ed. (1954).

(5) R. O. Wooton and H. M. Epstein, "Heat Transfer from a Parallel Rod Fuel Element in a Shipping Container", to be published, Battelle Memorial Institute (1963).

(6) McAdams, W. H. p 181, Eq7-9b.

(7) Edwards, A. L., "TRUMP: A Computer Program for Transient and Steady-State Temperature Distributions in Multidimensional Systems", UCRL-14754, Rev. 3., Lawrence Livermore Laboratory, September 1, 1972.

3.6.2 Experimental Tests of Copper Shot

(Section 3.6.2 deleted

3.6.3 Thermal Evaluation - BMI-1 Cask with Eight MURR Spent Fuel Elements

Normal Transport Conditions

1. Maximum Cask Surface Temperature

We follow the BMI-1 SAR, Section 3, Thermal Evaluation. During normal conditions, the cask is water-filled and the ambient temperature T_a [10 CFR 71.71(c)(1)] is 100 °F, or 560°R. The decay heat load is 1.5 kW and the solar load is 0.392 kW for Fermi fuel. These are exactly applicable to MURR fuel.

The following calculation of the cask outside surface temperature T_s due to radiant and convective (air) heat transfer of Q = 1.892 kW = 6,456Btu/hr is from SAR Section 3.4.2.2.

The needed equations are:

$$Q = Q_{radiation} + Q_{convection}$$

$$Q_{rad} = \sigma \varepsilon A \left[\left(\frac{Ts}{100}\right)^4 - \left(\frac{Ta}{100}\right)^4 \right]$$

$$Q_{conv} = h A (T_s - T_a)$$

$$h = 0.19 (T_s - T_a)^{1/3}$$

$$\sigma = 0.173 \frac{Btu/hr}{ft^2 \ (°F/100)^4}$$, the Stefan-Boltzmann constant

$\varepsilon = 0.5$, the emissivity; $A = 49.7\ ft^2$, the cask vertical surface area, conservative because not including cask corner areas from which heat transfer is obscured by air pockets. See SAR Section 3.4.2.1(a), top p. 3.10.

The heat transfer coefficient h formula is from W. H. McAdams, Heat Transmission, McGraw-Hill, Third Edition, p. 173.

The solution for the cask surface temperature is $T_s = 182°F$.

By 10 CFR 71.43(g), no accessible surface of a package in an exclusive use shipment may have a temperature exceeding 180°F. The calculated 182°F is subject to uncertainty because of cask model simplifications and assumptions. We have an experimental basis for concluding that the cask surface will not exceed 170°F.

In October 1984, we placed a 1.5 kW electrical heater inside the GE-700 cask with the lid on. After equilibrium was reached in 24 hours, the maximum cask surface temperature was 126°F when the ambient temperature was 74°F. Using the Q_{rad} and Q_{conv} formulas above, these experimental data let us derive a different heat transfer coefficient formula

$$h = 0.40\,(T_s - T_a)^{1/3}.$$

This formula should be better than McAdams' equation for h above, because it was measured under somewhat forced convection conditions, and was obtained with a cask very much like the BMI-1. The GE-700 cask without overpack is quite similar to the BMI-1 cask which does not use an overpack in transit. Using this h with the BMI-1 cask instead of the McAdams' formula, in a calculation otherwise like that above, gives $T_s = 158°F$. For an emissivity of 0.3, T_s is 164°F. For $\varepsilon = 0.7$, $T_s = 152°F$.

Our QA procedures for spent fuel shipping include measuring the cask outside surface temperature for four hours after loading. The GE-700 cask surface was always initially at about 105°F, the pool water temperature,

and cooled to about 100°F in 75°F ambient. This was true for decay powers in the range 0.35 to 1.1 kW.

We believe our measurements with the dummy electrical 1.5 kW load, and our experience with actual fuel loads, gives confidence that the BMI-1 cask surface temperature will not exceed 180°F. By our QA procedures, we will not ship if the $\Delta T = T_s - T_{amb}$ exceeds 80°F. (T_s = cask surface temperature.)

2. Maximum Fuel Temperature

We assume a worst case of a 180°F cask surface temperature, and want to add to this the calculated temperature rises through the lead (Pb) cask wall, across the cask cavity wall-fuel basket coolant-filled gap, and radially across the fuel.

As described in the SAR, Section 3.4.2.2(b), a temperature rise through the lead wall of 29°F was measured when an electrical heater of 1.4 kW was in the cavity. Scaled to 1.5 kW decay power, this temperature rise is 31°F.

MURR spent fuel is shipped as a cylindrical annulus of height H = 2 ft., inner radius a = 0.30 ft., and outer radius b = 0.55 ft. in a 0.25 inch 304 stainless steel outer cylindrical wall basket with radial 304 walls (0.25 inch and 0.375 inch alternating) between the fuel elements. There is a 0.75 inch gap between the 14 inch O.D. basket and the 15.5 in I.D. cavity.

To calculate ΔT_{gap} across the 0.75 inch of water coolant, we will use h = 100 Btu/hr.ft.^{2}°F. This value of the heat transfer coefficient is used on p. 3.16 of the SAR for Fermi fuel, and there is a reference to McAdams. We have also derived essentially this value following D. R. Pitts and L. E. Sissom, Heat Transfer, McGraw-Hill, Section 8.3.

Using an average radius of (7 in. + 7.75 in.)/(2)(12) = 0.62 ft., Q = 1.5 kW = 5118 Btu/hr, and fuel height 2 ft., we get from the Q_{conv} equation above

$$\Delta T_{gap} = \frac{5118}{(100)(2\ \pi)(.62)(2)} = 7°F$$

To calculate the temperature rise across the fuel ΔT_{fuel}, we solve the heat conduction differential equation for a cylindrical annulus, assuming only radial temperature variation T(r).

$$-\frac{1}{r}\frac{d}{dr}\left(r\frac{dT}{dr}\right) = \frac{Q'''}{k_{fuel}}$$

$$Q''' = \frac{\text{power}}{\text{volume}} = \frac{5118\ \text{Btu/hr}}{\pi(b^2 - a^2)\ H\ ft^3}$$

The solution for the boundary condition of zero heat flow to the inside of the annulus, (dT/dr) = 0 at r = a, is

$$T(r) = T(b) + \frac{Q'''}{4k_{fuel}}\left[b^2 - r^2 + 2a^2 \ln\frac{r}{b}\right]$$

and $\Delta T_{fuel} = T(a) - T(b)$.

k_{fuel} is an effective thermal conductivity through the fuel sideplates and basket walls. These subtend only 12% of the fuel annulus outer area, but metallic conductivities are so high that ΔT_{fuel} is relatively small.

$$k_{6061} = 110.\ \text{Btu/hr. ft.°F}\ ,\ k_{304} = 19\ \text{Btu/hr. ft..°F}$$

$$k_{fuel} = k_{6061}\frac{(16\ \text{sideplates})\ (0.15\ \text{in}/12)}{2\pi\ (0.55)} + k_{304}\frac{(4\ \text{ss walls})\ (0.25\ \text{in} + 0.375\ \text{in})/12)}{2\pi\ (0.55)}$$

$$= 7.5$$

So we get $\Delta T_{fuel} = T(a) - T(b) = 13°F$.

Finally, for the highest fuel temperature T_a at the inside of the annulus, $T_a = 13 + T(b) = 13 + 7 + 31 + 180 + 2 = 233°F$ where a 2°F rise across the stainless steel cask and basket cylindrical walls has been added. This result is well below the fuel cladding blister temperature which is greater than 900°F, and is well below the clad failure temperature. See Fuel Fabrication Specification TRTR-4 for University of Missouri fuel elements.

3. Maximum Cask Internal Pressure
AT 233°F, the vapor pressure of water is 25 psia. This will give 25 psig inside the cask, well below the maximum permissible operating pressure of 50 psig.

Hypothetical Accident Conditions

4. Maximum Accident Conditions
Section 3.5 of the SAR presents an analysis showing that in a "standard" 1475°F fire for 30 minutes, the cask cavity wall will reach about 560°F, or 1020°R. Loss of coolant occurs, so heat transfer between the fuel basket and the cavity wall is by convection of air and radiation. The heat transfer coefficient is given by

$$h = 0.0643\,(T_{basket} - T_{cavity})^{1/3}$$

This equation is given on p. 3.48 of the SAR. It may be derived using the Grashof/Nusselt empirical correlations. See Pitts and Sissom, Heat Transfer, McGraw-Hill, Chapter 8.

The calculation for the basket temperature is similar to that in the Normal Transport Conditions Section 1 above. With basket cylinder area 7.7 ft^2, the solution of

$$5118 \text{ Btu/hr} = (.173)(.5)(7.7)\left[\left(\frac{T_{bas}}{100}\right)^4 - \left(\frac{1020}{100}\right)^4\right] + (.0643)\,(7.7)\,(T_{bas} - 1020)^{4/3}$$

is $T_{bas} = 698°F$.

For the temperature rise across the fuel, consider a worst case that the thermal conductivities of the sideplates and basket walls are half those used above, so $k_{fuel} = (7.5)/2$. Then T(a) - T(b) = 26°F. Thus, the maximum fuel temperature in a hypothetical fire accident is 698 + 26 = 724°F, which is well below the clad failure temperature.

5. Maximum Pressure

With loss of coolant, and treating the cavity air as an ideal gas as was done in SAR Section 2.10.5.3, at 612°F the air pressure would be

$$(14.7 \text{ psia}) \left[\frac{612 + 460}{68 + 460}\right] = 30 \text{ psia}$$

This corresponds to 15 psig, well below the maximum operating pressure of 50 psig.

6. Lead Melting

SAR Section 3.5 gives the results of a hypothetical fire accident on the lead wall. The model for this calculation assumed an empty cavity (SAR p.3.37), so the results are not dependent on the type of fuel shipped.

Lead melts from its outer radius to a depth of 1.65 inches, as discussed in Section 3.5.4.1. The most important concepts are that expansion void is provided, no pressure is exerted on the walls of the cask by the melted

lead, the walls remain intact, and no lead is lost. This ensures adequate thermal shielding from the fire, and radiation shielding.

7. Failure of Relief Valve

In a hypothetical fire, the cask cavity inside wall temperature is 560°F, as shown in item 4 above. If there had not been loss of coolant when this temperature was reached, the water vapor pressure in the cavity would be

around 1,000 psi. It is not credible that the lid gasket could contain this high pressure, especially considering high temperature deterioration of the rubber gasket. Therefore failure of the relief valve would not prevent loss of coolant. Coolant expulsion will not result in the release of fission product activity. See the Structural Evaluation analysis for cask containment of radioactivity.

3.6.4 Thermal Evaluation of BMI-1 Cask with Eight MITR Fuel Elements

The total fission product decay heat is defined by the following relation:

$$\frac{P}{P_0}=6.1x10^3[(T_D+10)^{-0.2}-(T_I+T_D+10)^{-0.2}] \quad (1)$$

where P is the element decay heat in watts,

P_0 is the element steady state rate of heat production during the reactor operating time of T_I in days, given by the ratio of reactor power to number of elements present in the core, and,

T_D is the time of decay in days.

Given the worst case of a fuel element being continuously in the MITR core operated 5 days per week until the element has reached its allowed burnup limit of 45% and then allowed to decay for a minimum of 90 days results in a calculated decay heat of 127 watts. Having eight of these elements present in the BMI-1 cask results in a total decay heat load of 1016 watts, well below the 1.5 kW cask limit.

It should be noted that all MITR fuel elements intended for shipment in the BMI-1 cask are operated on a schedule of about 3.75 days per week and decay for a much longer period than 90 days. Of all the fuel elements currently awaiting shipment, the one with the largest decay heat has been calculated to be 19 watts. Even given a 50% error in the above equation from use at large decay times, this decay heat load is not of concern for any scenario involving the BMI-1 cask.

Table 3.3, MIT Spent Fuel Data, gives the decay heat and gamma activity for the MITR fuel elements to be shipped.

Reference: Rust, Nuclear Engineering, Noralson Publishing Company, 1979, p. 244.

Table 3.3 MIT Spent Fuel Data

ELEMENT ID	Beginning U-235 mass (g)	Ending U-235 mass (g)	Date of Removal	No. of days cooled as of 10/1/91	MWH produced	Decay heat (W)	Gamma Activity (Ci)	POST-IRRADIATION U-236 (g)	Pu-239 (g)	Np-237 (g)
MIT-16	506	317.80	2/25/85	2411	78810	11.23	1,291	3.082	5.20E-03	4.02E-03
4M44	445	253.17	8/16/82	3332	88276	8.92	1,026	3.036	5.12E-03	4.44E-03
4M43	445	266.00	10/27/80	3991	81639	6.94	798	2.808	4.74E-03	3.80E-03
4M42	445	249.22	8/20/84	2598	90315	11.61	1,335	3.106	5.24E-03	4.65E-03
4M40	445	255.62	11/17/76	5432	85337	5.19	597	2.935	4.95E-03	4.15E-03
4M39	445	254.26	8/16/82	3332	88276	8.92	1,026	3.036	5.12E-03	4.44E-03
4M38	445	266.28	2/23/81	3872	78225	6.90	794	2.690	4.54E-03	3.48E-03
4M37	445	256.23	6/14/82	3395	86967	8.65	994	2.991	5.05E-03	4.31E-03
4M36	445	267.35	7/7/80	4104	80961	6.68	768	2.784	4.70E-03	3.73E-03
4M35	445	268.59	7/7/80	4104	80961	6.68	768	2.784	4.70E-03	3.73E-03
4M34	445	254.85	6/27/83	3017	88003	9.82	1,129	3.026	5.11E-03	4.41E-03
4M33	445	250.75	8/20/84	2598	88050	11.39	1,309	3.028	5.11E-03	4.42E-03
4M32	445	255.30	12/15/86	1750	87459	16.49	1,896	3.008	5.08E-03	4.36E-03
4M31	445	255.18	6/27/83	3017	88003	9.82	1,129	3.026	5.11E-03	4.41E-03
4M30	445	254.74	2/2/87	1701	89214	17.16	1,973	3.068	5.18E-03	4.53E-03
4M29	445	255.66	5/20/85	2325	86624	12.53	1,441	2.979	5.03E-03	4.27E-03
4M28	445	255.07	2/2/87	1701	88956	17.10	1,966	3.059	5.16E-03	4.51E-03
4M27	445	253.81	12/15/86	1750	88040	16.55	1,903	3.028	5.11E-03	4.41E-03
4M26	445	252.65	7/22/85	2262	87768	13.02	1,497	3.018	5.09E-03	4.39E-03
4M25	445	245.59	7/15/85	2269	92718	13.52	1,554	3.189	5.38E-03	4.90E-03
4M24	445	257.26	11/17/86	1722	84819	16.37	1,882	2.917	4.92E-03	4.10E-03
4M23	445	256.74	12/15/86	1750	86115	16.31	1,875	2.961	5.00E-03	4.22E-03
4M22	445	257.72	4/1/85	2375	84491	12.04	1,384	2.906	4.90E-03	4.07E-03
4M21	445	265.61	9/8/80	4040	81561	6.82	785	2.805	4.73E-03	3.79E-03
4M20	445	245.86	3/29/82	3475	90098	8.69	999	3.098	5.23E-03	4.62E-03
4M19	445	257.15	6/27/83	3017	87958	9.82	1,129	3.025	5.10E-03	4.41E-03
4M18	445	261.30	6/14/82	3395	81206	8.17	940	2.793	4.71E-03	3.76E-03
4M17	445	268.11	7/7/80	4104	80961	6.68	768	2.784	4.70E-03	3.73E-03
4M16	445	255.60	12/15/86	1750	87011	16.43	1,889	2.992	5.05E-03	4.31E-03
4M15	445	255.69	6/14/82	3395	84702	8.46	973	2.913	4.92E-03	4.09E-03

Table 3.3 (Cont.) MIT Spent Fuel Data

4M14	445	256.32	6/27/83	3017	85524	9.58	1,102	2.941	4.96E-03	4.17E-03
4M13	445	269.19	7/7/80	4104	80961	6.68	768	2.784	4.70E-03	3.73E-03
4M12	445	233.39	3/23/87	1655	99198	18.89	2,173	3.411	5.76E-03	5.60E-03
4M11	445	265.46	5/12/80	4160	77483	6.34	729	2.665	4.50E-03	3.42E-03
4M09	445	269.62	5/4/81	3803	81912	7.30	840	2.817	4.75E-03	3.82E-03
4M08	445	266.39	10/27/80	3991	81640	6.94	798	2.808	4.74E-03	3.80E-03
4M06	445	254.96	7/22/85	2263	87506	12.96	1,491	3.009	5.08E-03	4.36E-03
4M05	445	266.77	10/27/80	3991	81640	6.94	798	2.808	4.74E-03	3.80E-03
4M04	445	258.83	8/16/82	3458	82310	8.09	931	2.831	4.78E-03	3.86E-03
4M03	445	268.24	5/12/80	4160	77806	6.37	732	2.676	4.52E-03	3.45E-03
4M02	445	264.36	9/8/80	4040	81561	6.82	785	2.805	4.73E-03	3.79E-03
4M01	445	252.55	6/27/83	3017	88289	9.86	1,134	3.036	5.12E-03	4.44E-03
4M10	445	300.46	6/25/79	4482	60880	4.75	546	2.094	3.53E-03	2.11E-03
MIT-08	506	446.88	9/6/83	2946	22654	3.05	351	0.886	1.49E-03	3.32E-04
MIT-11	506	399.87	2/19/86	2054	41614	7.84	902	1.627	2.75E-03	1.12E-03
MIT-32	506	433.15	7/15/85	2270	28718	5.10	586	1.123	1.90E-03	5.34E-04
MIT-19	506	471.77	10/14/86	1813	13680	3.32	382	0.535	9.03E-04	1.21E-04
MIT-12	506	342.39	5/9/88	1241	68135	18.84	2,167	2.664	4.50E-03	3.01E-03

Document 22

3.6.5 Decay Heat Analysis of HFBR Fuel

The original SAR thermal analysis, Section 3.1.2 (a), specifies that the maximum decay heat for BRR/MTR fuel is 1.02 kw. To determine a shielding source term the decay heat from all sources for a 20 HFBR assembly payload was determined using ORIGEN2. The case considered was based on 60 days operation at 60 MW with a full core of 28 assemblies. The ORIGEN2 output (Reference 22) results were reduced by a factor of 0.71 (20/28) to reflect a 20 HFBR fuel assembly payload on the BMI-1 cask. Table 3.4 summarizes the results of the decay heat analysis. As shown, an average fuel assembly decay time of 470 days results in a decay heat load below the SAR MTR fuel limit of 1.02 kw.

Table 3.4

BMI CASK TOTAL DECAY HEAT
(INCLUDING ALL RADIATION SOURCES)

ORIGEN2 CASE RESULTS FROM: BNLWATT3
BURNUP OF BNL CORE 28 ASSY 377.4 GU PER ASSY 60 MW, 60 DAYS

COOLING TIME DAYS	28 ASSY WATTS	20 ASSY WATTS
200	5.66E+03	4.04E+03
220	4.88E+03	3.49E+03
240	4.25E+03	3.03E+03
260	3.72E+03	2.66E+03
280	3.28E+03	2.35E+03
300	2.95E+03	2.11E+03
320	2.62E+03	1.87E+03
340	2.37E+03	1.69E+03
360	2.15E+03	1.54E+03
380	1.97E+03	1.41E+03
400	1.82E+03	1.30E+03
420	1.69E+03	1.20E+03
440	1.57E+03	1.12E+03
460	1.47E+03	1.05E+03
470	1.42E+03	1.01E+03
480	1.38E+03	9.83E+02
500	1.30E+03	9.26E+02

4. CONTAINMENT

4.1 Containment Boundry

4.1.1 Containment Vessel

For certain uses as defined in Reference 1,(Section 4.4.1) the cask cavity liner provides the containment. For other uses, also defined in Reference 1, an inner containment vessel (canister) is also used to provide containment. These are described in Section 1, including the drawings in the Appendix to Section 1.

4.1.2 Containment Penetration

Penetrations to the cask cavity include the vent/pressure relief line at the top and a drain at the bottom. The specified relief pressure is 75 psig. The drain line is leak tight.

The special containment canisters used within the cask cavity do not have any penetrations.

4.1.3 Seals and Welds

Seals on both the cask cavity and inner canisters are elastometric as discussed in Section 1. All welds are full penetration welds.

4.1.4 Closure

The closure of the cask cavity is accomplished by twelve 1 inch x 8 studs with two lock nuts per stud. The initial tightening torque on the nuts is 50 feet/pounds. The closure of the canister is accomplished by ten 3/8 x 16 inch bolts. The initial tightening torque on the bolts is 60 inch/pounds.

4.2 Normal Conditions of Transport

The performance of the cask and inner canister during normal conditions of transport are presented in the applicable subsections of Section 2 and 3.

4.3 Hypothetical Accident Conditions

The performance of the cask and inner canister during the hypothetical accident conditions are presented in the applicable subsections of Sections 2 and 3.

4.4 APPENDIX

4.4.1 References

(1) U.S. Nuclear Regulatory Commission Certificate of Compliance for Radioactive Materials Package Number 5957, Rev. 4, June 15, 1978.